TECHNISCHE
UNIVERSITÄT
DARMSTADT

Design and test of a highly scalable servo drive system based on PM linear synchronous motors

genehmigte
Dissertation

von

Dipl.-Ing. Sorin Mihail Silaghiu
aus Ploiesti/Rumänien

Design and test of a highly scalable servo drive system based on PM linear synchronous motors

Vom Fachbereich 18

Elektrotechnik und Informationstechnik

der Technischen Universität Darmstadt

zur Erlangung des akademischen Grades eines

Doktor-Ingenieurs (Dr.-Ing.)

genehmigte

Dissertation

von

Dipl.-Ing. Sorin Mihail Silaghiu

geboren am 31. August 1983 in Ploiesti, Rumänien

Preface

This PhD thesis is the result of my research work at the department of Power Electronics and Control of Drives at Darmstadt University of Technology.

My special thanks go first to the head of the department, Prof. Dr.-Ing. Peter Mutschler, for guiding this work. I am very grateful for his valuable advices, patience and encouragement during all the research years.

I would like to express my sincere gratitude to Prof. Dr.-Ing. Bernhard Piepenbreier from the department of Electrical Drives and Machines at the Friedrich-Alexander University in Erlangen-Nürnberg for his interest and willingness to be the co-reviewer of this thesis.

I thank my colleagues and also the students, who did their seminar or diploma thesis in my research field at the department, for the professional discussions, suggestions and support. The realisation of the experimental set-up would not have been possible without the support of the technical staff. I also appreciate the help of our secretary regarding all administrative issues. I am grateful to all my colleagues at the department for the very good working atmosphere.

I want to give my sincere thanks also to my parents, especially my mother, who supported and encouraged me throughout my entire education.

At the end I thank God for giving me the opportunity to do my PhD in Darmstadt, for His guidance and for giving me the daily energy and strength that I need.

Darmstadt, 27.10.2011

Abstract

In many industrial plants materials have to be transported between several processing stations, where they have to be processed with a high level of accuracy and precision. In the last years, linear electrical drives, especially the long-stator linear motors are used for these types of applications for both processing and transportation tasks. They have higher dynamics and processing precision and lower maintenance costs compared to conventional systems, which require additional mechanical gears.

The linear drive system must be modular and highly scalable in order to cover a wide range of applications. For this reason, the track of the plant is made of several stator segments. The excitation part of the motor is represented by permanent magnets (passive vehicles). Each stator segment has a dedicated inverter (Power Processing Unit) and processor (Information Processing Unit). Cheap IPMs (Intelligent Power Modules) are nowadays a good solution for implementing the inverter. A DSP was used as processor. The DSP and the IPM are the main components of the designed servo-controller, which together with a stator segment represents a module of the system. The DSP controls the inverter and is also used for the communication with the DSPs of the adjacent modules.

By connecting the ground potential of all servo-controllers to the negative DC-link rail ($\approx$ -280 V), a significant reduction in the implementation costs of the servo-controller was achieved.

When a vehicle crosses from one stator segment to the adjacent one, the control tasks migrate physically in that respective adjacent DSP. Data exchange is therefore required within each cycle of the current control loop (100 µs) between the adjacent modules. For an arbitrary scalable modular system, there will be also an arbitrary high communication demand. This demand can only be solved by a direct (Point-to-Point) connection between the adjacent DSPs. This connection was realised by means of the cost-effective RS485 data transmission protocol.

A central control unit is responsible then for the cyclical (1-10 ms) generation of new position reference values for the vehicles, according to a predefined schedule. The monitoring (assessment of internal variables of the distributed servo-controllers) of the entire system is realised also in real-time. Off-line download and upload actions of firmware or general data is also possible. For these tasks, the communication between the central unit (PC) and the distributed servo-controllers was realised by means of the Ethernet-based fieldbus EtherCAT.

Inside the processing stations of the system, the positioning accuracy and precision as well as the dynamic have to be very good. For this reason, inside those stations, position sensors must be

used. Outside those stations, for material transportation only, an EMF-based sensorless control was implemented. This will further reduce the overall system costs.

A small section of such modular and highly scalable system was realised as an experimental set-up in the context of this work, in order to test the functionality and the reliability of the proposed system.

Kurzfassung

In vielen Industrieanlagen werden Materialien in Bearbeitungsstationen mit hoher Präzision bearbeitet und zwischen diesen Stationen transportiert. Dafür kommen in den letzten Jahren immer häufiger Linearantriebe, speziell der Langstator Linearmotor, sowohl für die Bearbeitung als auch für das Transportieren zum Einsatz. Der Grund hierfür liegt in der hohen Dynamik, bei gleichzeitig hoher Positioniergenauigkeit und in der Reduzierung der Wartungskosten, weil keine zusätzlichen Getriebe notwendig sind, wie bei den rotierenden Antrieben.

Das Linear-Antriebsystem muss modular und beliebig skalierbar sein, um eine große Vielfalt von Anwendungen abzudecken. Dafür wird der Fahrweg in viele Statorabschnitte unterteilt. Die Sekundärteile (passive Fahrzeuge) sind Permanentmagnete. Jedem Statorsegment werden sowohl ein Umrichter (Leistungsteil) als auch ein eigener Prozessor (Informationsteil) zugeordnet. Preisgünstige IPMs (Intelligent Power Modules) bieten heutzutage eine gute Lösung für die Implementierung des Umrichters. Ein DSP wird als Prozessor eingesetzt. Der DSP und der IPM sind die Hauptkomponenten des ausgelegten Servocontrollers, der zusammen mit einem Statorsegment ein Modul des Systems darstellt. Der DSP dient sowohl zur Steuerung des Umrichters als auch zur Kommunikation mit den benachbarten Modulen.

Eine deutliche Reduzierung der Implementierungskosten des Servocontrollers wurde gewährleistet, indem die informationsverarbeitende Elektronik auf das Potential des Zwischenkreises (≈ -280 V) gelegt wurde.

Wenn sich ein Fahrzeug von einem Statorsegment zum nächsten bewegt, wandert dann die gesamte Regelungsaufgabe physikalisch in die nächste Informationsverarbeitungseinheit (DSP). Ein Datenaustauschbedarf mit der Zykluszeit der Stromregelung (100 µs) entsteht dann zwischen den benachbarten Modulen. In einem beliebig skalierbaren System entsteht daher auch ein beliebig großer Kommunikationsbedarf. Dieser Bedarf wird nur mit Hilfe einer direkten (Punkt-zu-Punkt) Verbindung zwischen den benachbarten Modulen erfüllt. Diese Verbindung wurde hier mit dem kostengünstigen RS485 Protokoll realisiert.

Ein Leitrechner sorgt dann für die Erzeugung von Positions-Sollwerten für die Fahrzeuge, unter Berücksichtigung eines Fahrplanes. Die Zykluszeit für die Positions-Sollwerte liegt im Bereich von 1-10 ms. Das Monitoring (Beobachtung von internen Variabeln der zahlreichen Servocontrollern) wird auch in Echtzeit gewährleistet. Offline sind Download- und Upload-Aktionen von Firmware und allgemeine Dateien auch möglich. Dafür wurde für die Kommunikation zwischen dem Leitrechner und den verteilten Servocontrollern der Ethernetbasierte Feldbus EtherCAT verwendet.

Innerhalb der Bearbeitungsstationen des Systems spielen die Positionierungsgenauigkeit und die Dynamik eine wichtige Rolle. Deswegen werden innerhalb dieser Stationen Positionssensoren verwendet. Für den Transport der Materialien außerhalb dieser Bereiche, wurde eine EMK-basierte sensorlose Regelung implementiert. Dadurch lassen sich weitere Systemkosten sparen.

Im Rahmen dieser Arbeit wurde ein kleiner Ausschnitt eines solchen modularen und beliebig skalierbaren Systems als Versuchsaufbau realisiert und dessen Funktionsfähigkeit nachgewiesen.

Contents

List of symbols and abbreviations

Symbols:

Voltages:

u_{S1}, u_{S2}, u_{S3}	Phase voltages of a stator segment
u_{Sa}, u_{Sb}	Stator voltages represented in the stator-oriented coordinate system (ab)
u_{Sd}, u_{Sq}	Stator voltages represented in the rotor-oriented coordinate system (dq)
e_{S1}, e_{S2}, e_{S3}	Induced voltages in the phases of a stator segment
e_{Sa}, e_{Sb}	Induced voltages represented in the (ab) coordinate system
e_{Sd}, e_{Sq}	Induced voltages represented in the (dq) coordinate system
u_{10}, u_{20}, u_{30}	Output voltages of the inverter
u_{ofs}	Offset voltage to be added to the reference phase voltages
u_{S0}	Star point potential of a stator segment
$u_{CC,surge}$	Blocking voltage of an IGBT during commutation
u_{line}	Transient voltage on the common negative DC-link bus
u_{CM}	Common-mode voltage
u_{A}, u_{B}	Potentials of the RS485 pair of wires for differential transmission of a signal
u_{1C}, u_{2C}, u_{3C}	Compensated phase voltages due to the inverter's characteristics
u_{SaC}, u_{SbC}	Compensated voltage reference values represented in the (ab) coordinate system
$\underline{U}_0, \underline{U}_7$	Zero-voltage vectors of the inverter
U_D	Voltage of the DC-link
U_{Cap}	Voltage on an electrolytic capacitor of the DC-link
U_{di}	On-state voltage of the inverter's freewheeling diode
U_{ti}	On-state voltage of the inverter's IGBT
U_{dt}	Average on-state voltage in a control cycle of both diode and IGBT
U_{DV}	Deviation from the reference value of the inverter's output voltage

Currents and Fluxes:

i_{S1}, i_{S2}, i_{S3}	Phase currents of a stator segment
i_{Sa}, i_{Sb}	Stator currents represented in the stator-oriented coordinate system (ab)
i_{Sd}, i_{Sq}	Stator currents represented in the rotor-oriented coordinate system (dq)

i_C	Current through the DC-link capacitors of an inverter
$i_{D,ac}$	AC component of the rectifier's output current
i_{ac}	AC component of the inverter's input current
i_{line}	DC-link current between two adjacent inverters
I_{tC}	Current peak value during the charge time of the local DC-link capacitor
I_{tDC}	Current peak value during the discharge time of the local DC-link capacitor
I_N	Output current of the inverter
$\psi_{S1}, \psi_{S2}, \psi_{S3}$	Flux linkages of the stator phases
ψ_{PM}	Flux linkage of the permanent magnet with the stator

Parameters and Gains:

R_S	Winding resistance of a stator phase
L_S	Winding inductance of a stator phase
L_{Sd}, L_{Sq}	Stator winding inductance components in the (*dq*) coordinate system
M_v	Mass of the vehicle
V_M	Gain of the motor's transfer function
V_{RI}	Gain of the current controller's transfer function
C_{EL}	DC-link capacitance of an inverter
$L_{\sigma,common}$	Common stray inductance of the DC-link
$L_{\sigma,ph}$	Stray inductance in an inverter leg
$L_{eff,ac}$	Inductance value of the DC-link bus bar system at high frequencies
$L_{bar,ac}$	Self-inductance of a DC-link bus bar at high frequencies
$L_{mt,ac}$	Mutual inductance in the DC-link bus bar system at high frequencies
$L_{\sigma S}$	Stray inductance between the electrolytic and snubber capacitors
L_{ESR}	Equivalent series inductance of the electrolytic capacitor
R_{ESR}	Equivalent series resistance of the electrolytic capacitor
L_{SN}	Equivalent series inductance of the snubber capacitor
C_{SN}	Value of the snubber capacitor
$L_{\sigma IPM}$	Stray inductance of the IPM connection pins
$h_{11}, h_{22}, g_{11}, g_{22}$	Gains of the EMF observer
p_1, p_2, p_3, p_4	Roots of a 4th order polynomial
k_1, k_2, k_3	Gains of the mechanical observer
b_C	Speed-dependent friction coefficient

Times and Frequencies:

T_{Sd}, T_{Sq}	Time constants of the current control loop
T_0	Sampling time
T_M	Time constant of the motor's transfer function

T_E	Time constant of the inverter's transfer function
T_{RI}	Time constant of the current controllers
T_{EI}	Equivalent time constant of the current control loops
t_{osc}	Oscillation time of the current measurement circuit
t_C	DC-link capacitor charge time
t_{DC}	DC-link capacitor discharge time
t_{DEAD}	Dead-time
$t_{C,ON}, t_{C,OFF}$	Turn-on and turn-off times of the IGBTs
t_{on}	Time inside a control cycle during which the low-side IGBT is on
$T_1...T_{10}$	Time intervals corresponding to the SPI communication
ω_0	Natural frequency of the current control loop
f_N	Output frequency of the inverter
f_{mains}	Frequency of the mains
f_G	Output frequency of the bridge rectifier

Angles:

γ	Electrical angle between the phases of a stator
β	Electrical angle of the rotor (vehicle)
$\Delta\beta$	Difference between the estimated and the real value of the electrical angle
φ	Angle of the inverter's voltage vector

Subscripts and marks:

O_{min}	Minimal value
O_{max}	Maximal value
O_{nom}	Nominal value
O_{ref}	Reference value
O_{RMS}	Root mean square value
O_{IN}	Input value
O_{OUT}	Output value
O_Σ	Sum value of the induced voltages in two adjacent stator segments
O_E	Output angle or position values from the EMF observer
O_M	Output angle or position values from the mechanical observer
$\hat{O}$	Estimated value
$\tilde{O}$	Estimation error
$\dot{O}$	Time derivative
O^*	Complex conjugate
$\underline{O}$	Space vector treated as a complex quantity

Matrixes in state space representation:

x	Matrix of the state variables
A, Ad, Av	State matrixes
B	Input matrix
K	Disturbance matrix
d	Matrix of the disturbance variables
I$_2$, I$_3$	Unity matrixes
H, G	Gain matrixes

Other Symbols:

a_g	Air gap between the stator and the permanent magnet
μ_{rec}	Recoil permeability
μ_0	Vacuum permeability
τ	Pole pitch of the motor
v	Speed of the vehicle
v_f	Filtered speed of the vehicle
x	Distance
p_i	Instantaneous power at the motor terminals
p_{mag}	Instantaneous power in the magnetic field of the stator
p_{mech}	Instantaneous mechanical power
p_{ohm}	Instantaneous value of the ohmic power losses
p_{rel}	Instantaneous value for the reluctance component of the mechanical power
$\Re\{\ \}$	Real part of an expression
j	Imaginary unit
F_{th}	Thrust force
F_d	Disturbance force
F_L	Load force
k_F	Force constant
s	Laplace operator
D_0	Damping of the control loop
G_0, K	Transfer functions
pd, pq	Perturbances of the current control loops
$P_0...P_{21}$	Specific positions of the vehicle along the track of the experimental set-up,
P_C, P_D, P_R, P_S	which trigger or define specific actions of the control stage
P_X, P_Y, P_Z	

Abbreviations:

ADC	Analog to Digital Converter
AMR	Anisotropic Magneto-Resistiv
ASCII	American Standard Code for Information Interchange
ASIC	Application Specific Integrated Circuit
CCU	Central Control Unit
CLK	Clock
COFF	Common Object File Format
CSMA	Carrier Sense Multiple Access
DCU	Distributed Control Unit
DSP	Digital Signal Processor
EtherCAT	Ethernet for Control Automation Technology
EMC	Electro-Magnetic Compatibility
EMF	Electro-Motive Force
EMI	Electro-Magnetic Interference
ESC	EtherCAT Slave Controller
EVM	Event Manager
FMMU	Field Memory Management Unit
FoE	File access over EtherCAT
FO	Fault Output
FOC	Field-Oriented Control
FPGA	Field-Programmable Gate Array
FTP	File Transfer Protocol
GPIO	General Purpose Input Output
HTTP	Hypertext Transfer Protocol
HVIC	High Voltage Integrated Circuit
IGBT	Insulated Gate Bipolar Transistor
IP	Internet Protocol
IPM	Intelligent Power Module
IPU	Information Processing Unit
IRT	Isochronous Real Time
LBM	Linear Brushless Motor
LCU	Line Connection Unit
LIM	Linear Induction Motor
LMU	Linear Motor Unit
LSM	Linear Synchronous Motor
LVIC	Low Voltage Integrated Circuit
LVTTL	Low Voltage Transistor-Transistor Logic
Mbps	Megabits per second

McBSP	Multichannel Buffered Serial Port
MF	Medium Frequency
MISO	Master Input Slave Output
MOSFET	Metal Oxide Semiconductor Field Effect Transistor
MOSI	Master Output Slave Input
OSI	Open System Interconnection
PCB	Printed Circuit Board
PDPINT	Power Drive Protection Interrupt
PDI	Process Data Interface
PE	Protection Earth
PI	Proportional Integrative
PLC	Programmable Logic Controller
PM	Permanent Magnet
PMLSM	Permanent Magnet Linear Synchronous Motor
PPU	Power Processing Unit
PSU	Position Sensor Unit
PT1	First-order lag element
PWM	Pulse-Width Modulation
RAM	Random Access Memory
RTE	Real Time Ethernet
RU	Rectifier Unit
SPI	Serial Peripheral Interface
SS	Slave Select
TCP	Transmission Control Protocol
TDMA	Time Division Multiple Access
TTL	Transistor-Transistor Logic
TwinCAT	The Windows Control and Automation Technology
UDP	User Datagram Protocol
VSI	Voltage Source Inverter
XINTF	External Interface
WKC	Working Counter

1. Introduction

The linear electric motor works after similar principles as the rotary electric motor, consisting of a stator and a mover separated by an air gap. The magnetic fields of these two parts will interact to produce a linear direct motion, meaning that no mechanical transmission is required between the stator and the mover. As they use the similar principles for generating the electromagnetic force, there are as many types of linear motors as rotary motors. Almost every rotary motor type will find its correspondent in the class of the linear motors. If a rotary motor is unrolled, it will form a flat, single sided linear motor. Rolling again this flat linear motor about the axis of the direction of movement will form a tubular linear motor. The magnetic flux of a linear motor can be parallel to the direction of movement (longitudinal flux motor) or perpendicular to this direction (transverse flux motor). A combination of the two types of fluxes inside one linear motor is also possible, where the flux is transverse in the stator and longitudinal in the mover [1]. The part of the linear motor, which produces the magnetic field in the air gap, is called excitation part and the other part where voltage is induced is called armature. Each part can be on the stator or on the mover side. According to the principle of generation of the electromagnetic force, the linear motors can be divided into three main categories:

- Linear Induction Motor (LIM). The part of the motor, which produces a travelling magnetic field in the air gap, is called primary (excitation part) and consists of three-phase windings. This travelling field will induce a voltage in the secondary of the machine if there is a speed difference (slip) between them. The secondary consists of a conducting plate on a solid iron or of short-circuited three-phase windings placed in slots of laminated core [2]. The induced voltage will generate currents in the secondary, which are interacting with the travelling magnetic field to produce the electromagnetic force.

- Linear Synchronous Motor (LSM). The armature creates in this case the travelling magnetic field and consists of three-phase windings. The excitation part can create a magnetic field or a variable magnetic reluctance in the air gap. This magnetic field can be produced by a PM or by a DC-current winding and it will interact (synchronize) with the travelling magnetic field to generate electromagnetic force. In the case of the variable magnetic reluctance motors, the electromagnetic force is a reaction force of the mover to the travelling magnetic field.

- Linear Brushless Motor (LBM). This motor works with a rectangular three-phase current system, whereas the first two above mentioned types are using sinusoidal currents. The induced voltages in the armature are trapezoidal. Using a position sensor, the commutation process of the currents is synchronized with the position of the mover. The LBM is therefore a special type of LSM.

Linear Electric Motor
(layout)

Flat geometry	Tubular geometry
Longitudinal flux	Transverse flux
Double sided	Single sided
Slotted	Slotless
Long stator *Long primary*	Short stator *Short primary*

Linear Electric Motor
(operation)

Induction | Synchronous | Brushless DC

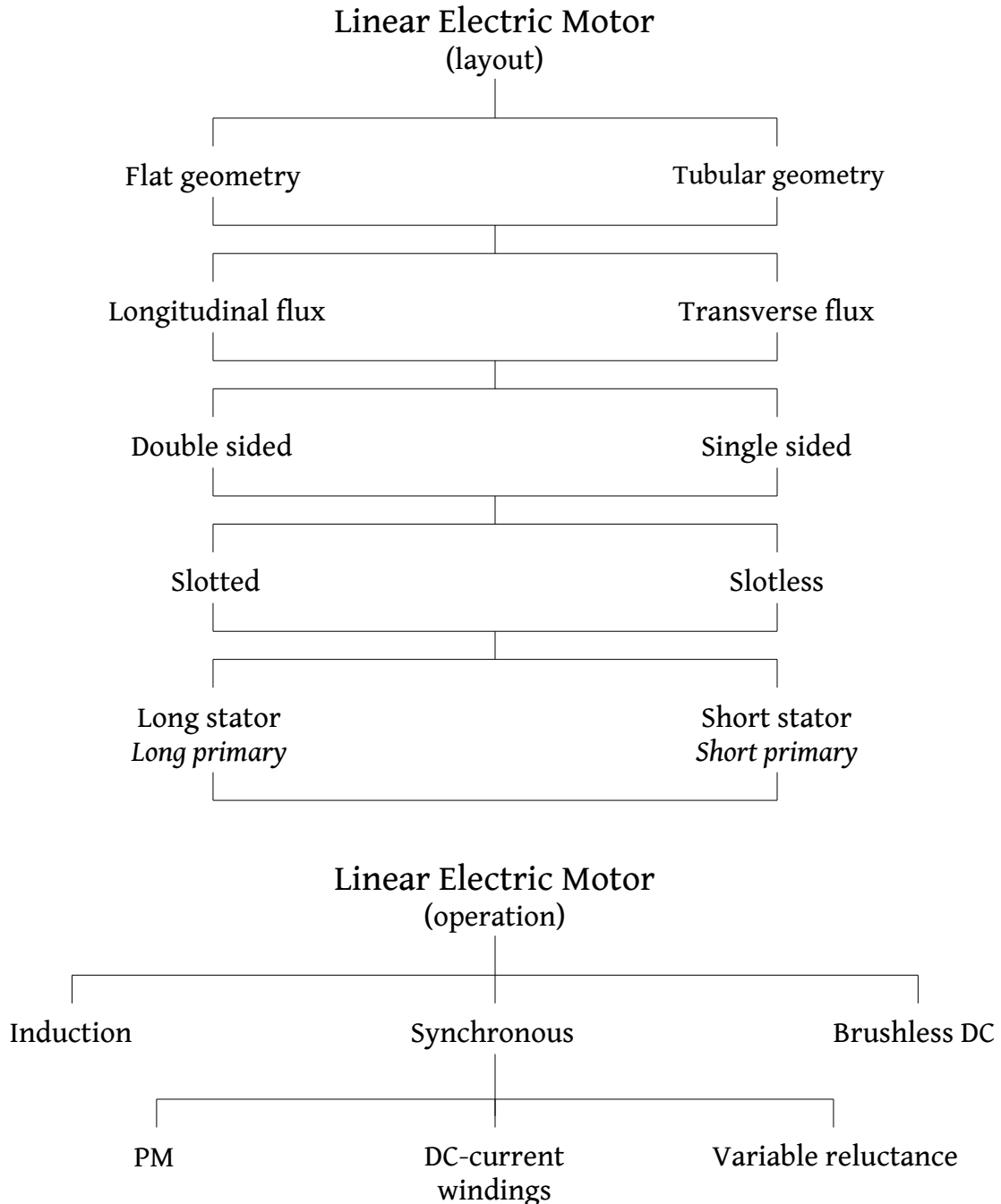PM | DC-current windings | Variable reluctance

Figure 1.1 Classification of the linear motors

In Figure 1.1 a brief classification of linear motor types is shown, regarding both the motor layout and the principle of operation. In the case of long-stator LSMs, the armature is longer than the excitation part. For short-stator LSMs the excitation part is longer than or equal to the armature.

For LIMs the terms of long-primary and short-primary are preferred instead. Almost any combination between layout and operation forms is possible depending on the application.

The linear motors were first mentioned at the end of the 19th century and at the beginning of the 20th century their main applications were meant for high-speed propulsion and public transportation systems. In 1946 the *Westinghouse Corporation* builds the first large-scale linear motor for aircraft launching, called *Electropult*, which was capable of speeds of about 100 m/s [1]. Even though the idea of using electromagnetic levitation in public transportation systems dates back in 1922, the first practical construction only took place in 1969 in *Munich*, *Germany* and the model was called *Transrapid 01*, which was capable of speeds up to 100 km/h [3]. The maglev (magnetic levitation) transportation system combines the linear motor technology with the technology of contactless magnetic suspension, offering energy efficient and pollution free alternative to air, car and standard railway traffic. Starting with the early 1970s the maglev systems for public transportation developed continuously, as they still are in the present. For industrial applications like machining, material processing or laser cutting, the linear electric motors started to win recognition and to be implemented only at the beginning of the 1990s [3]. The continuous progress over the last years in areas like motor design, power electronics, control of drives, positioning sensors and industrial fieldbuses, together with the actual interest for new intelligent solutions in transportation and industrial plants, opened new perspectives for the linear direct drives applications.

1.1. State of the art

1.1.1. Linear electric motors for public transportation

For high-speed (over 400 km/h) maglev systems, the long-stator LSM is preferred. The short-stator LSM is not used because there is the problem supplying the vehicle with energy and the vehicle would also be heavy, as all the necessary power converting units are situated on it. The LIM is also not an alternative for high-speed transportation, because its efficiency is strongly affected by the wide air-gap and its fluctuations. Only the currents in the primary produce the thrust force of the LIM, as the secondary has no independent magnetic field. The primary of the LIM will have therefore bigger dimensions than the armature of an LSM for the same thrust force, as it must carry the magnetization current component in addition.

In the last years, low-speed (100-150 km/h) linear motor systems become interesting for passenger transportation in urban areas [4], [6], [7] and also for goods transportation over short distances inside crowded industrial areas [4]. These transportation systems are with or without magnetic levitation and for propulsion usually long-stator LSMs or short-primary LIMs are used [5]. Nowadays ropeless elevators, based on linear electric motors, represent an alternative to the conventional elevators in very high buildings. The fixed parts of the motors are situated on the shaft's wall and the moving parts are the cabins. No drive units situated at the top of the building are required. More cabins are allowed to move independently on the same shaft and horizontal

movements are also possible in order to change the shaft. This increases the transportation efficiency, so that the number of shafts can be reduced. The building's size and automatically its construction costs can be therefore reduced. The *Multi Mobile System (MMS)*, developed in *Switzerland* and supported by the elevator manufacturer *Schindler AG*, uses a double-sided, long-stator LSM with excitation realized by PMs. One stator segment is made up of many motor modules connected in parallel. An inverter supplies each segment and all the inverters are sharing the same DC-link bus [8]. For these applications the double-sided, long-stator PMLSM with a slotted iron core is the best solution, as it develops the biggest thrust-force density compared with other linear motor topologies [9].

The most popular linear electric motor used now in public transportation is therefore the long-stator LSM. Because the vehicles travel over long distances, the armature along the guideway is split in many segments in order to improve the efficiency [10]. Only those segments involved in the development of the thrust force are energized. The segments have different lengths and can be separated by different gap sizes. In systems requiring relative high throughput (many travelling vehicles per time unit), as in the case of elevator systems, the segments are small compared with the size of the vehicle and are supplied by dedicated inverters.

The throughput is low for large distance transportation systems, so that the segments are long and a set of multiplexed inverters supplies several segments by switchgears. Different inverters can also supply two adjacent segments. When the vehicle passes over the respective segments, both inverters must be synchronized so that the desired thrust force is generated. A central control unit is responsible for the position and speed of the vehicle. These actual values are transmitted over a wireless communication system from the vehicle to the control units. The distributed control units manage the power flow from the inverts to the respective segments according to new position and speed reference values generated by a traffic planner.

The system topology of the *Transrapid* system in *Shanghai* is shown in Fig. 1.2. It is a modular control system, where the modules, called substations, are located along the guideway [11].
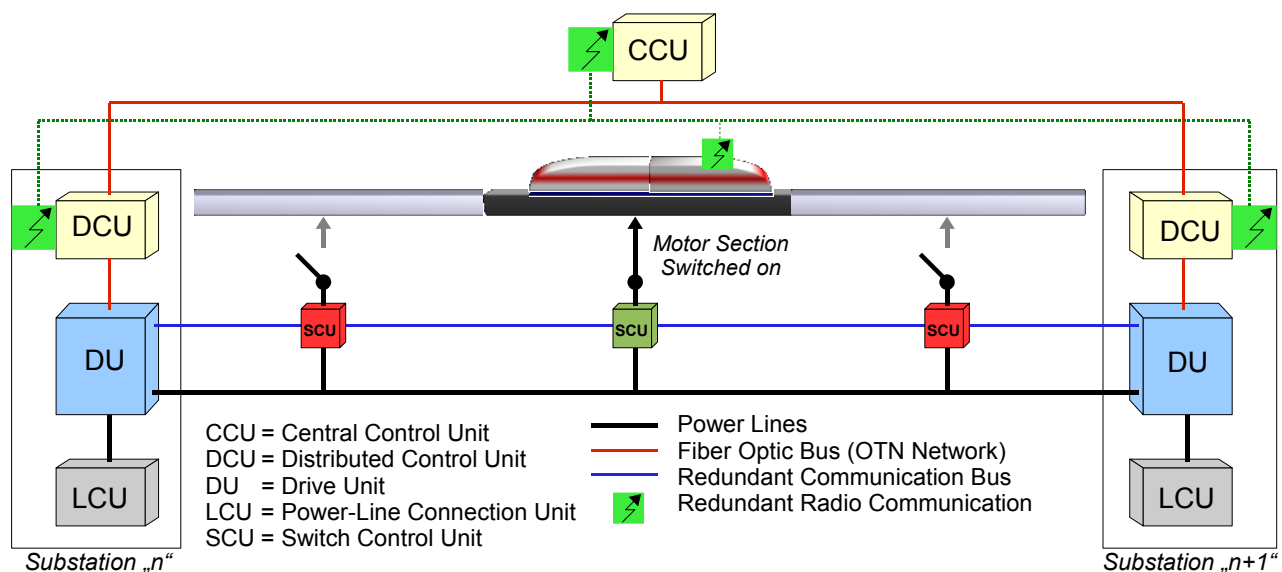

Figure 1.2: Topology of the *Transrapid* system in *Shanghai*

1.1.2. Linear electric motors in industrial applications for material handling and factory automation

Linear electric motors are used nowadays in industrial applications such as semiconductor industry, flat panel display manufacturing, machine tools, electronics assembly, factory and laboratory automation, robotics and photovoltaic cell manufacturing. Compared to conventional systems using pulleys, racks, screws or other mechanical parts that transform rotary to linear motion, direct drive systems based on linear motors have higher processing precision and lower maintenance costs. The implementation costs can be higher, but they are compensated in time by the higher throughput capability.

Material handling is an emerging application, which benefits from the advantages of the linear drive systems. Here, small to medium sized materials must be positioned with high dynamics between special stations, where they have to be processed with a high degree of accuracy. A single linear direct drive system is used for both transportation and processing tasks. Inside this class of applications there are several possible topologies [12], depending on specific features of the application, like the size and profile of the production track, the number of material carriers (vehicles), the dynamic requirements, the power rate and the implementation costs. Typical specifications in material handling and factory automation applications are [13]:

- Positioning accuracy around 50 μm
- Repeatability 10-20 μm
- Demanding duty cycles
- High dynamics and reliability over cost ratio

The general system configuration for this type of applications is shown in Fig. 1.3. The main units of the system are:

- Linear motor unit (LMU)
- Power processing unit (PPU)
- Information processing unit (IPU)
- Position sensor unit (PSU)

At the LMU-level the PMLSM is used for its high thrust-force density and for the fact that air-gaps of few millimetres are allowed. Both short-stator and long-stator PMLSM types are used. The iron core can be slotted or slotless. The slotted type has a bigger thrust force per volume unit, but has
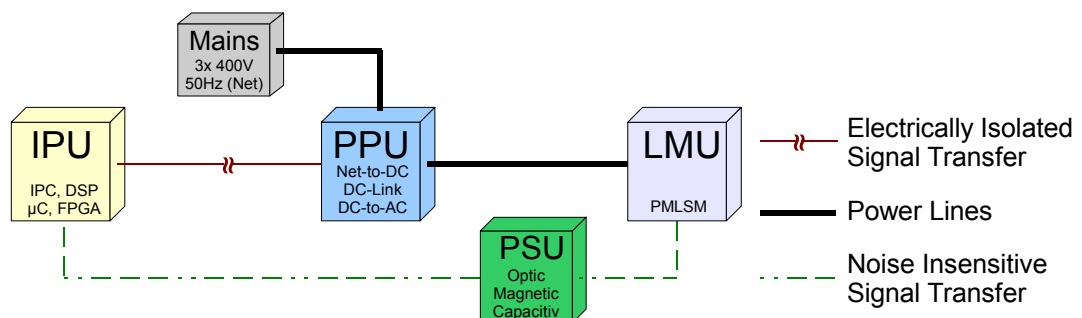

Figure 1.3: Configuration of the direct drive system

therefore a significant cogging force. The most popular technique to reduce the cogging effect is skewing the magnets [3]. The single-sided configuration of the PMLSM usually fulfils the dynamic requirements, but in the case of high acceleration demands, or if the attractive force between the PM and the iron core is too high, the double-sided configuration can be implemented. Rare-earth magnets such as NdFeB (Neodymium-Iron-Boron) or SmCo (Samarium-Cobalt) are selected for the excitation part of the LSM due to their high remanence and energy density values.

At the PPU-level a standard voltage source inverter (VSI) supplies the windings of the armature. Multiplexing inverters by mechanical or electronic switches is not a feasible solution for long-stator topologies in this case. The mechanical switches are not applicable due to the large number of switching actions per time unit and a safe-functioning electronic switch unit will require a larger number of IGBTs than using one dedicated inverter for each motor section.

At the IPU-level there is always a central control unit (CCU) responsible for the traffic flow inside the system. It generates the new position reference values of the vehicles, monitors the entire process and interacts with the system administrator over a graphical interface. The CCU is connected with the PPU by means of a controller, such as microcontroller, DSP or FPGA. The connection between this controller and the PPU is typically electrically isolated, where the pulse width modulated (PWM) signals generated by the controller are connected to optocouplers and then transferred to the gate-drive units of the power electronic devices of the VSI (IGBTs or MOSFETs). The position control algorithm is implemented either in the CCU or in the above-mentioned controllers. The most popular control method for servo drives is the field-oriented control (FOC), where all calculations are performed in the orthogonal moving frame of the vehicle. For this reason, the position of the vehicle must be known. All the controllers inside one system have to communicate with the central control unit by means of an industrial communication protocol.

There are three linear direct drive topologies used for material handling and factory automation.

1) **Short-stator topology**

It is still the most wide spread topology in this class of industrial applications. The track is passive and contains the PMs and the vehicles are the active part (moving windings). The energy is brought to the vehicles by cable drag chains or by sliding contacts. The motor system from the *Parker Company*, shown in Fig. 1.4, is an example of such topology. The PPU contains a standard VSI and at the IPU-level there is a controller designated to each vehicle. The controller communicates with the CCU over a cable or a wireless connection. The controller, the VSI and the position sensor are physically situated on the vehicle. Due to the complexity of the cable structure module, it is very difficult to use this topology over long distances or if many vehicles are present in the system. The difficulty due to long and curved tracks can be avoided by using a contact-less energy transmission at medium frequency (MF), as shown in Fig. 1.5. In this case the PPU inside one vehicle contains beside the VSI also the secondary of the MF-transformer and a rectifier. Due to the fixed power rate of this transformer, if many vehicles are simultaneous in acceleration or
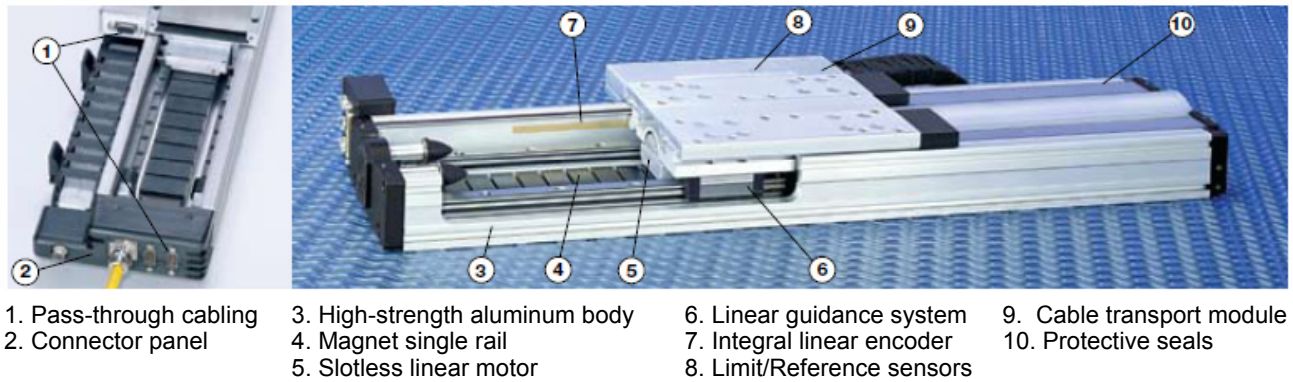
1. Pass-through cabling
2. Connector panel
3. High-strength aluminum body
4. Magnet single rail
5. Slotless linear motor
6. Linear guidance system
7. Integral linear encoder
8. Limit/Reference sensors
9. Cable transport module
10. Protective seals

Figure 1.4 Short-stator PMLSM with drag chains (*Parker*) [14]

deceleration phases, this alone cannot assure the dynamic requirements. For this reason, the short-stator topology is only recommended for systems with short tracks, high dynamics and low number of vehicles or for systems with long tracks and low dynamics. The dynamic performance can be improved if rechargeable power supplying elements like super capacitors are used on the

1. Central Control Unit
2. Mains
3. MF Power Generator
4. MF Transmission Line
5. Distributed Controller Unit
6. Voltage Source Inverter
7. MF Transformer
8. Sup. Capacitor & DC/DC Converter
9. Slotted Linear Motor
10. Magnetic Single Rail
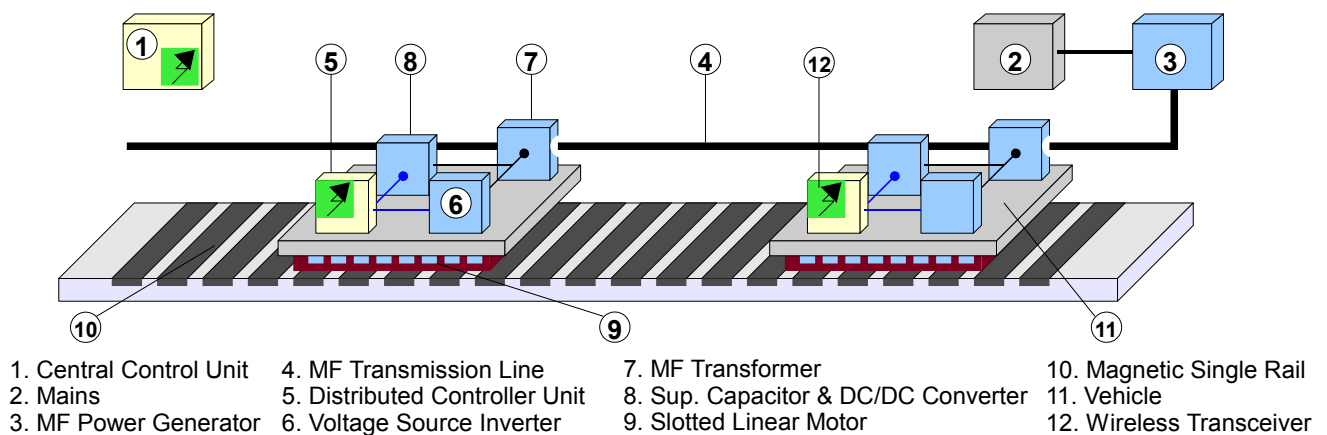11. Vehicle
12. Wireless Transceiver

Figure 1.5 Short-stator topology with contact-less energy transmission

board of the vehicles. These elements are discharged during acceleration periods and are again recharged during braking. They are also a part of the vehicle's PPU along with the power converters that assure this energy flow, leading to relative heavy and complex vehicle structures. There are research projects focusing on this topology [15].

2) Centralized long-stator topology

In some industrial plants for material handling, beside the high processing accuracy, a high throughput and a high complexity of the production track are also required. It involves a high number of vehicles per track length, which have to move with a high degree of independency, meaning that they are all able to accelerate and brake simultaneously without loosing their dynamic. The track can have curves, close paths and switches. For these considerations, the long-stator PMLSM topology is the suited one. The track is spilt into several armatures (segments) and only one vehicle may be present on a segment at a given time. The vehicles are passive elements (moving magnets). Typical segment lengths are between 0.5 m and 1 m. A dedicated inverter

supplies each segment. In the case of a centralized long-stator topology both the PPU and the IPU are centralized, e.g. situated in a cabinet.

The implementation of a direct drive system based on this topology is supported by *FVA* (*Forschungsvereinigung Antriebstechnik*), a network for innovative drives in *Germany* [16]. The system is quite complex due to the structure of the IPU. The structure of the PPU is simple. A standard VSI is designated to each stator segment and all VSIs are connected to the same DC-link rails. The algorithm for current, speed and position control is executed inside the CCU at cycles of 100 µs. This cycle time is split in ten intervals, each interval being dedicated to one vehicle. The prototype system can have therefore a maximum of ten vehicles. The CCU is made of one or more industrial PCs operating with a real-time *Linux* kernel. An inverter-bus is used for data transfer (modulation information and measured phase currents) between the IPU and the PPU. Two controller-based interfaces are needed; one to connect the CCU to the inverter-bus and the other
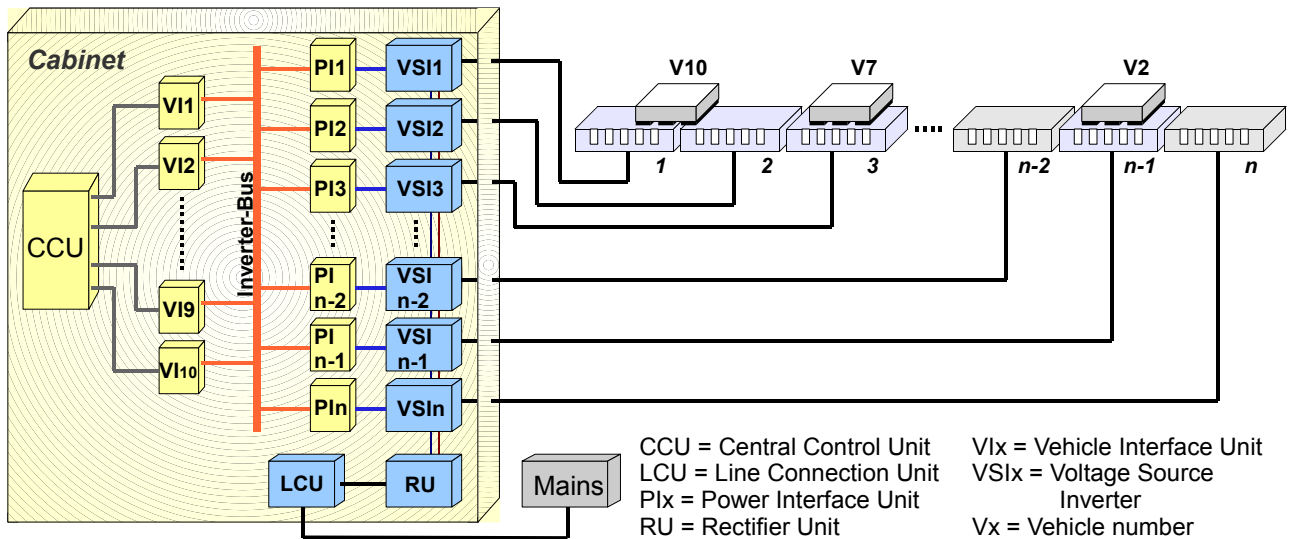

Figure 1.6 Long-stator topology with centralized IPU and PPU

to connect the VSIs to the same bus, as shown in Fig. 1.6.

The complexity of the CCU and the number of the vehicle-interface units increases along with the number of vehicles. The bandwidth of even the most powerful industrial filedbuses will be fully occupied in this case, so that the inverter-bus will always represent a bottleneck for the scalability of this system. The motor-supply cables represent another disadvantage of this topology, especially for large systems. They increase the overall cost, occupy a lot of space and can be very long. Long cables between the inverter and the motor will cause dangerous overvoltages at the motor terminals. At the same time the electromagnetic interference (EMI) generated by the inverter increases [17].

This topology is therefore suitable for small-to-medium systems with no more than ten vehicles.

3) Decentralized long-stator topology

The industrial applications tend to be more complex and larger, because the market demands for quality and quantity are constantly increasing. Therefore the need to process a bigger quantity of

products in a shorter time is high. Due to this trend, the long-stator topology for material handling applications became interesting in the last years. The centralized topology, as shown, limits the capability of a system to grow. A decentralized long-stator topology, as proposed in this
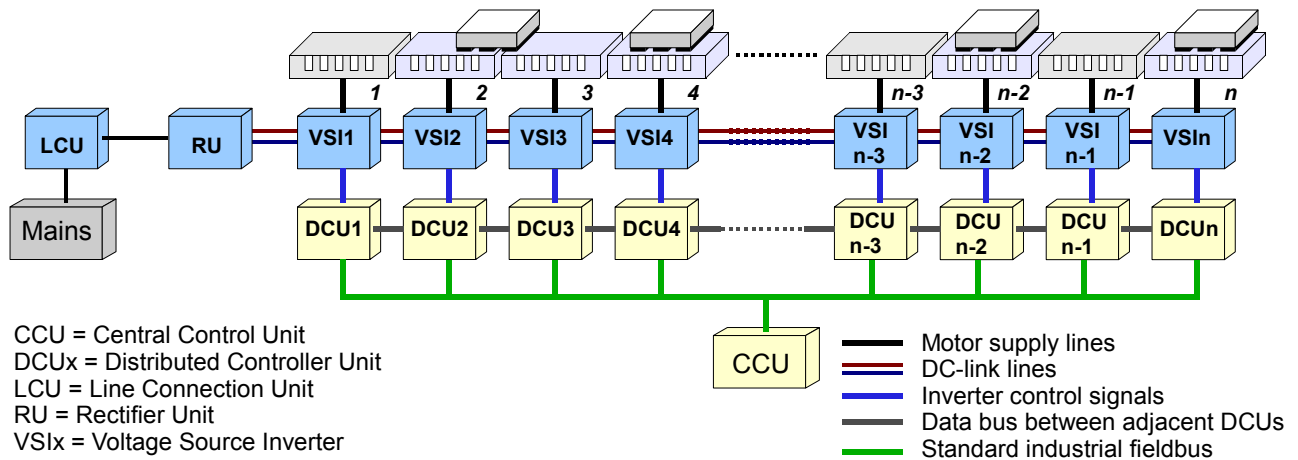

CCU = Central Control Unit
DCUx = Distributed Controller Unit
LCU = Line Connection Unit
RU = Rectifier Unit
VSIx = Voltage Source Inverter

Motor supply lines
DC-link lines
Inverter control signals
Data bus between adjacent DCUs
Standard industrial fieldbus

Figure 1.7 Long-stator topology with decentralized IPU and PPU

work, is a solution to this problem. The structure of a decentralized system is shown in Fig. 1.7. In this case one stator segment is also supplied by one VSI. The algorithm for current, speed and position control is entirely executed in the main controller of the DCU. The DCU also contains an interface that connects the unit to an industrial fieldbus. The CCU contains an industrial or a standard PC and a fieldbus interface. When a vehicle passes over two adjacent segments, the respective inverters must be synchronized, so that the desired thrust force can be generated at the vehicle. For the synchronisation, the involved DCUs have to exchange data within each current control cycle. This data transfer cannot be realized by means of an industrial fieldbus, because the same bottleneck problem will occur as in the case of a centralized topology. A special data bus connection between the adjacent DCUs has to be used instead, so that the entire bandwidth of the fieldbus serves only for monitoring and traffic control. The size of the system can be therefore considerably increased. Another advantage of this topology is its high degree of modularity. One module consists of a stator segment, the VSI and the DCU. Modules can be easily replaced or added to the system.

This type of topology is relative new and at the moment there are not many such systems available on the market or under research. One of the companies who developed a similar system is *MagneMotion* (*USA*). The central part of their system, presented in Fig. 1.8, is the *QuickStick* module, which can be 0.5 m or 1 m long and contains one or more stator segments (maximal ten), the necessary VSI and DCU and a position sensor system as well. The adjacent modules are connected over serial communication lines. A PC or PLC represents the CCU and the industrial fieldbus used here is EthernetIP. The DCUs are connected to this fieldbus over node controllers, which act as switches at junction points (turntables or electromagnetic switches) where more than two paths meet [18].
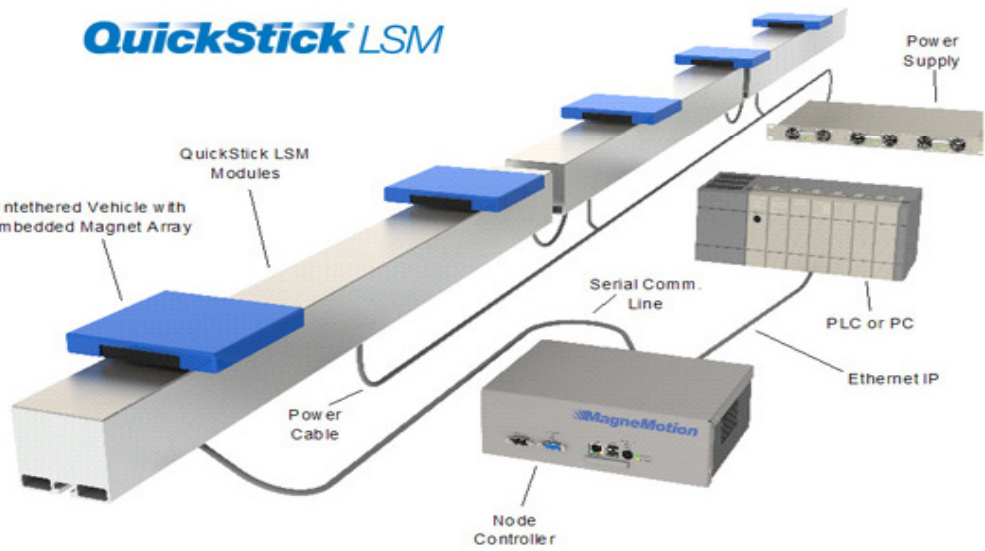
Figure 1.8 *MagneMotion*'s modular system structure [19]

The advantages of the topology in Fig. 1.7 are obvious. But at the first glance it also seems to be expensive due to the large number of controllers required. Investigations are still necessary in order to find solutions that reduce the implementation costs and the overall system complexity. Finally, the table below is a review of the characteristics of the three topologies presented above.

System topology:			Short-stator		Long-stator	
System characteristics:			**Cable drag chains**	**Contact less energy transmission**	**Centralized control**	**Distributed control**
Complexity		**PPU**	Low (one VSI per vehicle)	Medium (without Sup. Capacitors) High (with Sup. Capacitors)	Medium (one VSI per stator segment)	Medium (one VSI per stator segment)
		IPU	Low (one controller per vehicle)		High	
		PSU	Low (sensor chip on the vehicle)		High (sensor chip along the track)	
Costs (Over track length unit)		**PPU**	Low	Medium	High	
		IPU	Low		Medium-High	High
		PSU	Low (for a certain accuracy level)		Medium (for the same accuracy level)	
Dynamic			High	Low (without Sup. Capacitors) Medium (with Sup. Capacitors)	High	
Scalability			Low	Medium	Medium	High
Type of application	**Track length**		Very short	Long	Medium	Long
	Nr. of vehicles		Very small	Small	Medium	High
	Throughput		Medium	Medium	High	High

Table 1.1: Direct drive system topologies for industrial applications based on PMLSM

1.2. Starting point and purpose of the work

The starting point of this work was fixed on decentralized long-stator topology systems (Fig. 1.7), based on PMLSM, for industrial applications like material handling and factory automation. The purpose was to design and implement such a system, where the costs and complexity had to be reduced as much as possible without affecting the specifications mentioned in the section 1.1.2. The issues that appeared under these circumstances at the PPU and the IPU level had to identified and solved. The key aspects of this work are:

- The development of the control strategy (chapter 2). The sensor-based, as well as the sensorless EMF-based control were considered. The sensorless control is an important issue for long-stator topologies, where the position-sensing unit is very expensive.

- The development of a point-to-point communication structure between the DCUs with a minimal hardware and software complexity (chapter 3).

- The analysis and selection of the most suitable industrial fieldbus for this application, as well as its integration in the structure of the IPU (chapter 4).

- The development of a cost-effective servo-controller (VSI + DCU), where the ground potential of its electronic is tied at the negative DC-link rail (about –280 V). All servo-controllers are connected then to the same DC-link bus (chapter 5).

- The test of the developed system and of the control strategy, by means of a small-scale experimental set-up. This is meant to confirm the high scalability, the reliability and dynamic characteristics of the developed architecture (chapter 6).

2. Control strategy

This chapter presents the theoretical aspects regarding the control of the system. The adopted control strategy has to fulfil the specifications presented in the previous chapter regarding position accuracy, repeatability, throughput, reliability and dynamics. The FOC algorithm is based on the mathematical model describing the fundamental wave behaviour of the PMLSM without saturation and takes into account the synchronization requirements of two adjacent inverters during the vehicle's transition period across the respective stator segments. The algorithm is entirely implemented in the DCU where it is executed cyclically each 100 µs. The synchronization requires a data transfer in each cycle between the adjacent controllers. This represents the **hard** real-time communication demand of the control system. The motion coordination of the vehicles and the monitoring of the system is the task of the CCU. According to its traffic planner, the CCU must send cyclically new position reference values to the DCUs and collect status data from them. This data transfer has a cycle time of few milliseconds and represents the **soft** real-time communication demand of the control system.

2.1. Mathematical model of the PMLSM

Based on equations presenting the relations between electrical and magnetic values in the motor, the mathematical model describes the generation of the forces acting on the vehicle. The model is valid for both long-stator and short-stator topologies and considers no saturation and no space harmonics. The motor excitation is realised by rare earth PMs, which are characterized by a high coercitive magnetic field strength and low recoil permeability $\mu_{rec} \approx \mu_0$. They are subject to demagnetisation due to the reluctance of the entire magnetic circuit and the stator's reaction field, but are not affected by fluctuations in the air gap and can withstand strong demagnetisation
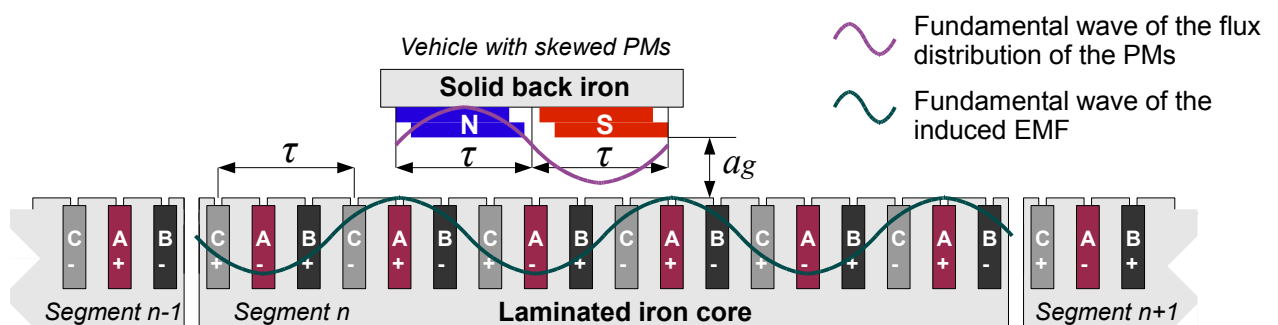

Figure 2.1 Structure of the segmented, long-stator PMLSM

cycles. For the PMLSM used in the experimental set-up, the PMs are bounded on the surface of a solid back iron and the stator windings are distributed in slots of a laminated iron core as shown in Fig. 2.1. The space distribution of the flux density in the air gap, produced by both PM and stator currents, for a motor topology similar to the one in Fig. 2.1, was determined in [20]. Only the fundamental of this value is considered, so that the EMF in the motor is assumed to be sinusoidal. The phase voltage equations of the PMLSM are:

$$u_{S1}(t) = R_S i_{S1}(t) + \frac{d\psi_{S1}(t)}{dt}$$
$$u_{S2}(t) = R_S i_{S2}(t) + \frac{d\psi_{S2}(t)}{dt}$$
$$u_{S3}(t) = R_S i_{S3}(t) + \frac{d\psi_{S3}(t)}{dt}$$

(2.1)

The equation (2.1) in fixed stator coordinates can be written by means of space vectors as in [21]:

$$\underline{u}_S(t) = R_S \underline{i}_S(t) + \frac{d\underline{\Psi}_S(t)}{dt}$$

(2.2)

where

$$\underline{u}_S(t) = k\left(u_{S1}(t) + u_{S2}(t)e^{j\gamma} + u_{S3}(t)e^{2j\gamma}\right)$$

(2.3)

<u>Remark:</u> For the definition of space vectors, different scaling factors can be used. In this thesis, the scaling factor $k = 1$ is used, as in [21]. Frequently, in other textbooks $k = 2/3$ is used. With $k = 2/3$ the projection of a space vector to a winding axis of the machine directly gives the instantaneous value of the physical quantity (i, u, Ψ etc.). Using $k = 1$ the physical quantity is obtained by multiplying the projection of the space vector by $2/3$.

Similar equations to (2.3) are also valid for the current and flux space vectors. The electrical angle between the stator phases is $\gamma = 2\pi/3$. The star connection of the motor and the sinusoidal EMF leads to the following constraints regarding the phase currents and the linkage fluxes:

$$i_{S1}(t) + i_{S2}(t) + i_{S3}(t) = 0$$
$$\Psi_{S1}(t) + \Psi_{S2}(t) + \Psi_{S3}(t) = 0$$

(2.4)

The space vector of the stator flux linkage is defined as:

$$\underline{\Psi}_S(t) = L_S \underline{i}_S(t) + \frac{3}{2}\Psi_{PM}(x(t))e^{j\beta(t)}$$

(2.5)

Ψ_{PM} is the position dependent value of the PM flux linkage with the stator, L_S is the stator inductance and β is the electrical angle of the vehicle.

$$\beta(t) = \frac{\pi}{\tau}x(t)$$

(2.6)

Using (2.5) and (2.2) the real and imaginary components of the voltage space vector in the fix stator reference frame (ab) are:

$$u_{Sa}(t) = R_S i_{Sa}(t) + L_S \frac{di_{Sa}(t)}{dt} - \frac{3\pi}{2\tau} \Psi_{PM}(x(t)) \sin(\beta(t)) v(t)$$

$$u_{Sb}(t) = R_S i_{Sb}(t) + L_S \frac{di_{Sb}(t)}{dt} + \frac{3\pi}{2\tau} \Psi_{PM}(x(t)) \cos(\beta(t)) v(t)$$

(2.7)

where $v(t)$ is the speed of the vehicle.

In order to simplify the non-linear equations in (2.7), the voltage space vector will be shifted in a system of coordinates (dq), which follows the magnetic field of the vehicle. The voltage equations in (dq) frame become:

$$u_{Sd}(t) = R_S i_{Sd}(t) + L_{Sd} \frac{di_{Sd}(t)}{dt} - \frac{\pi}{\tau} L_{Sq} i_{Sq}(t) v(t)$$

$$u_{Sq}(t) = R_S i_{Sq}(t) + L_{Sq} \frac{di_{Sq}(t)}{dt} + \frac{\pi}{\tau} L_{Sd} i_{Sd}(t) v(t) + \underbrace{\frac{3\pi}{2\tau} \Psi_{PM}(x(t)) v(t)}_{e_{Sq}}$$

(2.8)

Theoretically the EMF exists only in the q-axis and has the value of e_{Sq}. The instantaneous power at the motor terminals is:

$$p_i(t) = u_{S1}(t) i_{S1}(t) + u_{S2}(t) i_{S2}(t) + u_{S3}(t) i_{S3}(t)$$
$$= \frac{2}{3} \Re\{\underline{u}_S(t) \underline{i}_S^*(t)\}$$

(2.9)

The equation (2.9) can be written in (dq) reference frame

$$\underline{u}_S(t) = u_{Sd}(t) + j u_{Sq}(t)$$
$$\underline{i}_S^*(t) = i_{Sd}(t) - j i_{Sq}(t)$$
$$p_i(t) = \frac{2}{3}(u_{Sd}(t) i_{Sd}(t) + u_{Sq}(t) i_{Sq}(t))$$

(2.10)

By inserting (2.8) in (2.10), the instantaneous power is determined by:

$$p_i(t) = \underbrace{\frac{2}{3} R_S (i^2{}_{Sd}(t) + i^2{}_{Sq}(t))}_{p_{ohm}(t)} + \underbrace{\frac{2}{3}\left(L_{Sd} i_{Sd}(t) \frac{di_{Sd}(t)}{dt} + L_{Sq} i_{Sq}(t) \frac{di_{Sq}(t)}{dt} \right)}_{p_{mag}(t)} +$$

$$\underbrace{\underbrace{\frac{2\pi}{3\tau}(L_{Sd} - L_{Sq}) i_{Sd}(t) i_{Sq}(t) v(t) + \frac{\pi}{\tau} \Psi_{PM}(x(t)) i_{Sq}(t) v(t)}_{p_{rel}(t)}}_{p_{mech}(t)}$$

(2.11)

This power is split into ohmic power losses $p_{ohm}(t)$, power stored in the magnetic field $p_{mag}(t)$ and the mechanical power $p_{mech}(t)$ transferred to the vehicle.

The reluctance component $p_{rel}(t)$ of the mechanical power is zero if the current i_{Sd} is controlled to zero or if the motor has no saliency. The reluctance motor, which has no excitation field, uses only the reluctance component to produce the thrust force. The relation between the mechanical power and the thrust force is:

$$P_{mech} = v F_{th} \tag{2.12}$$

If we consider the reluctance force to be zero, the relation of the thrust force is:

$$F_{th} = \frac{\pi}{\tau} \Psi_{PM}(x) i_{Sq} = k_f i_{Sq} \tag{2.13}$$

The effect of this thrust force on a vehicle of mass M_v is:

$$M_v \frac{dv}{dt} = F_{th} - F_d \tag{2.14}$$

The characteristics of the PMLSM are summarised in the block diagram of Fig. 2.2.

The force F_d, seen by the control system as a perturbation force, is the sum of three forces:
- The friction force of the linear guiding system, which depends on the vehicle's speed [22]
- The periodical cogging force, which is produced by the interaction between the PMs and the slotted stator (which was neglected in the fundamental wave model)
- The load force

The cogging force depends on the electrical angle β. Skewing the PMs diminishes its amplitude. The bandwidth of the speed control loop must be big enough in order to compensate the cogging force, especially at high speeds. Otherwise compensation methods as in [23] would be necessary.
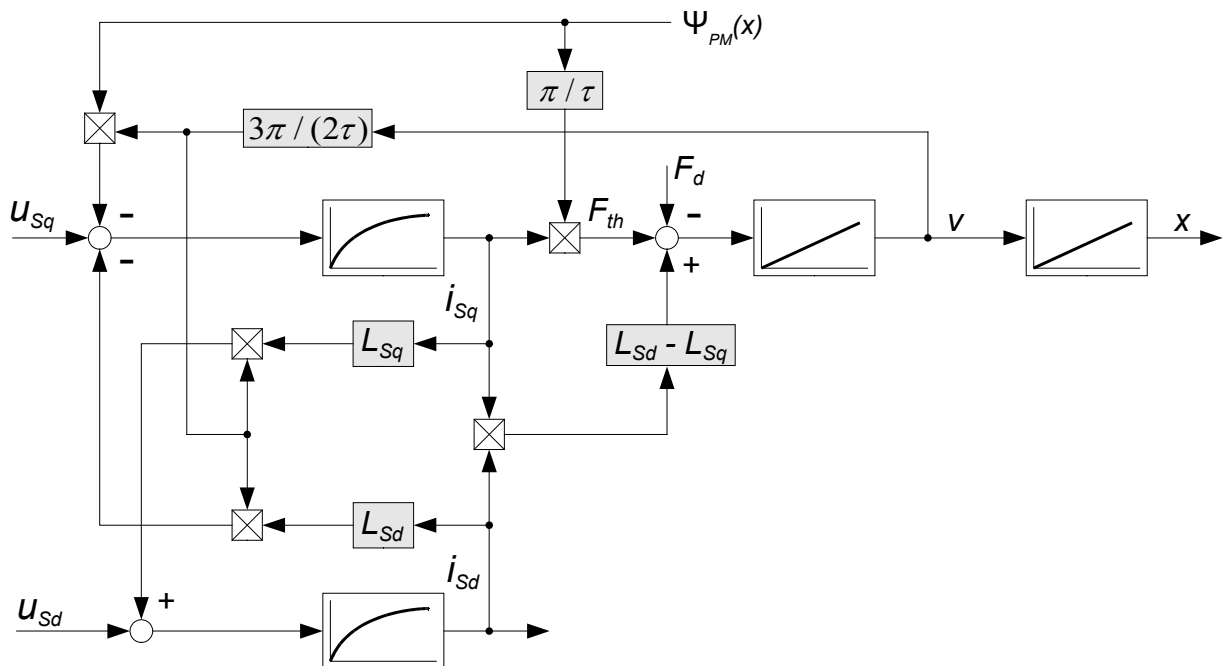

Figure 2.2 Block diagram of the PMLSM

For this application the current i_{Sd} is controlled to zero, because it doesn't contribute to the thrust force generation, as the saliency is negligible small. The cogging force effect of the motor chosen for the experimental set-up is very small, so that no compensation was necessary.

2.2. Field oriented control and modulation method

The equations describing the behaviour of the PMLSM in (dq) reference frame are the basis for the design of the current, speed and position control loops. The variables of these equations have DC values in steady state and lead to a decoupled control system similar to the one of a DC motor. The proportional position controller, the PI speed controller and the PI current controller form a cascaded control system, which is the classical method for the control of electrical drives. The current control loop is the inner loop and is therefore very important for the dynamic of the whole system. The design of the (dq) current controllers starts from equations in (2.8), written as:

$$T_{Sd}\frac{di_{Sd}(t)}{dt}+i_{Sd}(t)=\frac{1}{R_S}u_{Sd}(t)+\underbrace{\frac{\pi}{\tau}T_{Sq}i_{Sq}(t)v(t)}_{pd}$$

$$T_{Sq}\frac{di_{Sq}(t)}{dt}+i_{Sq}(t)=\frac{1}{R_S}u_{Sq}(t)-\underbrace{\left(\frac{\pi}{\tau}T_{Sd}i_{Sd}(t)v(t)+\frac{1}{R_S}\frac{3\pi}{2\tau}\Psi_{PM}\left(x(t)\right)v(t)\right)}_{pq}$$

(2.15)

are the time constants of the current control loops.

$T_{Sd}=\dfrac{L_{Sd}}{R_S}\approx T_{Sq}=\dfrac{L_{Sq}}{R_S}$ The current controllers for the d- and q-components are running in parallel and are designed in the same manner. In (2.15), both equations are non-linear due to the coupling terms pd and pq, which are acting as perturbations for the control loops. The second term of the component pq, which depends only on the speed, is considered a stationary perturbation, so that only the current dependent term is important for the dynamic performance of the controller. At low speeds, the influence of the perturbations can be very well compensated by the integrative component of the controllers. At high speeds, depending on the characteristics of the PI controller and of the motor, a good dynamic performance can be also achieved without using feedforward compensation.

Fig. 2.3 shows the current control loops, where the behaviour of the motor and of the inverter is
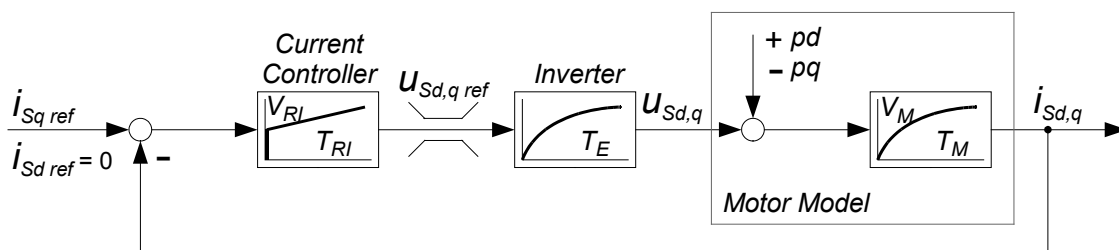

Figure 2.3 (dq) current control loops

associated with a PT1 element. In (2.16), T_0 represents the sampling time (100 µs).

$$PT_{1,LSM} = \frac{V_M}{T_M s + 1} \qquad PT_{1,INV} = \frac{1}{T_E s + 1}$$

$$\text{(Motor)} \qquad \qquad \qquad \text{(Inverter)}$$

$$V_M = \frac{1}{R_S} \; ; \; T_M = T_{Sd}, T_{Sq} \qquad T_E = \frac{3}{2} T_0 \tag{2.16}$$

The transfer function of the current controller is:

$$K(s) = V_{RI} \frac{T_{RI} s + 1}{T_{RI} s} \tag{2.17}$$

The controller is designed by using the method of amplitude optimum, where the time constant of the controller must compensate the time constant of the motor $T_{RI} = T_M$, so that the closed-loop transfer function will describe a second order system:

$$G_0(s) = \frac{1}{\dfrac{T_M T_E R_S}{V_{RI}} s^2 + \dfrac{T_M R_S}{V_{RI}} s + 1} = \frac{1}{\dfrac{1}{\omega_0^2} s^2 + \dfrac{2D_0}{\omega_0} s + 1} \tag{2.18}$$

where ω_0 is the natural frequency and D_0 is the damping of the control loop. From (2.18) the gain of the controller is determined for the desired damping value. The output values of the current controllers are limited according to the maximal value of the voltage space vector $\underline{u}_S$.

The d-component of the voltage will have priority over the q-component, as shown in (2.19).

$$u_{Sd,\max} = \left| \underline{u}_{S,\max} \right| \qquad u_{Sq,\max} = \sqrt{u_{Sd,\max}^2 - u_{Sdref}^2}$$

$$u_{Sd,\min} = -\left| \underline{u}_{S,\max} \right| \qquad u_{Sq,\min} = -\sqrt{u_{Sd,\max}^2 - u_{Sdref}^2} \tag{2.19}$$
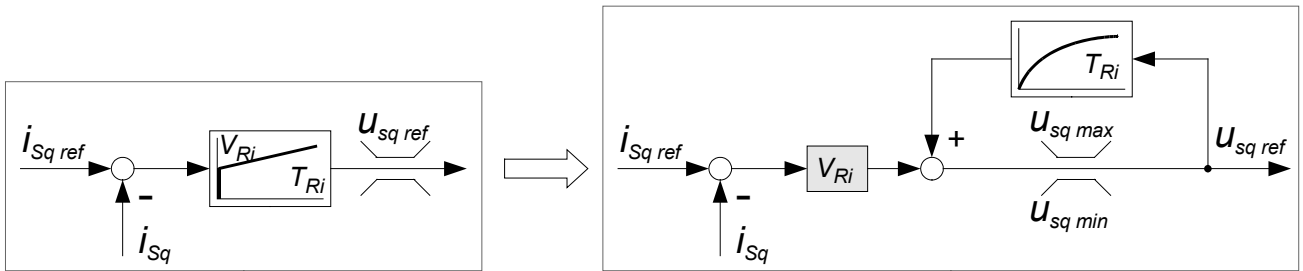

Figure 2.4 PI controller with anti-windup

The value of $\left| \underline{u}_{S\max} \right|$ depends on the modulation method used. A simple, code efficient way to design the modulator is to use directly the phase reference voltages $u_{S1ref}, u_{S2ref}, u_{S3ref}$, generated as in Fig. 2.8. For a good utilization of the inverter's voltage limits, the star point u_{S0} from Fig. 2.5 can be shifted from its zero position by using an offset voltage, as shown in Fig. 2.6. The switching time for each phase will be:

$$t_{onY} = \left(\frac{1}{2} - \frac{u_{SYref} + u_{ofs}}{U_D} \right) T_0 \; ; \; (Y = 1, 2, 3) \tag{2.20}$$

In (2.20) t_{onY} is the on time of the low side IGBTs (as defined in the list of symbols), U_D is the DC-link voltage and u_{ofs} is the offset voltage.
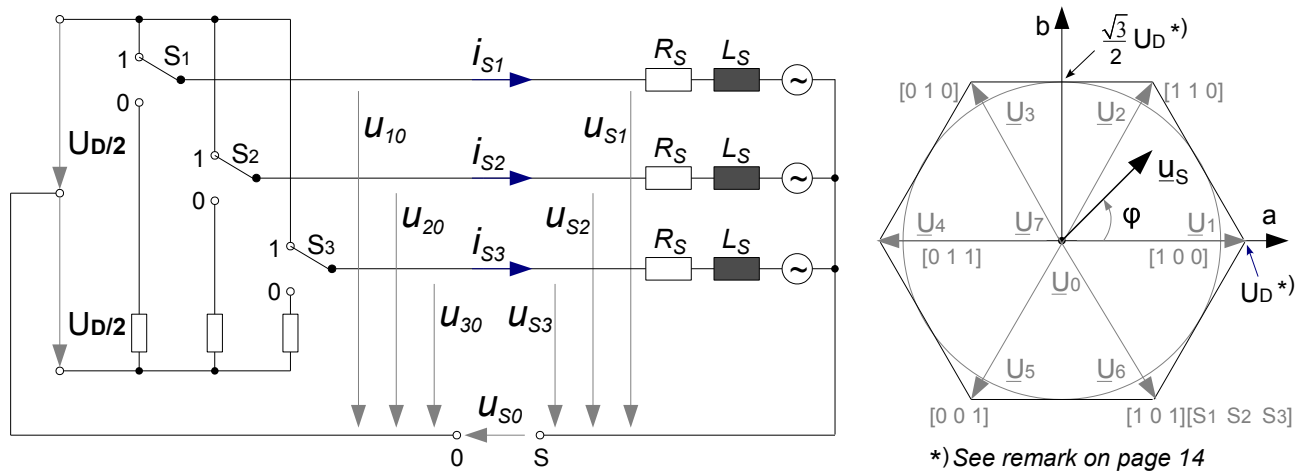

Figure 2.5 Equivalent inverter circuit

There are many modulation methods depending on how many inverter legs are switching in one PWM cycle and on how the offset voltage is being calculated [24], [25], [26], [27]. The average value of the modulation index and the current measurement by shunts are important factors in selecting the modulation method, as it will be illustrated in the fifth chapter.

Fig. 2.7 shows the simulated offset voltage for two carrier based modulation methods. For both methods, the maximal values of the space vector voltage and of the phase voltages are:
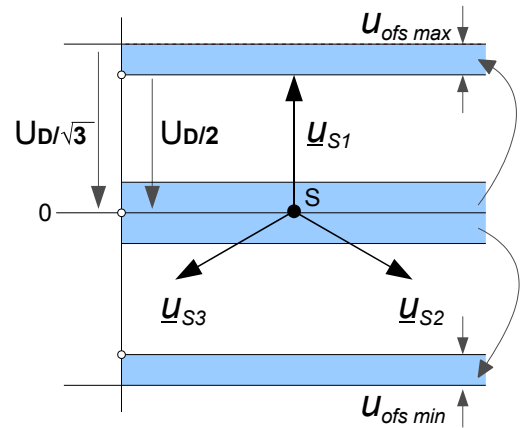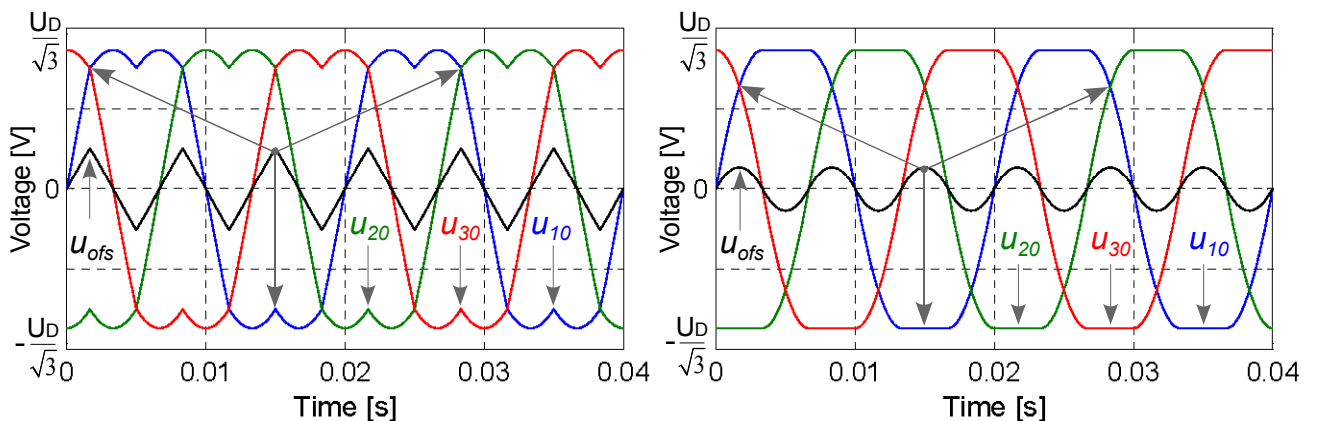

Figure 2.6 The offset voltage

$$\left|\underline{u}_{S,\max}\right| = \frac{\sqrt{3}}{2}U_D \quad ; \quad \left|\underline{u}_{SY,\max}\right| = \frac{U_D}{\sqrt{3}} \quad ; \quad (Y = 1, 2, 3) \tag{2.21}$$

a) Carrier based modulation with the offset voltage calculated as in (2.22)

b) Carrier based modulation with the offset voltage calculated as in (2.23)

Figure 2.7 Low frequency content of the offset voltage and the inverter's output voltages

The offset voltage is calculated according to (2.22) for the modulation of Fig. 2.7a and to (2.23) for the modulation of Fig. 2.7b ([27], [28]).

$$u_{ofs} = -\frac{(u_{\max S} + u_{\min S})}{2} \quad ; \quad \begin{cases} u_{\max S} = \max\left\{u_{S1ref}, u_{S2ref}, u_{S3ref}\right\} \\ u_{\min S} = \min\left\{u_{S1ref}, u_{S2ref}, u_{S3ref}\right\} \end{cases}$$

(2.22)

$$u_{ofs} = \begin{cases} \dfrac{|u_S|}{\sqrt{3}} - u_{\max S} \quad ; \quad u_{\max S} + u_{\min S} > 0 \\ -\dfrac{|u_S|}{\sqrt{3}} - u_{\min S} \quad ; \quad u_{\max S} + u_{\min S} < 0 \end{cases}$$

(2.23)

For the design of the speed control loop, the current control loop of the q-component is approximated by a PT1 element.

$$G_I(s) = \frac{1}{T_{EI}s + 1} \quad ; \quad T_{EI} = 4D_0^2 T_E$$

(2.24)

Fig. 2.8 shows the block diagram of the entire cascaded control. In order to avoid a big speed overshoot, the speed reference value is filtered by means of a first order low-pass filter. The design of the speed and position control loops is presented in the appendix.

As it can be seen from Fig. 2.8, the FOC requires the knowledge of the actual position and speed of the vehicle. A high-resolution sensor can measure the position and then the speed is obtained by using derivative and filtering operations. If the sensor's resolution is not satisfactory, a good

Figure 2.8 Block diagram of the cascaded control in field coordinates for the PMLSM

speed calculation is still possible by using a speed observer based on the mechanical motor model. For electrical drives, there is generally nowadays desired to implement sensorless control strategies in order to reduce costs. And this is even more evident in the case of linear drives, where the sensor system would have to cover the entire length of the track. There are two main sensorless control strategies:

- EMF-based control strategy
- Control strategy based on magnetic anisotropies

The first one doesn't work at standstill but is relative simple to implement, while the second one works theoretically at standstill but is more complex and quite challenging especially at high loads [29], [30], [31], [32]. For the applications that this work focuses upon, the EMF-based method alone is satisfactory. The implementation of the EMF-based control and the experimental results for both sensor-based and sensorless control are presented in detail in chapter 6.

2.3. Hard real-time communication demands between the distributed controllers

The block diagram from Fig. 2.8 is implemented in all distributed control units (DCUs) of the system. During the transition period of a vehicle across two adjacent stator segments, both involved DCUs have to control the current of the equation (2.13) in such a way that the desired resulting force is developed at the vehicle, which has to assure a smooth, bump-less transition. Therefore, a data exchange between the adjacent DCUs must take place within each current control cycle during the transition period. This period contains three main states:
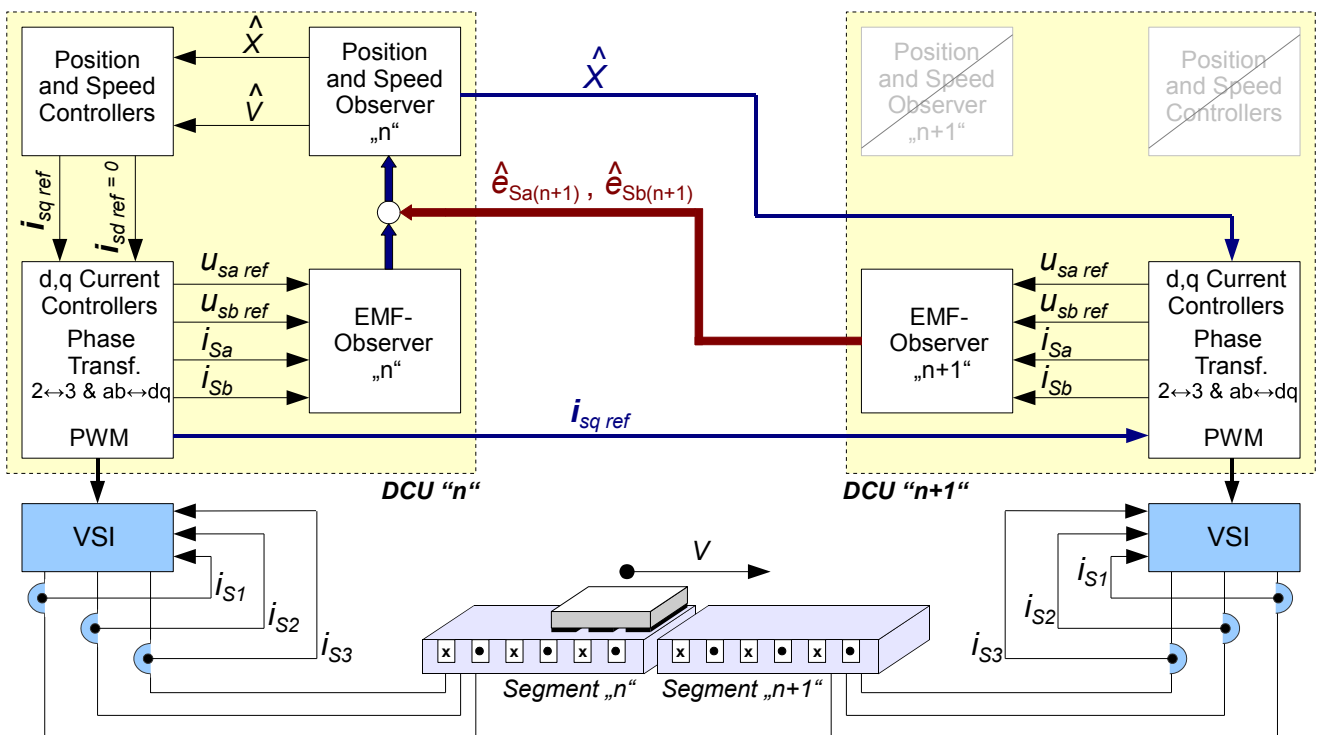

Figure 2.9 Data transfer between the DCUs at the beginning of a transition period

- The first state begins shortly before the vehicle reaches the edge of one segment and is heading towards the neighbour segment as shown in Fig. 2.9. In this figure the case of an EMF-based sensorless control is considered. The current controllers of both stator segments must be active, but only one DCU is controlling the position and the speed of the vehicle. It is a master-slave relation where DCU "n" is the master and DCU "n+1" is the slave. DCU "n+1" has to control the current according to the received reference value sent by DCU "n". Similarly, only the position and speed observer of the master DCU is active but this needs the EMFs from both segments. This state ends when the vehicle reaches the middle point between the stator segments.

- The second state begins when the vehicle reaches the central position between two stator segments and ends after one control cycle. Within one control cycle, the master-slave roles of DCU "n" and DCU "n+1" interchange, so that DCU "n+1" becomes the master. This is also the state where the maximum amount of data has to be exchanged. The final values of the state variables for speed and position control must be transferred from DCU "n" to DCU "n+1" where they are set as initial values, as shown in Fig. 2.10. For the position and speed control the state variables are the integrator value of the PI speed controller and the value of the filtered speed reference. For the position and speed observer, the state variables are the estimated speed and position values.

- The third state follows immediately after the second state and ends shortly after the vehicle completely leaves segment "n". Now DCU "n" has to control the current according
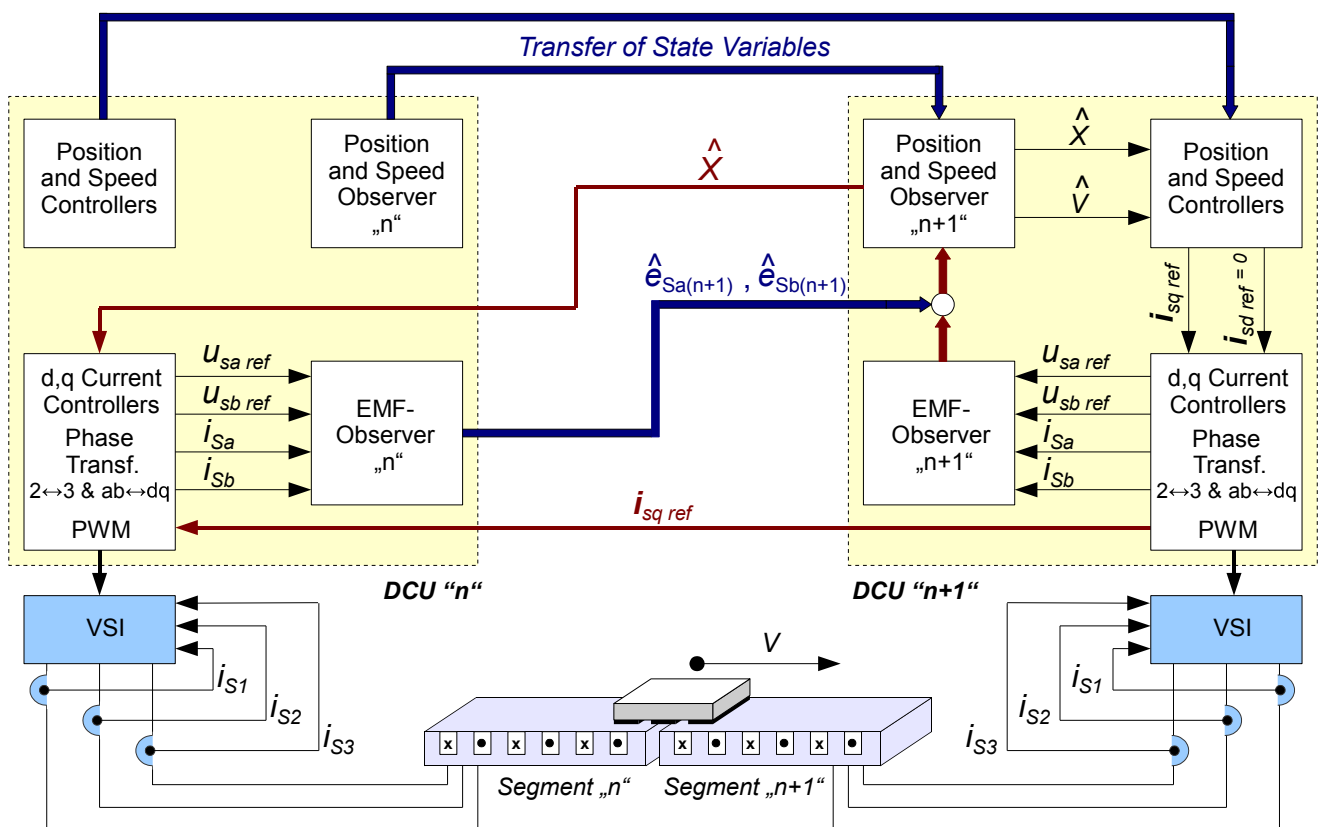

Figure 2.10 Maximum data transfer between two adjacent DCUs during a transition period

to the received reference value sent by DCU "n+1". Also here both EMF-observers must be active, as shown in Fig. 2.11.
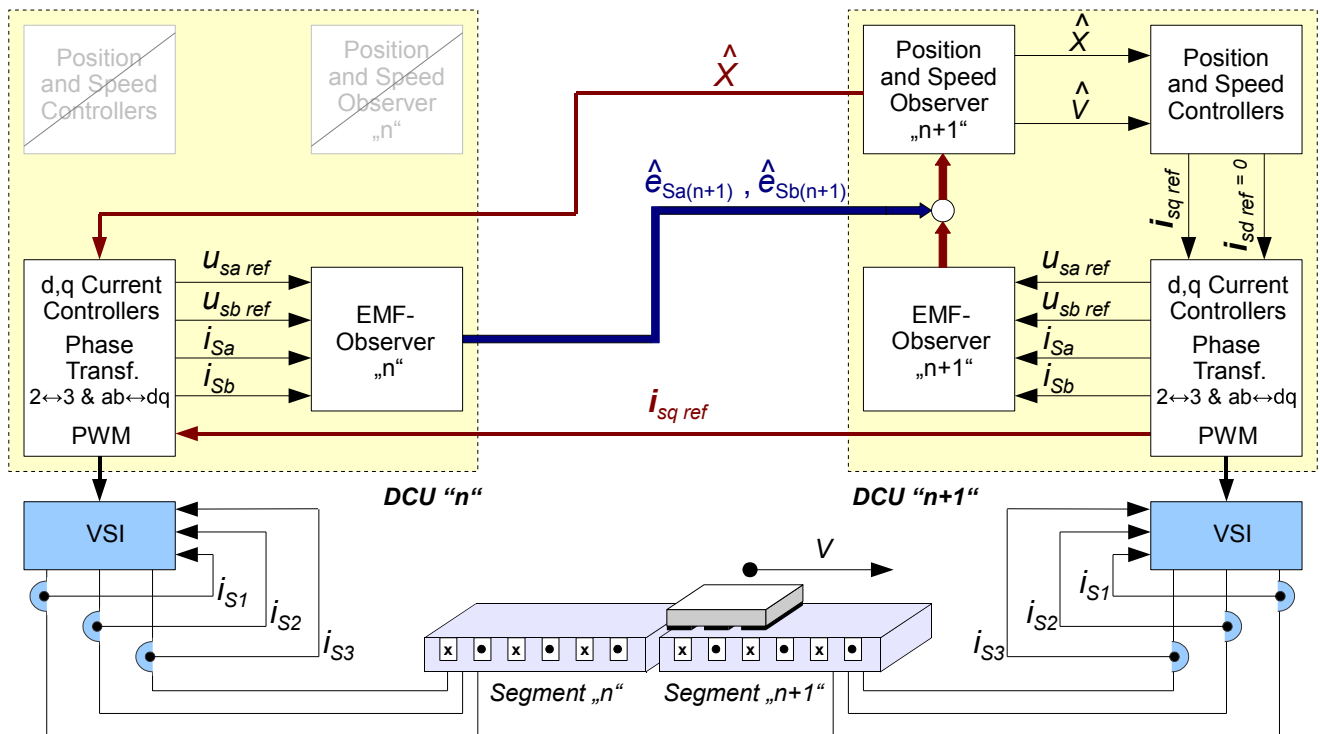

Figure 2.11 Data transfer between the DCUs at the end of a transition period

Regarding the master-slave relation at the level of the control strategy, the mastership moves according to the vehicle's position and an additional slave control function is invoked while the vehicle transits to the next stator segment. As an arbitrary number of vehicles may be simultaneously in a transition period, a high communication bandwidth will be required. For a highly scalable system any industrial fieldbus will not be able to fulfil this task. The necessary communication bandwidth can be only guaranteed by individual point-to-point connections between the adjacent DCUs. Any DCU must be able to communicate with both adjacent units, on its left and on its right respectively. It must poses therefore two independent and relative fast communication channels. At the application layer this communication was realized by means of the SPI (Serial Peripheral Interface) protocol, as the DCU has two SPI compatible units. At the physical layer the differential data transfer protocol RS485 was used. The implementation of this point-to-point connection is presented in chapter 3.

2.4. Motion coordination and monitoring

At the beginning of this chapter the main tasks of the Central Control Unit (CCU) were mentioned, namely: the cyclical data transmission of new position reference values to the DCUs (motion coordination) and the cyclical status data reading from the DCUs (system monitoring). Inside the control system we distinguish between two real-time communication loops: the superimposed loop in milliseconds cycles between the CCU and the DCUs and the hard real-time communication

loop executed at every sampling interval of 100 μs between any two adjacent DCUs. Both communication loops must run independently so that the CCU must be able to access any DCU in the system, at any moment, without stopping or delaying a running communication between this and another DCU. Similarly, all DCUs must be able to provide actual status data to the CCU at any time instant. For this reason, the control system needs another communication bus beside the SPI-based one. Regarding the scalability of the system, a standard industrial fieldbus is used therefore for motion coordination and monitoring, which must allow in the first place the connection of a large number of communication nodes to the control network and a high communication bandwidth. There are also other requirements, which have to be fulfilled by this fieldbus, such as:

- It must allow high topology flexibility. Line, tree and star connections of the communication nodes should be possible without additional node controllers or cabling
- The hardware complexity and costs must not be high.
- The idea of modularity must be also reflected in the easy addition or removal of modules ("plug & play"), facilitating an easy system set-up and maintenance.
- It must allow a simple controller interface.
- Error detection at the physical and the application layers are mandatory.
- At the application layer, a protocol for off-line data transfer to/from the DCUs must be available. This will allow the parameterisation and configuration of the DCUs. Data upload from the DCUs will enable the off-line analysis of state variables saved at every 100 μs.
- It should support Internet protocols and be compatible with other standard fieldbuses. It should be also well established in the field of industrial automation.
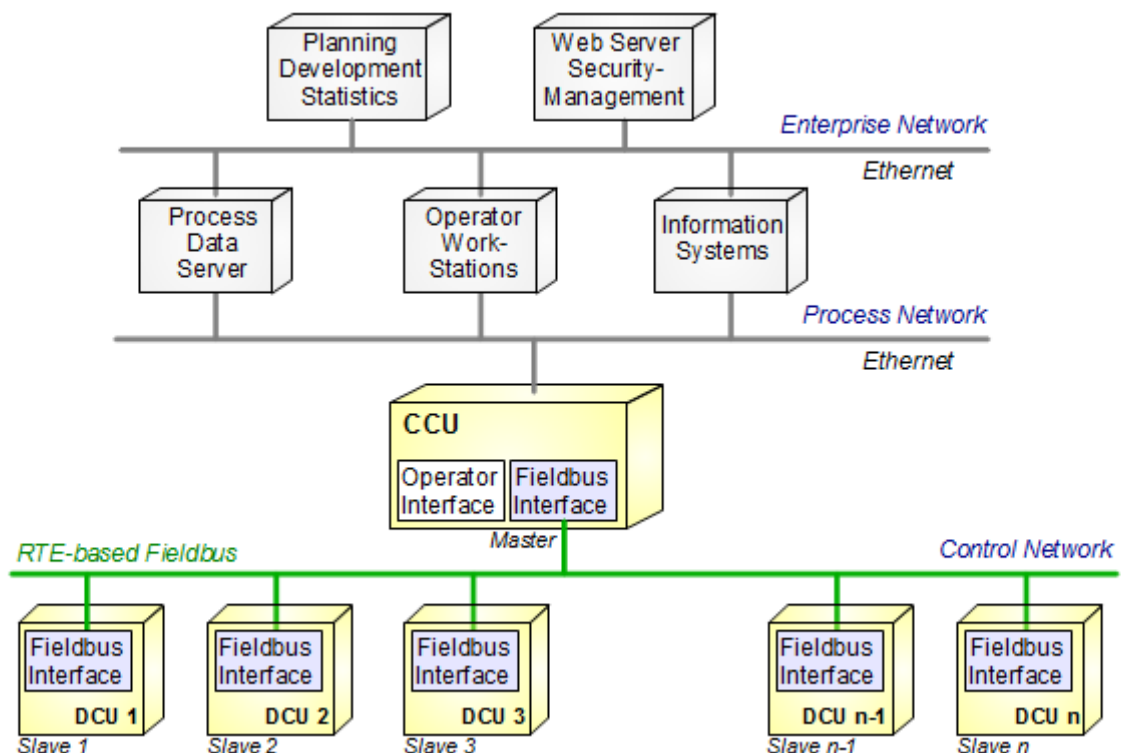

Figure 2.12 Network connection in an industrial automation system

Over the last years RTE (Real-Time Industrial Ethernet) solutions for implementing industrial fieldbuses gained popularity, so that nowadays there are many RTE-based protocols available [33]. The importance of Ethernet in the present industrial automation systems is shown in Fig. 2.12. Even though at the beginning Ethernet was not considered an appropriate solution due to its lack of real-time performance, the modification of this protocol at the upper levels of the OSI/ISO model lead to new real-time capable, wire-based, protocols [34]. Taking in consideration the requirements listed above and the actual trend for industrial network solutions nowadays, an RTE-based protocol was used also in this work, namely EtherCAT. EtherCAT stands for Ethernet for Control Automation Technology and is one of the most powerful industrial fieldbus available now [35]. Due to the 100BASE-TX fast-Ethernet standard (specified in the IEEE 802.3), used at the physical layer, high bit-rates of 100 Mbps are possible. It allows the connection of up to 65535 devices to the control network. At the fieldbus level there is a fix master-slave relation between the CCU (EtherCAT master) and the DCUs (EtherCAT slaves). This protocol is completely hardware implemented. The fieldbus interface of the master is a standard network card, so that a standard PC can represent the CCU. The same network card is used to interact with both process and control networks. No additional hardware is requested for the master. The fieldbus interface of the DCU is implemented by EtherCAT ASICs.

The characteristics of EtherCAT and its role in the proposed system are presented in detail in chapter 4.

3. Point-to-point connection between the distributed controllers

This chapter describes the operation of the data transfer between neighbouring DCUs, which was outlined in the figures 2.9, 2.10 and 2.11. A more detailed description of the hardware, which is used for this communication, is given later in the chapter "Experimental Set-up".

3.1. SPI data transfer

SPI describes a synchronous and serial data bus. It was initially defined by *Motorola*, as a simple and cost-effective method to transmit data between microcontrollers and peripherals like ADCs and sensors. Along the same SPI-bus, the communication between two or more microcontrollers is also possible. The data transfer is based on the master-slave principle. Data can be transmitted at high rates (up to tens of Mbps) in full-duplex or half-duplex mode. The communication nodes on a SPI-bus are typically connected over four logic signals:

- A clock signal (CLK), which is generated by the master
- A data signal (MOSI) from the master towards the slave(s)
- A data signal (MISO) from a slave towards the master
- A slave-select signal (SS), required if there is more than one slave-node on the bus.

SPI was not patented by *Motorola* (it is license-free) and is not standardized. The user can decide upon the phase, polarity and rate of the clock signal, the size and shift operations of the incoming and outgoing data, the number of slaves and slave-select signals and upon the communication mode (half- or full-duplex).
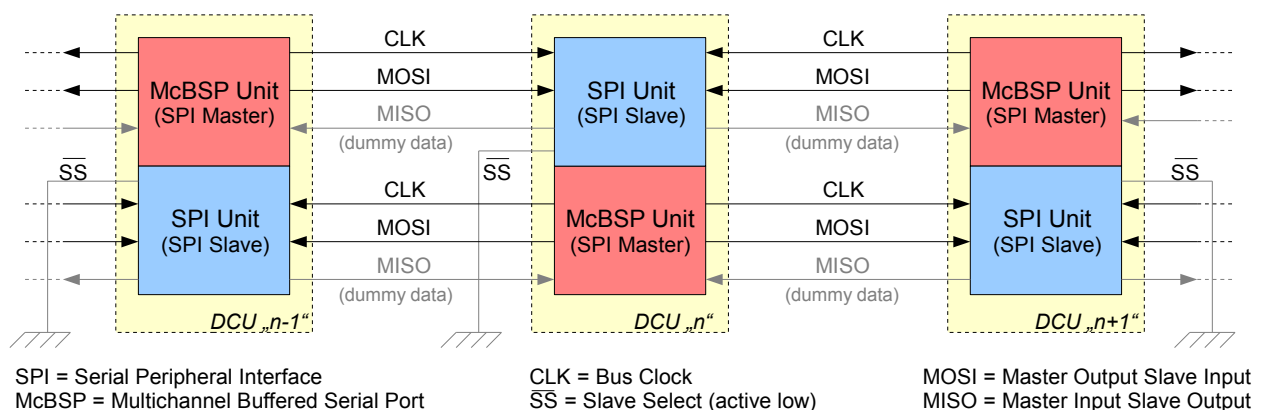

Figure 3.1 SPI configuration for the distributed controllers

The DSP TMS320F2812 of a DCU in this project contains two SPI-compatible units, which are used to implement the connection with its adjacent DCUs. These units are: the SPI unit and the McBSP unit, presented in the Fig. 3.1. McBSP is a synchronous data transmission protocol, which besides the SPI-compatibility has also extended features, such as independent clocking for sending and receiving data, multi-channel selection and frame synchronization [36].

The McBSP unit is here always working as a master and the SPI unit always as a slave. This was the only configuration, for which the maximal speed of 12.5 Mbps, allowed by the used DSP-board, could be reached. The slave-select signal was not used, because each slave unit is connected with two master units. This active-low signal of the slave units was tied to ground, so that a slave unit will always shift out its data if it receives a valid clock signal. A slave unit can exchange data only with one master at a time. The selection of the active master unit is made by a communication protocol with the help of four general-purpose I/O (GPIO) signals of the DSP. These signals assure also that no short-circuits occur on the bus, as described later in the Figs. 3.4 and 3.5.

The master initialises the data transfer by sending the clock signal. The data are transferred as 16-bit words. Both the master's and the slave's shift registers will shift their bits in and out according to the phase and polarity of this clock. Here, the clock signal is inactive-low and has no phase delay. The data is transmitted on the rising edge and received on the falling edge of the clock.

Fig. 3.2 shows the ideal case of the data transfer at a clock frequency of 12.5 MHz, where signal delays due to the transmission medium have been neglected. The slave receives the rising clock
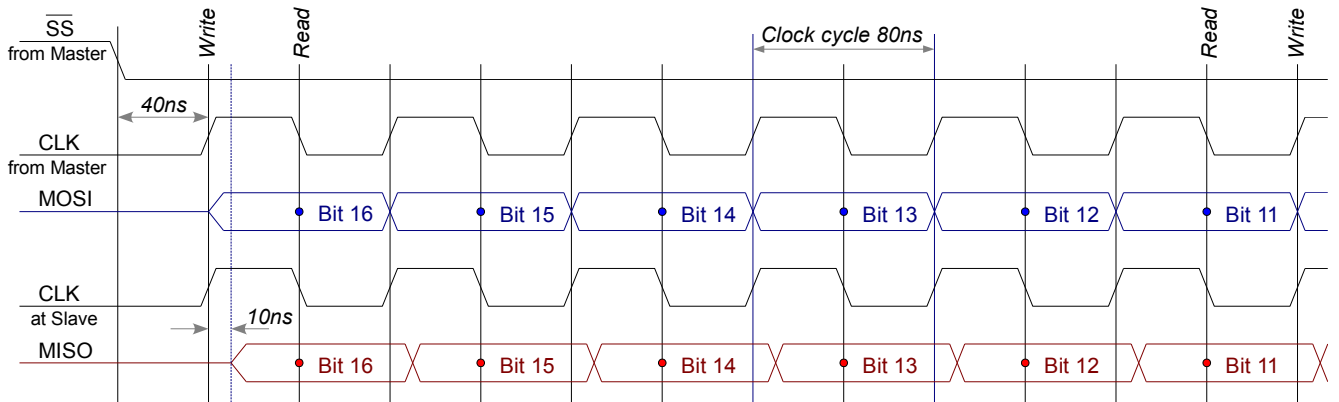

Figure 3.2 Ideal full-duplex communication process disregarding delays

pulses generated by the master with no delay and after maximum 10 ns puts its data on the bus. Along with the falling edge of the clock, both master and slave read the data. After 16 clock pulses the master and the slave successfully exchange a word. This is a full-duplex communication mode. The data transfer process of Fig. 3.2 corresponds rather to direct connections (i.e. single ended transmission) over short PCB routes or cable lengths and cannot be used in this case. In our set-up, due to reasons of EMC and longer cable distances, data must be transmitted differentially over a one-meter long cable. We selected the differential signalling standard RS485 for the physical layer of this communication. The propagation delay inserted by the RS485 transceivers and the cable had to be considered for a full-duplex communication. A full-duplex communication at 12.5 MHz cannot be realised with the maximal propagation delays shown in the following table.

RS485 Transmitter	Cable	RS485 Receiver
10 ns (maximal delay value)	5 ns	15 ns (maximal delay value)
Total maximal propagation delay: 30 ns		

This is explained in Fig. 3.3, where the first bit read by the master has a false value and the second bit read corresponds actually to the first bit send by the slave. All the bits read by the slave have correct values.
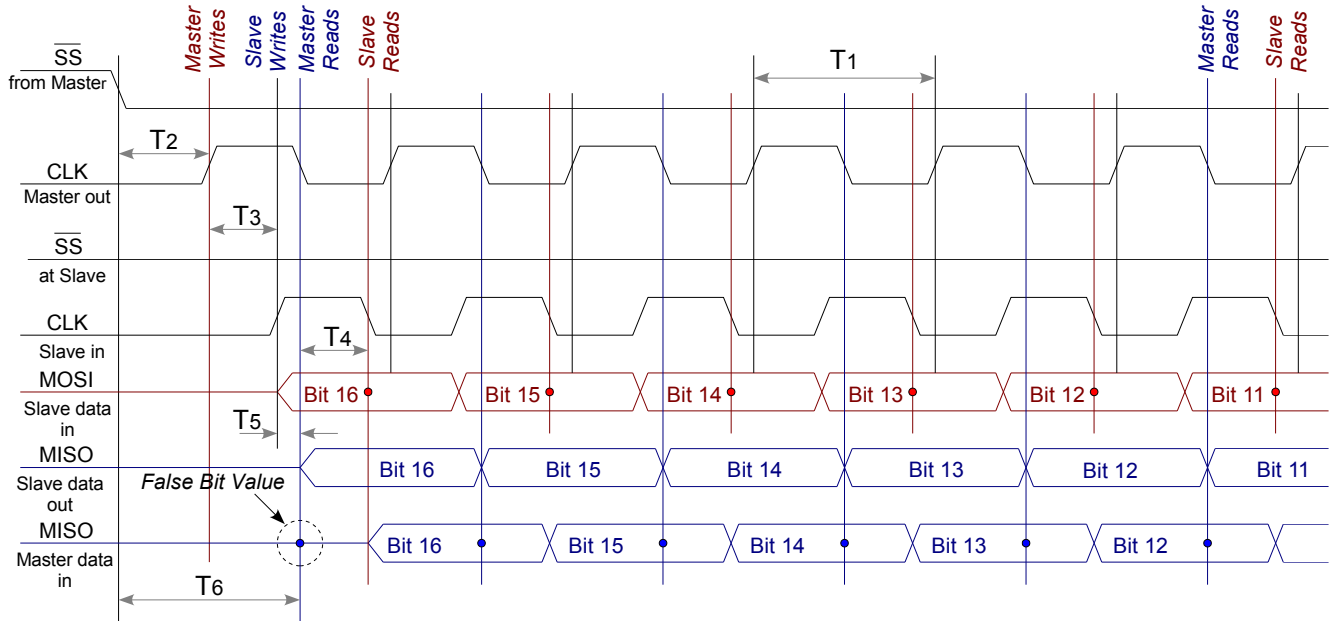

Figure 3.3 Full-duplex communication process considering real delays

Interval	Definition	Value
T_1	Clock cycle	80 ns
T_2	Delay time, SS low to CLK (master) high	40 ns
T_3	Total maximal propagation delay	30 ns
T_4	Minimal set-up time of a received bit before the falling edge of CLK (slave)	30 ns
T_5	Maximal delay time, CLK (slave) high to MISO valid	10 ns
T_6	Delay time, SS low to first bit read (master)	80 ns

Table 3.1 Timing specifications for a real full-duplex communication process

As the full-duplex communication with real delays inserted by the RS485 transceivers doesn't work properly, in this project two simultaneous half-duplex transmissions were developed.

3.2. Communication protocol

The communication between any adjacent DCUs is initiated and stopped according to the relative position of the vehicles. Fig. 3.4 shows the initial state where at the control stage only DCU "n" is controlling the vehicle. The stator segment "n+1" is passive and at this moment there is no communication process between the two DCUs. Concerning the communication, the SPI-compatible units as well as the RS485 transmitters and receivers are outlined in the Fig. 3.4.
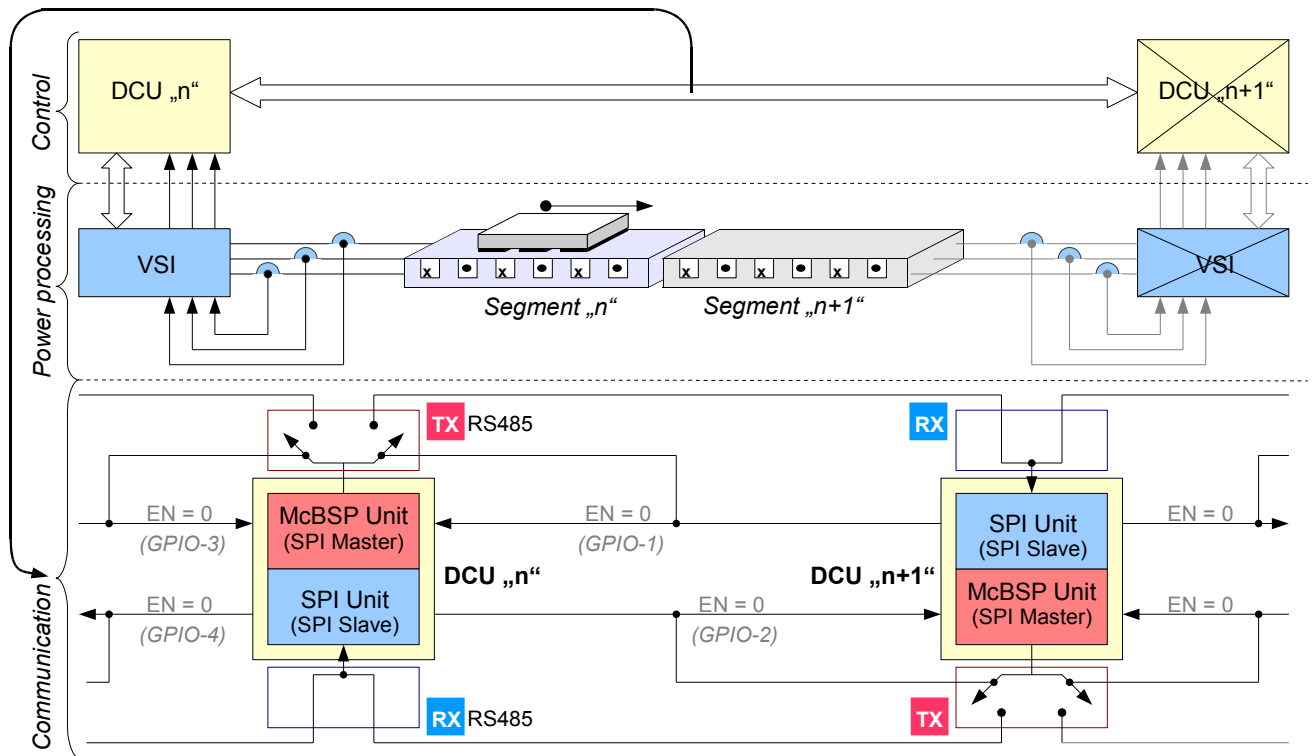
Figure 3.4 Initial state of the point-to-point communication process

The communication protocol is based on four GPIO signals, two outputs and two inputs on the side of each DCU. In order to avoid short circuits on the communication bus, the RS485 transmitters of a DCU can be enabled/disabled only by the corresponding adjacent DCUs, as shown in Fig. 3.4.
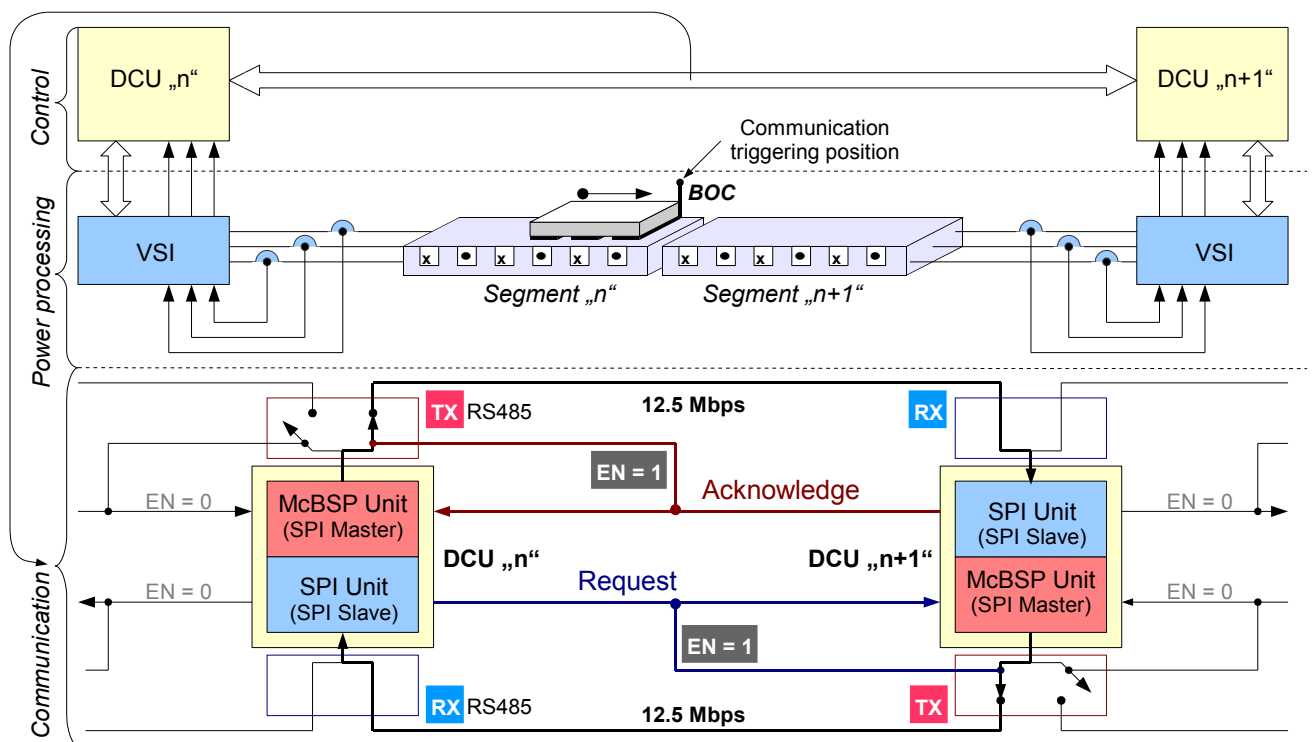

Figure 3.5 Full-duplex communication at 12.5 Mbps

When the vehicle reaches the communication triggering position, marked in Fig. 3.5, DCU "n" sends a communication request signal to DCU "n+1", which enables at the same time the transmitters of DCU "n+1" towards DCU "n". DCU "n+1" must assess then its actual communication state. If it is not already communicating with DCU "n+2", as assumed in Fig. 3.5, it has to acknowledge this communication request. Along with the acknowledge signal, the transmitters of DCU "n" towards DCU "n+1" are enabled.

The entire point-to-point communication process is presented in the flowchart of Fig. 3.6. The power stage of the modules is activated and deactivated also according to the relative position of
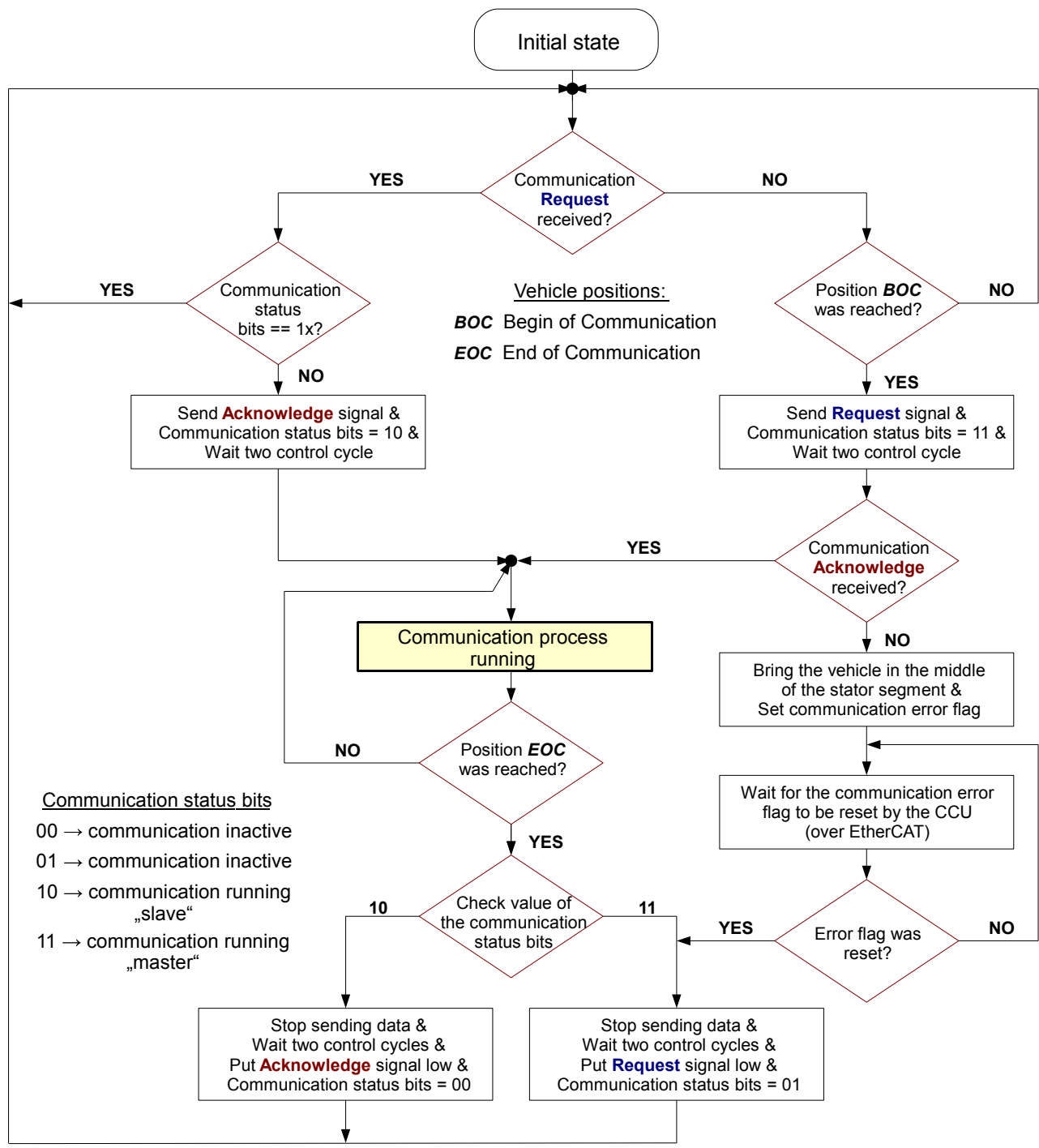
Figure 3.6 Flowchart of the position dependent point-to-point communication process

the vehicle, namely the power stage of module "n+1" is activated after the communication-triggering position has been reached. Immediately after activation, the force producing current of the module "n+1" is controlled to zero and there is no master-slave relationship between the modules. DCU "n+1" becomes a slave controller only after it acknowledges the communication request. Both DCUs exchange after this point simultaneously data (as shown in Figs. 2.9, 2.10 and 2.11) in both directions at the speed rate of 12.5 Mbps. This corresponds to a full-duplex communication, but with no problems concerning propagation delays [37]. The communication process ends when the triggering position "End of Communication (EOC)" is reached. The request and acknowledge signals are set low, so that the RS485 transmitters of both communication parts are disabled.

If DCU "n+1" communicates with DCU "n+2" and receives at this time a communication request from DCU "n", it will just ignore it. DCU "n" will not receive the acknowledge signal, so that after two control cycles will stop immediately the vehicle. Afterwards it will set the collision flag inside its state variable and will reposition the vehicle in the middle of the stator segment. The CCU must then reset this error flag before sending new position reference values to DCU "n". The CCU is informed about the communication process by means of three bits inside the status variables of all DCUs. One bit is a communication-error flag and the other two are reflecting the status of an error-free communication (Fig. 3.6). During normal operation, collision situations should not occur if the traffic planner of the CCU has been implemented correctly.

Remark: In the system, three levels of master-slave relations must be distinguished. At the level of control strategy, the mastership moves according to the position of the vehicle and a new slave controller is invoked when the vehicle transits to the next stator segment. For the SPI communication, each DCU accommodates one SPI-master unit and one SPI-slave unit. For the EtherCAT communication, which is introduced in the next chapter, an ordinary PC serves as EtherCAT master and all servo-controllers are EtherCAT slaves.

The CCU starts via EtherCAT the control cycles in all DCUs simultaneously. This means that the PWM-timers should run synchronized in all DCUs. But even though the electronic oscillators of the processors inside the DCUs are of the same type, very small differences between their frequencies still exists. This leads to a significant clock drift between them in few seconds.

Fig. 3.7 shows how are the data transmitted, received and read, when there is no clock drift between two adjacent DCUs. The intervals T_0, T_7, T_8, T_9 are defined in Table 3.2. It is supposed that the DCUs exchange the same amount of data (e.g. ten 16-bit variables) in each control cycle. In all DCUs the SPI-received data is red shortly after a control cycle begins and data is transmitted at the end of the cycle. Due to the synchronized transmit and read actions in both DCUs, the transmitted data by one DCU in a control cycle are always received before being read in the next control cycle by the other DCU. Fig. 3.8 shows the case when there is a clock drift between the DCUs and not all transmitted data are received before being read.
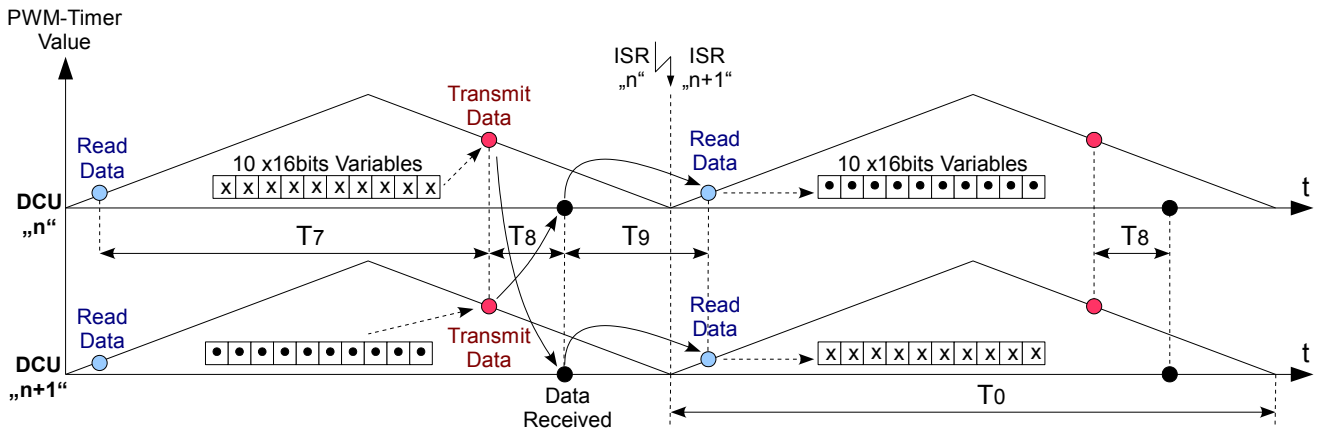
Figure 3.7 Data transfer with synchronized PWM-timers

DCU "n+1" starts transmitting data shortly before DCU "n" reads its receive-FIFO. Only half of this transmitted data will be available in the receive-FIFO at the time DCU "n" reads it. The other half of the data will be read by DCU "n" in the next cycle. In the worst case the read data are not consistent and there will be one cycle delay between transmitted and received data. A software procedure keeps the consistency of the data inside the 16-level receive-FIFO of a DCU. No more than ten variables are sent in a control cycle so that a FIFO overflow cannot occur.
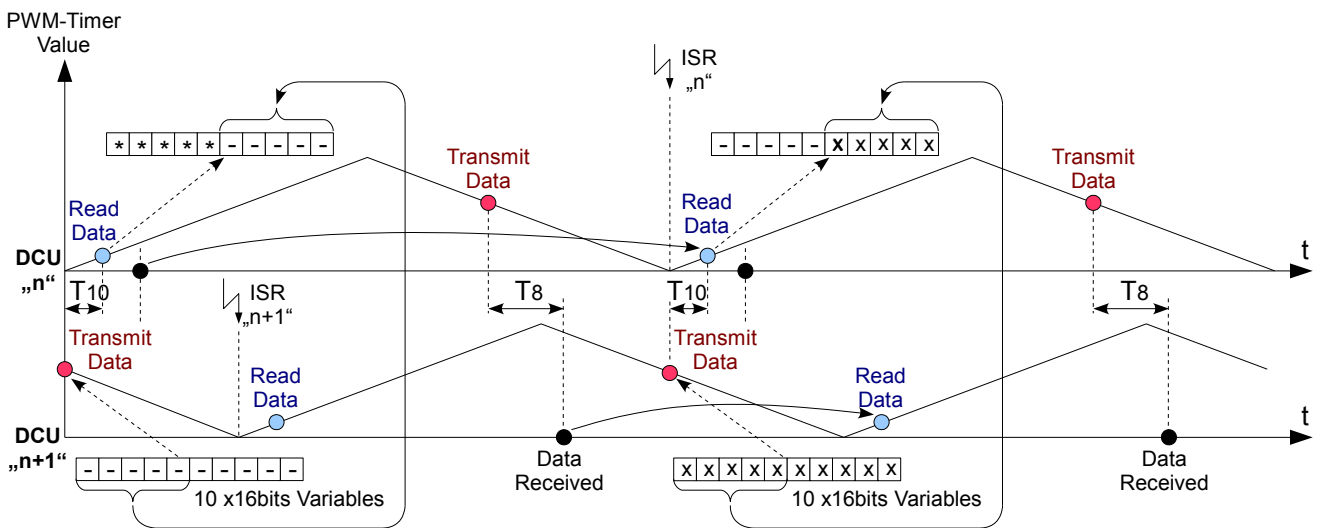

Figure 3.8 Data transfer with non-synchronized PWM-timers

Interval	Definition
T_7	Between the read and transmit actions inside one control cycle (constant)
T_8	Required to transmit 10 x 16bits at 12.5 Mbps (constant)
T_9	Between the read action and the time when data were written in the FIFO (variable)
T_0	Control cycle (constant)
T_{10}	Between the transmit action in one DCU and the read action in the adjacent DCU (variable)

Table 3.2 Timings related with data transfer and clock synchronization issues

Just one cycle delay in the communication process does not affect the control performance. The current control loop runs independently in all DCUs and they exchange only current reference values. The variation of the vehicle's speed and consequently the induced EMF are assumed to be zero within a current control cycle period (100 μs).

In principle, it would be possible to synchronize the PWM-timers of all DCUs by means of the EtherCAT fieldbus. Any EtherCAT slave device (here the DCU) contains a special clock unit, which can be used to synchronize, according to the IEEE 1588 standard, all the EtherCAT slaves to one reference clock hold by one slave (typically the first slave after the master in a network segment). But this would not be an advantage for this application. As a consequence of synchronization, the IGBTs of two adjacent VSIs controlling a vehicle would always commutate approximately at the same time instants. Due to the stray inductance of the common DC-link, synchronized switching would increase the spikes in the DC-link voltage and the stress on the IGBTs.

3.3. Data transmission at the physical layer

In this application, where the electronic of all DCUs is tied to the negative DC-link rail, the safety at the physical layer of the point-to-point data transmission is of concern, mainly due to common-mode voltage problems. In this subchapter these problems are identified based on simulation and experimental results and solutions are offered.

RS-485, also known as TIA/EIA-485, is a hardware standard, which describes a differential data transmission over long cables in multipoint communication networks [38]. It assures a high level of noise immunity and is therefore preferred in industrial environments. For a data channel a pair of wires is required, one for the original and one for the inverted signal. Received and radiated EMI are therefore (theoretically) eliminated, as these signals are equal but opposite on the two wires and their fields will cancel each other. The maximal rate and distance of data transfer depends though on the attenuation characteristics of the cable and the noise coupling of the environment. A transmission rate of 12.5 Mbps over one meter long cable is possible.

Details of the hardware implementation are given in the chapter "Experimental set-up". There, Fig. 5.18 shows the implemented simplex network topology. For data and clock signals one receiver is connected with two transmitters over the same pair of wires. Only one transmitter is allowed to send at a time and the transmission is unidirectional. Termination resistances were placed at the extreme ends of all pair of wires in order to match the characteristic impedance of the wiring.

Two situations are of concern for proper signal transmission:

- Idle-bus periods
- Common-mode voltage problems

3.3.1. Idle-bus state

During the non-transition periods of the vehicle, the transmitters of data and clock signals are in a high-impedance state, so that the voltage on the respective pair of wires is left floating. Due to

the noisy environment, the corresponding receivers can be then falsely triggered and these signals are erroneously interpreted as valid signals. This situation should theoretically not occur, as the receivers are fail-safe. The input threshold value of their differential voltage is set between –10 mV and –200 mV and not between ±200 mV as usual. Like this, due to the termination resistances, their outputs should be logic-high during the bus-idle condition. Anyhow, the bandwidth of this hysteresis voltage still doesn't represent a reliable solution against high noise levels. This problem is completely solved at the application layer by means of the communication protocol. At this level, the bus is considered idle until the communication is acknowledged. During this time the SPI-units are deactivated, meaning that the clock signals are ignored and no bit-shifting actions take place inside their data shift registers. The transmitters for data and clock signals are enabled when the communication is acknowledged, so that the bus is no longer idle. The SPI- and McBSP-units are reset to initial configuration values and then activated. After a wait-period of one control cycle (Fig. 3.6) the McBSP-units will write their clocks and data on the bus.

3.3.2. Common-mode voltage and multicommutation problems

In systems where a large number of inverters are connected to a common DC-link, high-voltage transients can occur due to the multicommutation process of the IGBTs and the resulting stray inductance of the DC-link connection.

The switching times of the IGBTs in the different phases of the distributed inverters are not synchronized, never the less several IGBTs can switch simultaneously or nearly simultaneously. This is known as multicommutation [39]. The multicommutation effect on an inverter system as shown in Fig. 3.9 was analysed in [39], [40]. Here the voltage at the common stray inductance $L_{\sigma,common}$ is produced by the added di/dt values of the different commutating IGBTs.

Assuming the same di/dt for all IGBTs, the blocking voltage of an IGBT will be:

$$u_{CC,surge} = L_{\sigma,common} \cdot n \cdot \frac{di}{dt} + L_{\sigma,ph1} \cdot \frac{di}{dt} + U_D$$

(3.1)

The value of the surge voltage $u_{CC,surge}$ must be kept bellow the maximal rating of the switching devices. The first action to minimize this voltage is to keep $L_{\sigma,common}$ as low as possible. This is
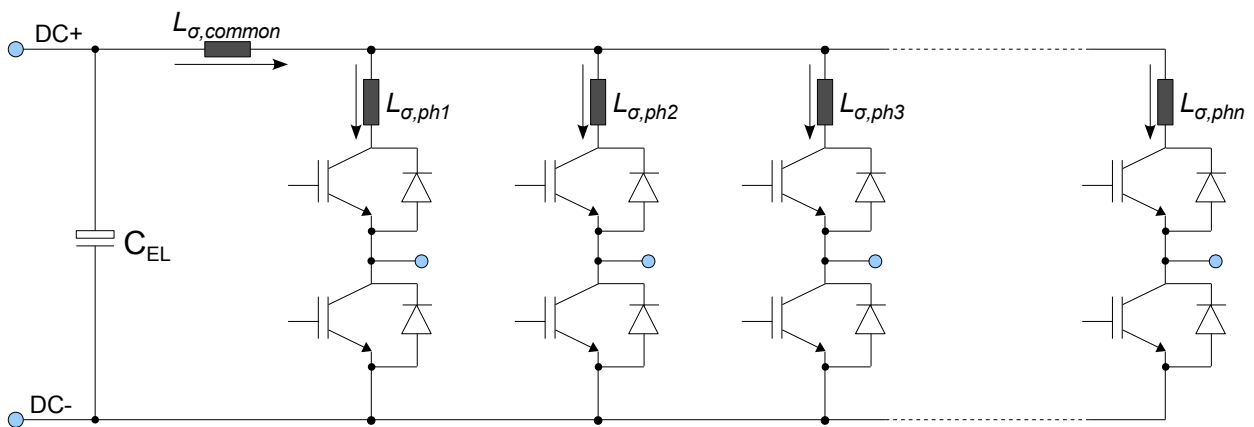

Figure 3.9 Surge voltages for multiple inverter legs connected to a common DC-link [40]

realized by implementing a compact bus system consisting of two copper sheets (DC+ and DC-), separated by an insulation layer [41]. Of course it would be preferable to be able to limit or control the value of di/dt, but the gate-drive circuit is not accessible in the commercial IPMs. Therefore, the modules must be protected against high surge voltages by snubbing elements (usually capacitors).

The simplified equivalent circuit of the proposed DC-link structure for this type of applications is shown in Fig. 3.10 and the parameters are defined in Table 3.3. The DC-voltage supply should be situated in the middle of the DC-link bus. A snubber capacitor is mounted very close to the DC-link terminals of each IPM and the electrolytic capacitors are also distributed along with the inverters, so that the current through the DC-link bus becomes more uniformly distributed [42].
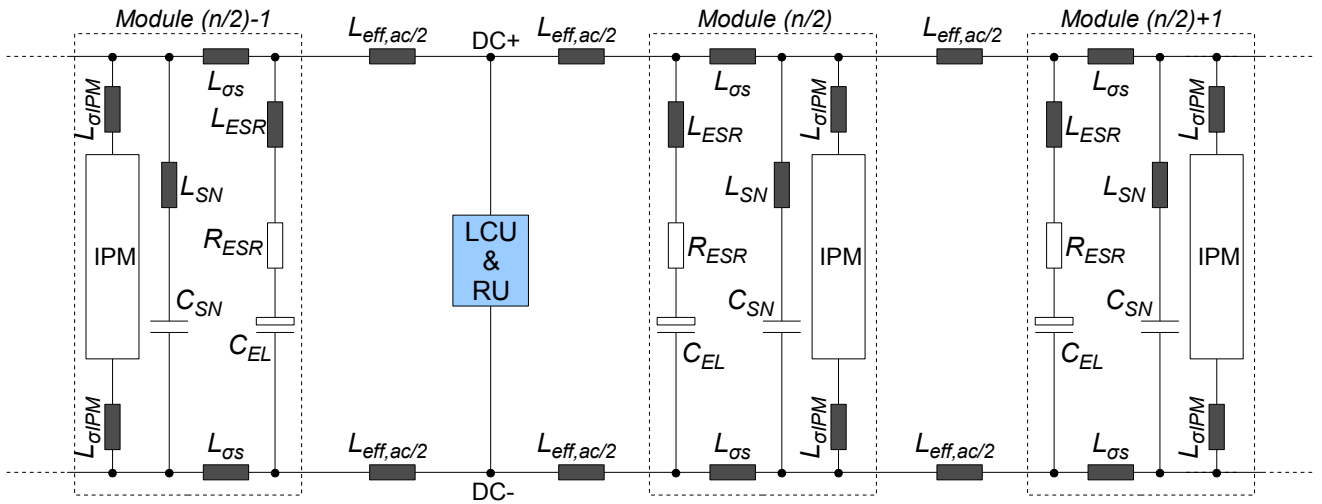

Figure 3.10 The circuit model of the common DC-link

Name	Definition
$L_{eff,ac}$	Total stray inductance of the bus bar system between two modules
$L_{\sigma s}$	Stray inductance of the PCB routes between the electrolytic and snubber capacitors
L_{ESR}	Equivalent series inductance of the electrolytic capacitors
R_{ESR}	Equivalent series resistance of the electrolytic capacitors
C_{EL}	Value of the electrolytic capacitors
L_{SN}	Equivalent series inductance of the snubber capacitors
C_{SN}	Value of the snubber capacitors
$L_{\sigma IPM}$	Stray inductance of the IPM

Table 3.3 Parameters of the circuit model of the common DC-link

Regarding the communication structure, the RS485 receivers have to be protected against voltage transients on the common negative DC-link line between two adjacent modules. These transient voltages are seen as common-mode voltages by the receivers and can have higher values than the maximal specified ratings of the devices.

The value of the common mode voltage u_{CM} (Fig. 3.11), seen by the RS485 receiver is:

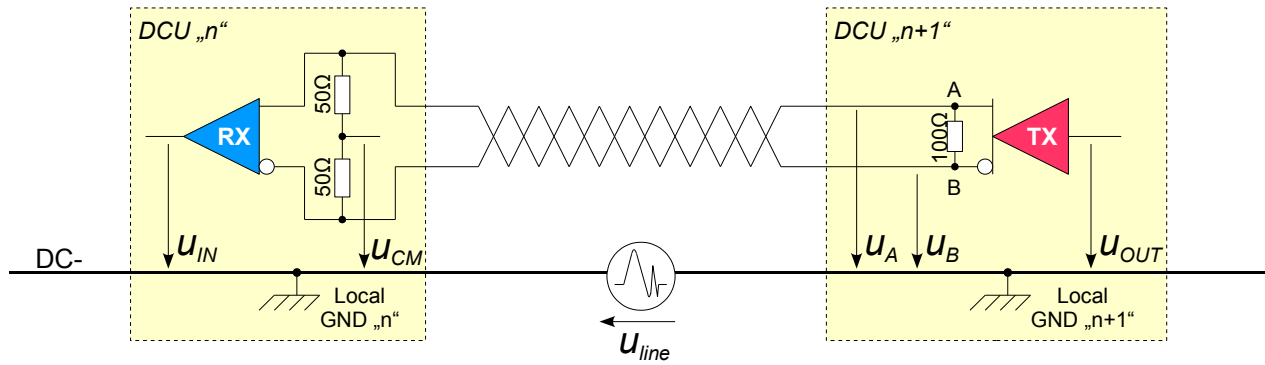$$u_{CM} = \frac{u_A + u_B}{2} + u_{line}$$

(3.2)

Figure 3.11 Common-mode voltage issue for the RS485 receivers

The characteristics of the transient voltage u_{line} were first analysed with the help of a SIMPLORER simulation model (Fig. 3.12), where both adjacent inverters were commutating simultaneously.
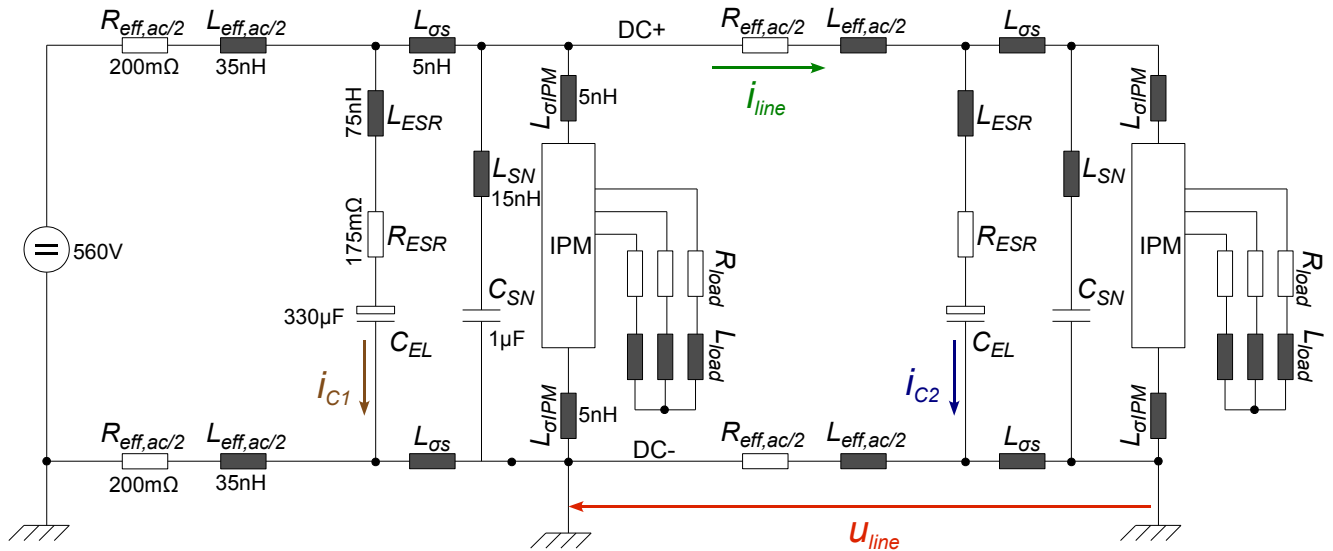

Figure 3.12 Simulation model for the analysis of the transient voltages on the negative DC-bar

A real IGBT model was used in the simulation and a dead-time interval was considered for the gate signals of an inverter-leg. Sinusoidal currents of different amplitudes and frequencies could be generated on the passive RL-load configuration.
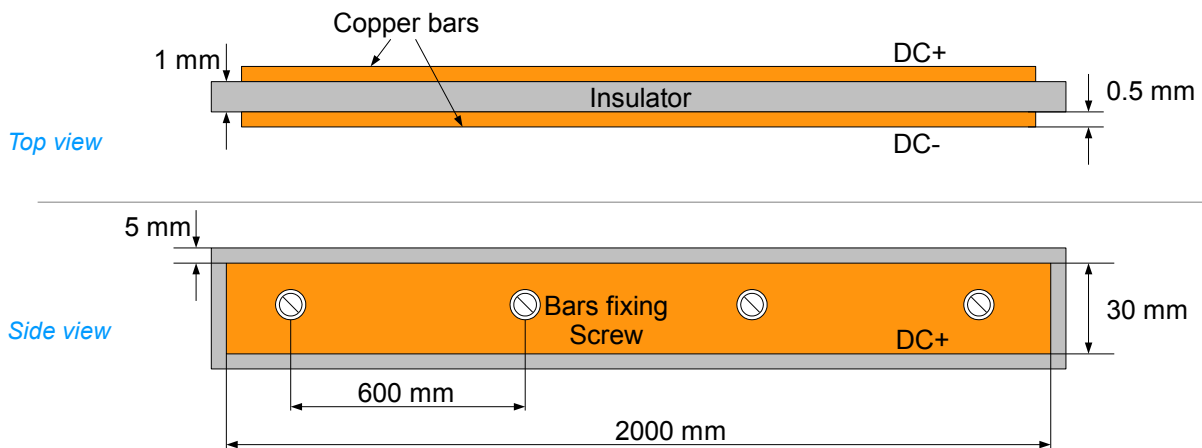

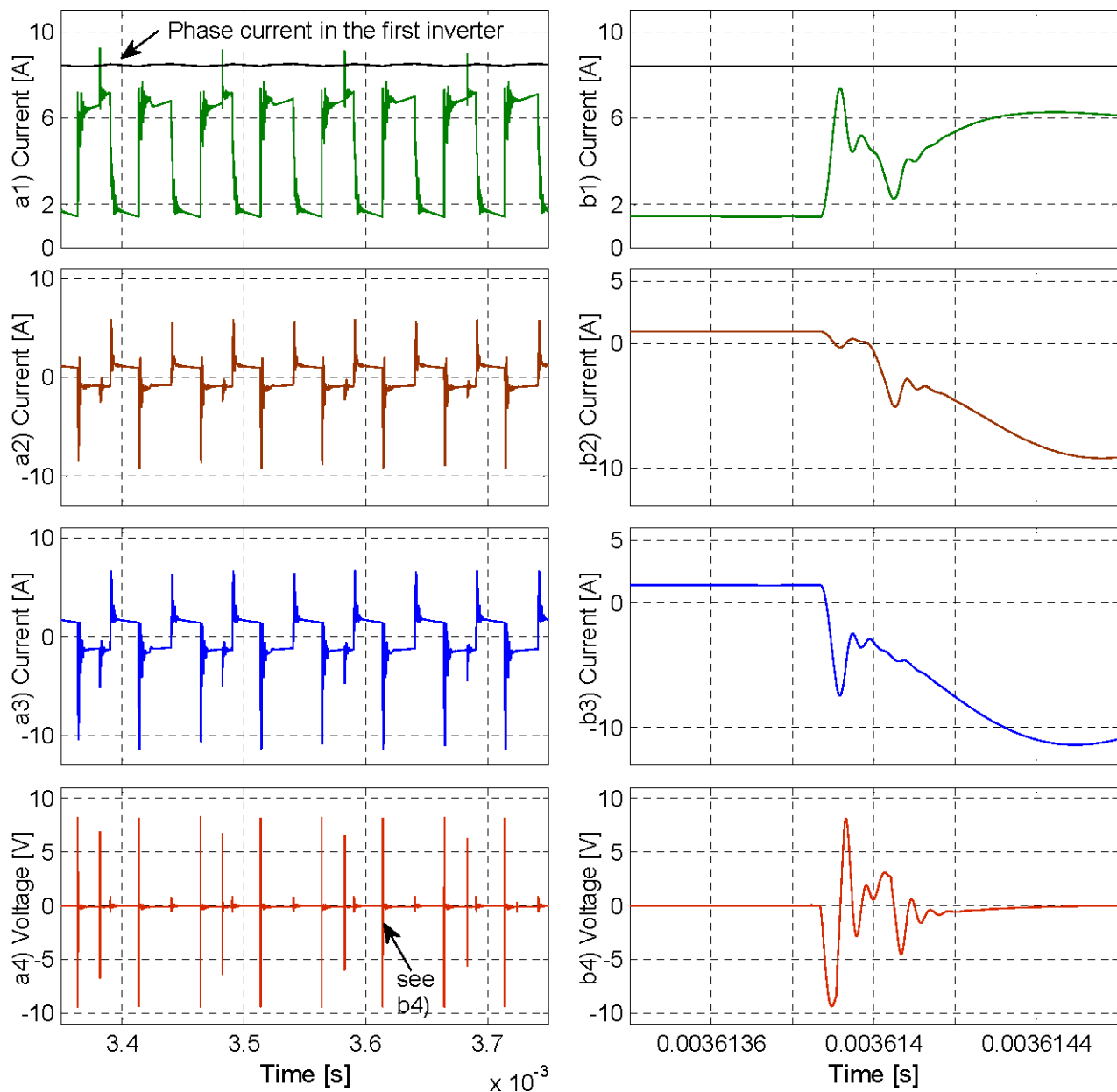Figure 3.13 Bi-plate bus system as common DC-link bus

Figure 3.14 Simulation results for the considered simulation model

a1) & b1) i_{line} : Current through the DC-link bars between the two inverters

a2) & b2) i_{C1} : Current through the electrolytic capacitor of the first inverter

a3) & b3) i_{C2} : Current through the electrolytic capacitor of the second inverter

a4) & b4) u_{line} : Transient voltage along the common negative DC-link between the inverters

The equivalent circuits of the electrolytic and the snubber capacitors were considered in the simulation. The values of their series resistances and inductances are calculated by means of their impedance values at the respective resonance frequencies. The impedance of the planar bus system consists of resistance and inductance. The inductance of each bus conductor is the sum of the self-inductance L_{bar} and the mutual inductance L_{mt}. The bus system is a bi-plate bus system, as shown in Fig. 3.13, where the currents in both bars have opposite directions. For a good inductive

coupling between the bars, the distance between them has to be small. The total inductance of the bus system is:

$$L_{eff,ac} = L_{bar1,ac} + L_{bar2,ac} - 2L_{mt,ac} \qquad (3.3)$$

The values $L_{bar1,ac}, L_{bar2,ac}$ represent the self-inductances at high frequency of the rails DC+ and DC- respectively. Typically, the frequencies of the transient voltages on these lines reach values up to several MHz. The skin- and proximity-effects play therefore an important role in determining the resistance and inductance values of the planar bars, as the inductance $L_{eff,ac}$ decreases at high frequencies [41].

The equations defining the effective inductance of the implemented bi-plate bus system (Fig. 3.13) at low and high frequencies as well as the resistance value at high frequency [41], [43], are presented in the appendix. The bus bar length between two adjacent servo-controllers is 0.6 m. Due to the connection elements of the servo-controllers to the bus bars, the value of $L_{eff,ac}$ for the mentioned length was approximated for the simulation at 70 nH.

The simulation results presented in Fig 3.14 show that the value of the transient voltage u_{line} is below the maximal allowed value of the common-mode bus input range, ±15 V, for most RS485 devices. The parameters of the DC-link components are shown in Fig. 3.12. The currents on the DC-link bus are shared between both DC-link capacitors. For the entire system these currents will be shared between the capacitors of both active and inactive inverters. The frequency of the transient voltage u_{line} is about 5 MHz.
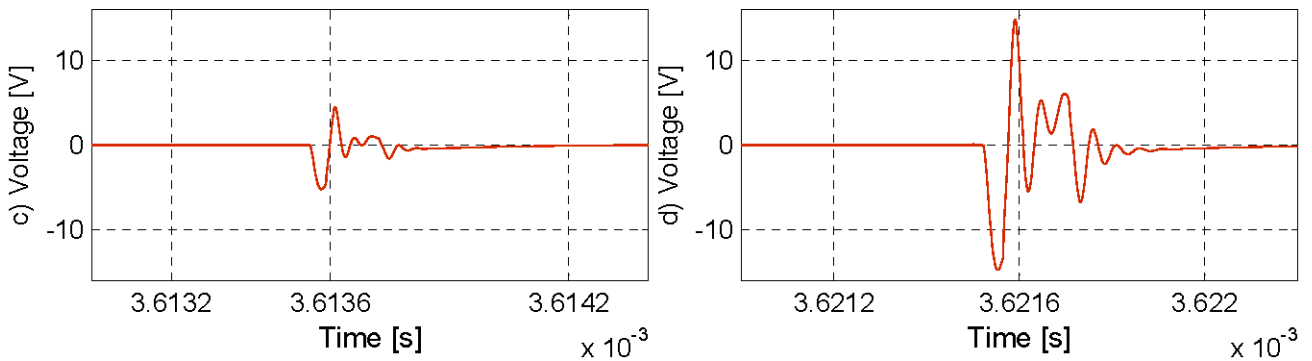

Figure 3.15 Effects of the DC-link parameters upon the transient voltage U_{line} (simulation)

    c) u_{line} : Transient voltage for $L_{eff,ac} / 2 = 10nH$ and $L_{SN} = 15nH$

    d) u_{line} : Transient voltage for $L_{eff,ac} / 2 = 35nH$ and $L_{SN} = 30nH$

General conclusions of the simulation results:

- The stray inductances $L_{\sigma S}, L_{\sigma IPM}$ have a very small influence upon the value of u_{line} but a big influence upon the surge voltages over the IGBTs.
- The inductances of the snubber capacitors and of the bus bars have the biggest influence upon the value of u_{line} (Fig. 3.15) and should be kept as small as possible.

- The values of the resistances of the DC-link components are not relevant for the amplitude of the voltage u_{line}. They only contribute to the damping time of the transient process.

The simulation results help to identify those circuit elements, which are most relevant for the generation, suppression and the characteristics of the voltage transients, but cannot substitute the measurement results. With the simulation model is not possible to consider disturbances, as parasitic capacitances and interference effects, which exist in a real set-up. Also an exact determination of the parameters of all circuit elements and the exact switching characteristics of the IPM cannot be obtained.
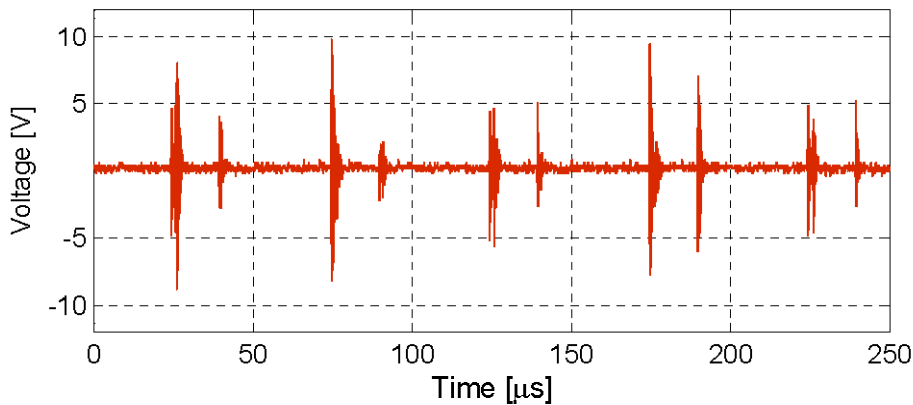

Figure 3.16 Experimental measurement of the transient voltage u_{line}

Anyhow, the experimental measurement from Fig. 3.16 shows similar results as in the simulation for the same control conditions. The damping time of the oscillations is larger but their amplitudes are not of concern. Using a tri-layer planar bus system would further reduce the effective impedance of the bus [41], so that lower transient voltages could be achieved.

In systems where the voltage transients are still of concern, additional protection measurements must be used. A first possible solution to protect the RS485 devices against high common-mode voltages, which luckily do not exist in the proposed application, is to isolate the ground of these devices from the host's device ground by using optical or digital isolators (Fig. 3.17). This method
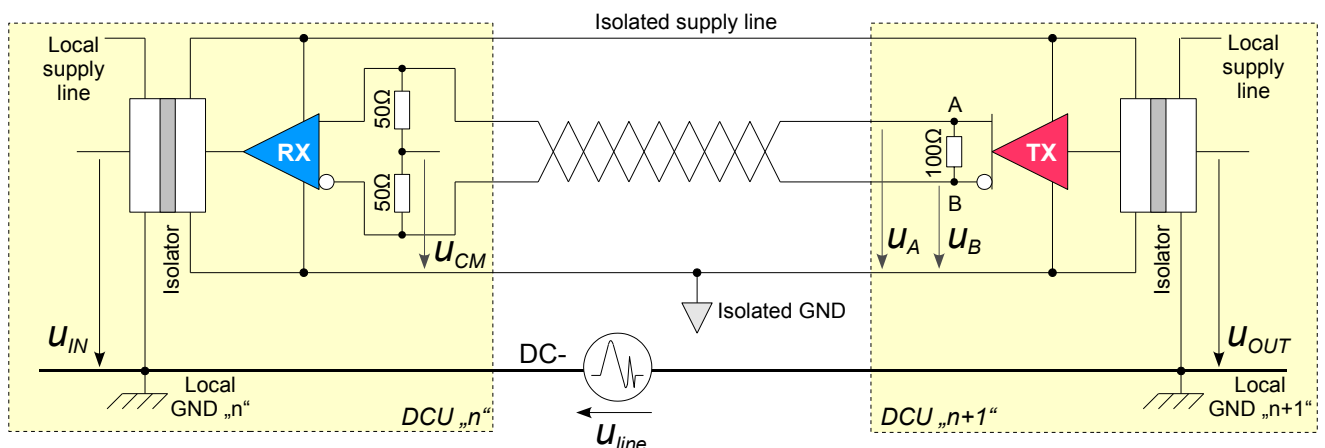

Figure 3.17 Galvanic isolation of the RS485 devices (not necessary in the proposed system)

requires, beside the isolators, also an isolated power supply between any two adjacent modules. As one of the aims of this work is to keep the implementation costs for large systems low, isolation should be avoided as far as possible.

Another, less-expensive solution is to use bi-directional transient voltage suppression (TVS) diodes. These are clamping devices, which suppress the overvoltages above their breakdown voltage and can withstand high power peaks (several hundreds of Watts). They are connected as shown in Fig. 3.18 and are selected to conduct at voltages in the proximity of the recommended operating conditions of the RS485 devices. The disadvantage in this case is that these diodes add an extra capacitance to the communication lines, which deteriorates the transmitted signals at high bit-rates.
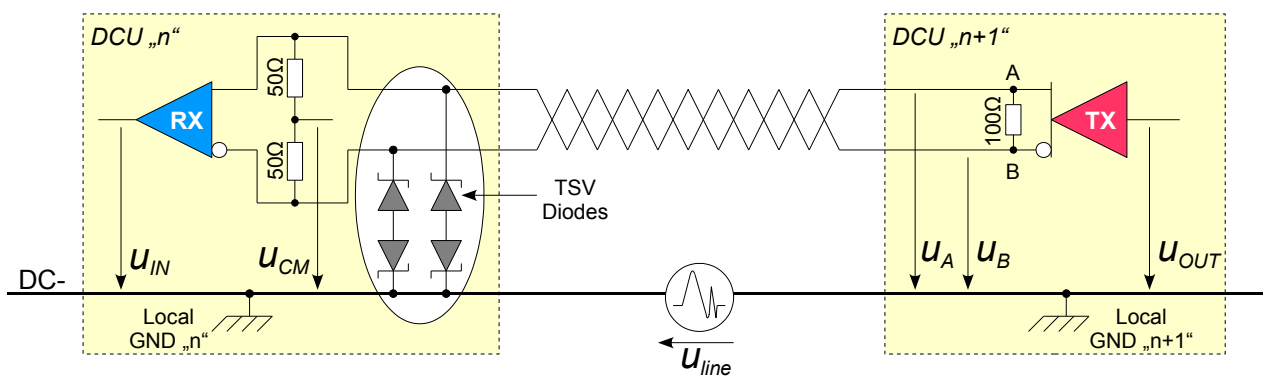

Figure 3.18 Transient voltage protection with TSV diodes

The receiver used in the experimental set-up (SN75LBC175A) has a built-in circuit protection against overvoltages, realised with standard Zener diodes, which have a very small capacitance, which doesn't affect the transmission speed. It can support short voltage transients in the range of ±30 V but with a maximum power peak of approximately 9 W. This is sufficient for the proposed application and is the most cost effective solution.

4. Industrial fieldbus solution for motion coordination and monitoring

To connect the CCU with all DCUs an industrial fieldbus is selected. During development, commissioning and test of a large system, control programs must be frequently modified and then downloaded to a multitude of DCUs. Also upload actions of process data, recorded within the DCUs, have to be possible. Up- and downloads are off-line file transfers initiated on demand. While the system of linear drives is in normal operation, data for motion coordination and monitoring have to be exchanged cyclically between CCU and the DCUs inside few milliseconds.

4.1. Overview of the main real time Ethernet (RTE)-based fieldbuses

The actual trend in distributed automation systems is to use Ethernet as the single networking technology, as shown in Fig. 2.12. The main characteristics of Ethernet, which lead to this trend, are [44], [45]:

- The high data transmission rates at the physical layer, which assure a large bandwidth compared with other fieldbuses
- At the network and the transport layer of the OSI model, the IP and the TCP/UDP protocols allow an easy integration in the Internet and the use of application layer protocols such as FTP (up- and download of general data to the field devices) or HTTP (web servers for device engineering).
- The implementation costs are low as the technology is wide spread and well specified

Because Ethernet alone is not real-time capable due to its nondeterministic arbitration mechanism, several techniques (e.g. modified CSMA, token passing, TDMA, master-slave approach and switched Ethernet), meant to transform Ethernet in a true real-time communication tool, have been developed over the years [33], [46], [47]. The RTE protocols can be allocated to one of the three possible architectures shown in Fig. 4.1. The first architecture uses Ethernet and the TCP/IP protocols without any modification. Only at the application layer a specific protocol is defined. The second architecture uses the standard Ethernet hardware but bypasses the TCP/IP stack, so that a specific protocol type is specified in the Ethernet frame. The third architecture also bypasses the TCP/IP stack but brings also modifications in the hardware of the Ethernet. The scheduling process of switched Ethernet is modified and the switching functionality is integrated in the field devices. These types of protocols achieve the highest performance (e.g. have data

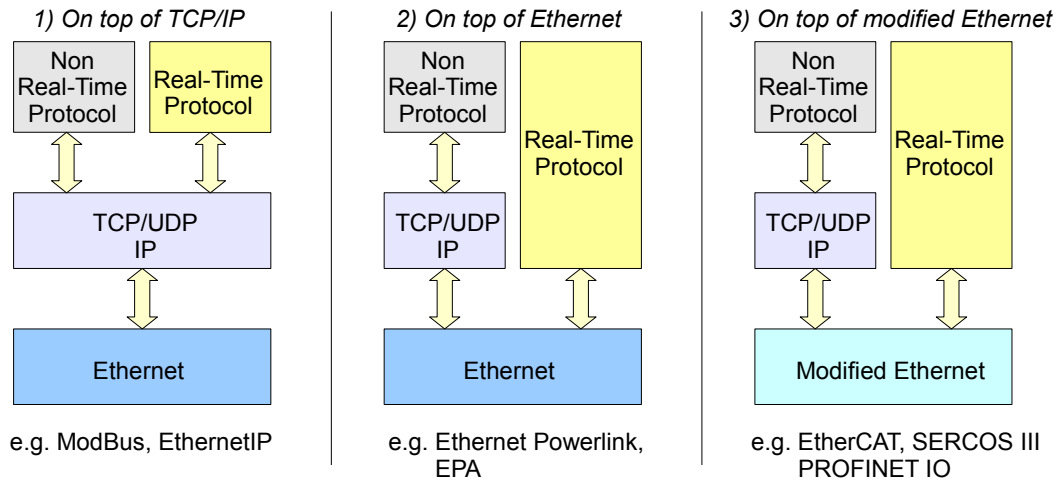| 1) On top of TCP/IP	2) On top of Ethernet	3) On top of modified Ethernet

Figure 4.1 RTE architectures [46]

update cycles smaller than one millisecond) and are therefore preferred in distributed servo-drive applications. The protocols belonging to the second and third architecture are also able to handle standard IP frames, either on the same channel as the real-time data (tunnelling) or on a separate channel.

There are many RTE protocols, which can fulfil the task of motion coordination and monitoring for this application, regarding the necessary data update cycle of few milliseconds. Many of them have been created for specific applications and just few were widely adopted and internationally standardized, like e.g. Ethernet Powerlink, EthernetIP, PROFINET, EtherCAT and SERCOS III.

Fieldbus characteristics	EtherCAT	SERCOS III	PROFINET IRT
Principle of operation	Master/Slave	Master/Slave	Time synchronization of the device internal switches
Special Ethernet controller	Required only for the slave devices	Required for both master and slave devices	Required
Basic network topology	Line, ring, star or tree structures are supported	Line or ring	Line or ring
Cable redundancy	Yes	Yes	Yes
Overall Performance [48]	Very good	Very good	Good
User organization	ETG (EtherCAT Technology Group)	SI (SERCOS International)	PNO (PROFIBUS Nutzerorganisation)
Number of suppliers, products variety and organization members	Big	Medium	Medium

Table 4.1 Overview of the main characteristics for three RTE-based fieldbuses

The utilization of an RTE-based fieldbus for motion coordination and monitoring in this case means that the DCUs must incorporate a hardware interface for this fieldbus. An ASIC, an FPGA, a multi-protocol Ethernet controller or a standard Ethernet controller can represent this hardware interface. Due to the high number of DCUs in our application, the hardware costs and complexity is one of the main criteria in selecting the fieldbus.

The costs for the special Ethernet controllers are quite similar for the three protocols of Table 4.1, because the respective protocol stack can be implemented in an e.g. FPGA. EtherCAT has the advantage that its master device requires only a standard and no special Ethernet controller. EtherCAT offers also the most flexible network topology and has the largest variety of products, number of suppliers and organization members [35]. For smaller, non-scalable system topologies (small number of vehicles) where the communication between the adjacent DCUs would have been possible over an RTE-based fieldbus alone (no extra SPI-based fieldbus required), then SERCOS III would have been the better solution due to its superior performance regarding the cross-communication procedure between the slave devices [34].

4.2. Data transfer modes over EtherCAT

EtherCAT is a master/slave-based protocol where the master always initiates the data transmission inside a communication cycle. The master can use the same Ethernet frame to send data to, or gather data from the slave devices. Inside the slave devices the incoming frames are hardware processed "on the fly", meaning that data is added to or extracted from the frame while this passes through the device. The delay-time due to data processing of a slave is very short (below 100 ns) and constant, as it doesn't depend on the size of the frame. When the formed frame reaches the last slave of the network, it is automatically sent back to the master. The slave devices of an EtherCAT network are designated to one or more network segments. A segment consists of one or several slaves. From the standard Ethernet point of view an EtherCAT segment is a single Ethernet device. There are two configuration modes of an EtherCAT network:

- Direct mode, where a network segment is designated to a master device
- Open mode, where several network segments are accessed separately over a switch by one or several masters

The slave devices of a network segment can be arranged in a line, ring, tree or star configuration. All configurations can be seen as a physical ring due to the full-duplex data transmission and to the fact that the slave devices can transfer data also in the reverse direction [49].

The Ethernet frames used by EtherCAT are identified with the number 0x88A4 in the header of the frame. The data in the frame is split in specific EtherCAT datagrams as shown in Fig. 4.2. Any datagram can be designated to a particular slave but an important feature of EtherCAT is that many slaves can be handled by a single datagram using a logical addressing scheme. The logical address space of 4GB is shared among all slave devices of a network segment. Logical addresses are converted inside a slave device into local physical addresses by means of the Fieldbus Memory
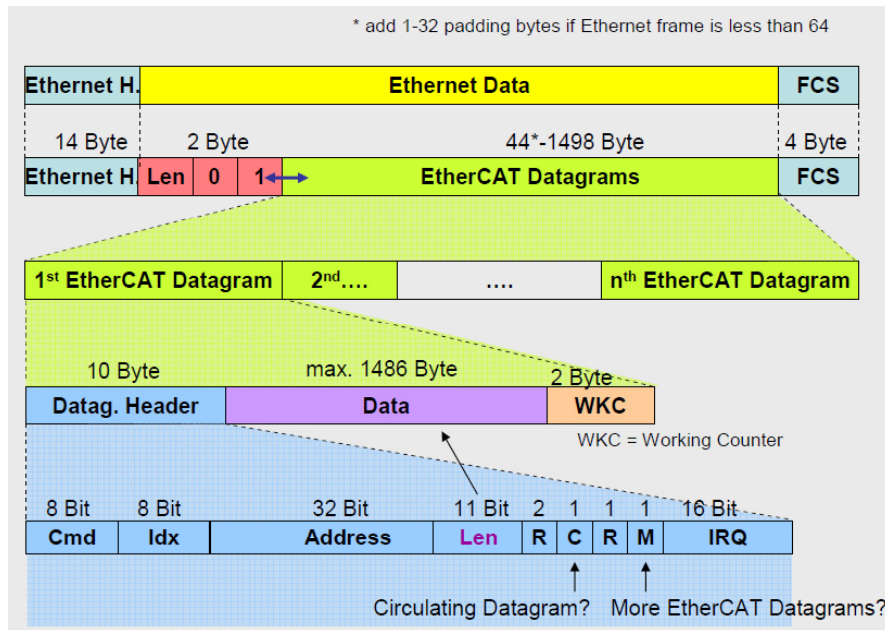
Figure 4.2 Structure of the Ethernet frame used by EtherCAT [49]

Management Units (FMMUs). The FMMUs allow therefore the logical addressing for data segments that span over several slave devices. This reduces the total overhead.

Until now it was shown how can the master access the memory of the slave devices. This memory is also accessed by the DSPs of the DCUs. Hardware details are shown in the Fig. 5.19 of the chapter "Experimental set-up". A memory access management is therefore necessary. This is realized by the SyncManager units of the slave devices, which are using memory buffers of predefined lengths to assure a consistent and secure data exchange between the EtherCAT master and the DCUs. There are two communication types in an EtherCAT network:

- Reliable communication (mailbox data transfer), where the master and the DCU accessing the memory of the ESC must agree upon the write/read access (data cannot be written/read at/from one address by one unit until it was before read/written by the other unit).
- Non-reliable communication, where both the master and the DCU can access the memory of the ESC at any time for both read and write actions.

The reliable communication is based on a specific protocol at the application layer, which must be also implemented in the DCUs. Here the FoE (File access over EtherCAT) protocol was used for both update and parameterisation (download) of the control algorithm as well as for general data upload. This protocol is similar to the well-known FTP protocol. The general data, representing state variables of the control algorithm, were saved in every control cycle in the memory of the DCUs. The master then uploaded them off-line, where they were analysed with MATLAB to prove the quality of the control. For this communication the master used physical addressing and exchanged data only with one DCU at a time.

The non-reliable communication is used for cyclical exchange of process data. The term non-reliable is associated with the fact that old data will be dropped if the above-mentioned memory

buffers are written faster than being read. This communication serves for motion coordination and monitoring. Based on an internal traffic planner, the master generates cyclically the new position reference values for the vehicles. These values are embedded in an Ethernet frame as shown in Fig. 4.3.

As this frame passes through, the DCU will notice that its logical address (predefined in its FMMU) is inside the logical memory area specified in the header of the first datagram (logical start address and length) and extracts the appropriate position reference value from it. Similarly occurs with the second datagram, when the DCUs insert their status values in the frame. After being processed by all DCUs, the frame returns to the master for evaluation. The master checks first the valid processing of a datagram by comparing the WKC (Working Counter) with the expected value. This counter is incremented by the DCUs after a successful write or read action. The frame ends always with the FCS (Frame Check Sequence). This is recalculated inside each DCU and if an error is detected, the master will be flagged by this DCU. A fault is like this precisely located in the system [49].
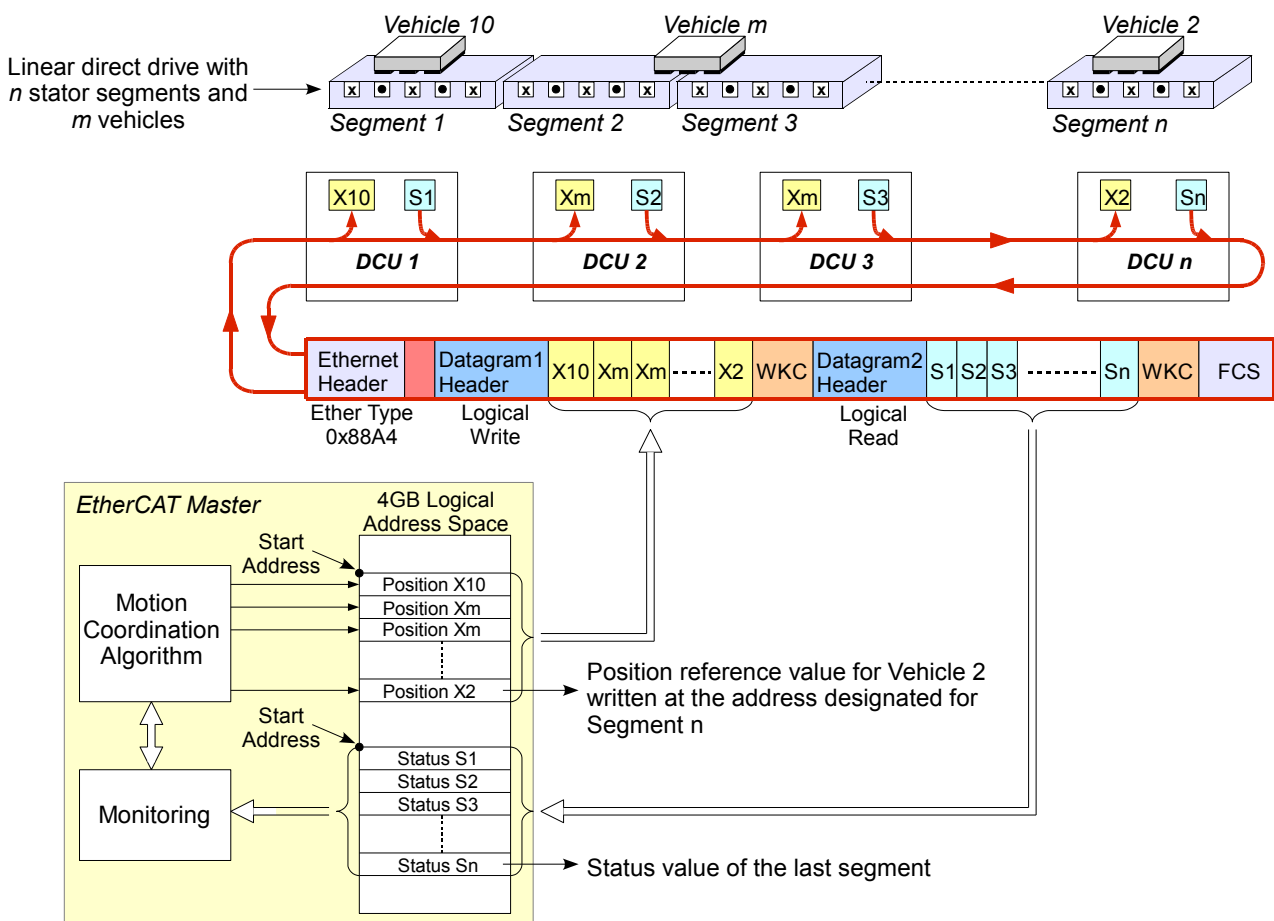

Figure 4.3 Cyclical data transfer for motion coordination and monitoring

4.3. The EtherCAT master application

The Windows Control and Automation Technology (TwinCAT) is a software application running under Windows NT, which implements the functionality of the EtherCAT master [50]. It gives the user the possibility to define special tasks, which have different priority levels and are executed cyclically at specified time intervals. The lowest cycle time is 50 μs. The user cannot write control code or any code lines inside those tasks but can only define variables. In each communication cycle the defined input-type and/or output-type variables of a task can be exchanged with the process data of any EtherCAT slave device. An input variable of a task can be also associated with an output variable of the same task, so that process data communication between two EtherCAT slaves is possible. For the experimental set-up an output variable of a task, representing the
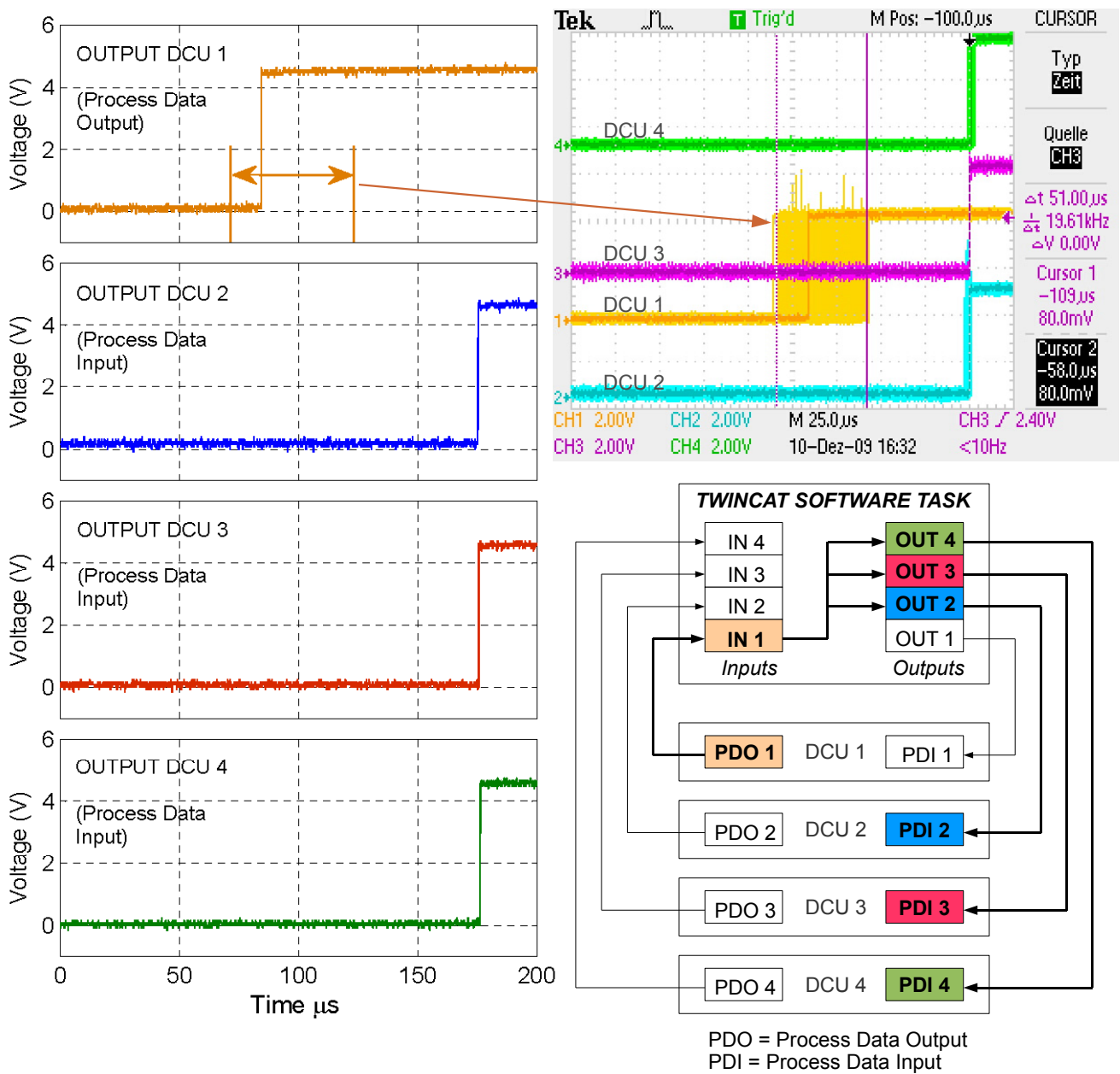

Figure 4.4 Analysis of TwinCAT's real-time functionality

position reference value of the vehicle, was associated with the input process data of all EtherCAT slaves. Output process data, representing the status of the distributed servo-controllers, were in turn associated with four input variables of the same task. Access to the variables of a task can be gained from Windows applications like Visual Basic or Visual C++ via a specific DLL. Here a Visual Basic application was created, which generates the new position reference values for the vehicle and monitors the system at 10 ms intervals.

The real-time capability of TwinCAT was analysed as shown in Fig. 4.4. A program in the first DCU toggled cyclically the value of an output process data and output this action on a GPIO. The program in the other three DCUs read continuously (pooling) the memory of the local ESC and output a physical signal according with the value of one input process data. The output process data of the first DCU was connected with an input variable of a software task running at 50 µs. The input process data of the other three DCUs were connected with three output variables of the same software task. The software task was therefore responsible for the real-time data transfer between the DCUs. The minimal data transfer delay is about 56 µs (one cycle) and the maximal delay is 106 µs (two cycles). This is due to the fact that the cyclical writing of the process output data of the first DCU is not synchronized with the Ethernet frames sent by the software task. The 6 µs difference represents the latency of the system.

The communication relationship at a certain moment between the master application and the DCUs is defined by means of the EtherCAT state-machine, shown in Fig. 4.5. The master requests a state transition through a special register of the ESC. The transition requires specific initialisations of the units (e.g. FMMUs and SyncManager) and the memory registers of the ESC from both DSP and master side. The EtherCAT state-machine must be therefore implemented in the DSP-Flash memory.
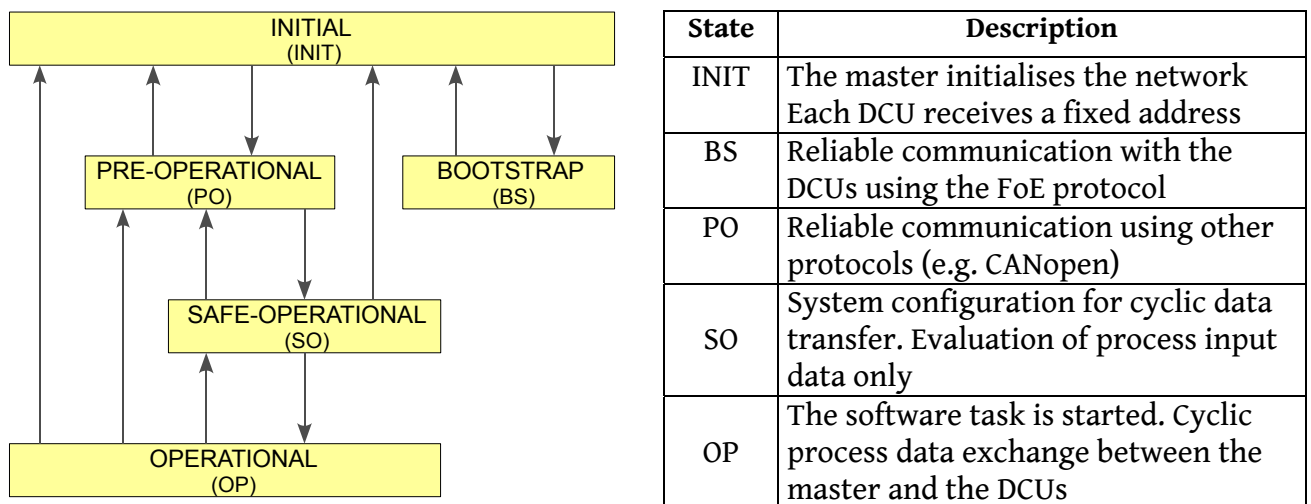
State	Description
INIT	The master initialises the network Each DCU receives a fixed address
BS	Reliable communication with the DCUs using the FoE protocol
PO	Reliable communication using other protocols (e.g. CANopen)
SO	System configuration for cyclic data transfer. Evaluation of process input data only
OP	The software task is started. Cyclic process data exchange between the master and the DCUs

Figure 4.5 Description of the EtherCAT state-machine

4.4. Software configuration for the embedded servo-controllers

The DCUs must work as embedded systems, where the entire firmware is saved in the internal Flash memory of the DSPs [51]. Initially, in order to write the code sections in the DSP-Flash, the JTAG interface of the DSP-board is used. This implies a non-isolated connection between the CCU and the DCUs. The DSP-Flash has two partitions. The first partition contains code sections, which are not subject to changes and the second contains modifiable code sections (Table 4.2).

Fix Code Sections	Changable Code Sections
1). Initialisation of system control registers and of the Flash unit	1). Initialisation of variables used for the control algorithm
2). Initialisation of the used peripheral units (ADC, EVA, SPI, McBSP, XINTF)	2). The motor control algorithm (the field oriented control)
3). Transfer of functions from Flash to RAM. Running code from Flash reduces the processing speed at 80%	3). Functions defining the serial point-to-point communication
4). Functions to Erase, Program, Verify the Flash	
5). The EtherCAT state-machine	
6). The FoE protocol	

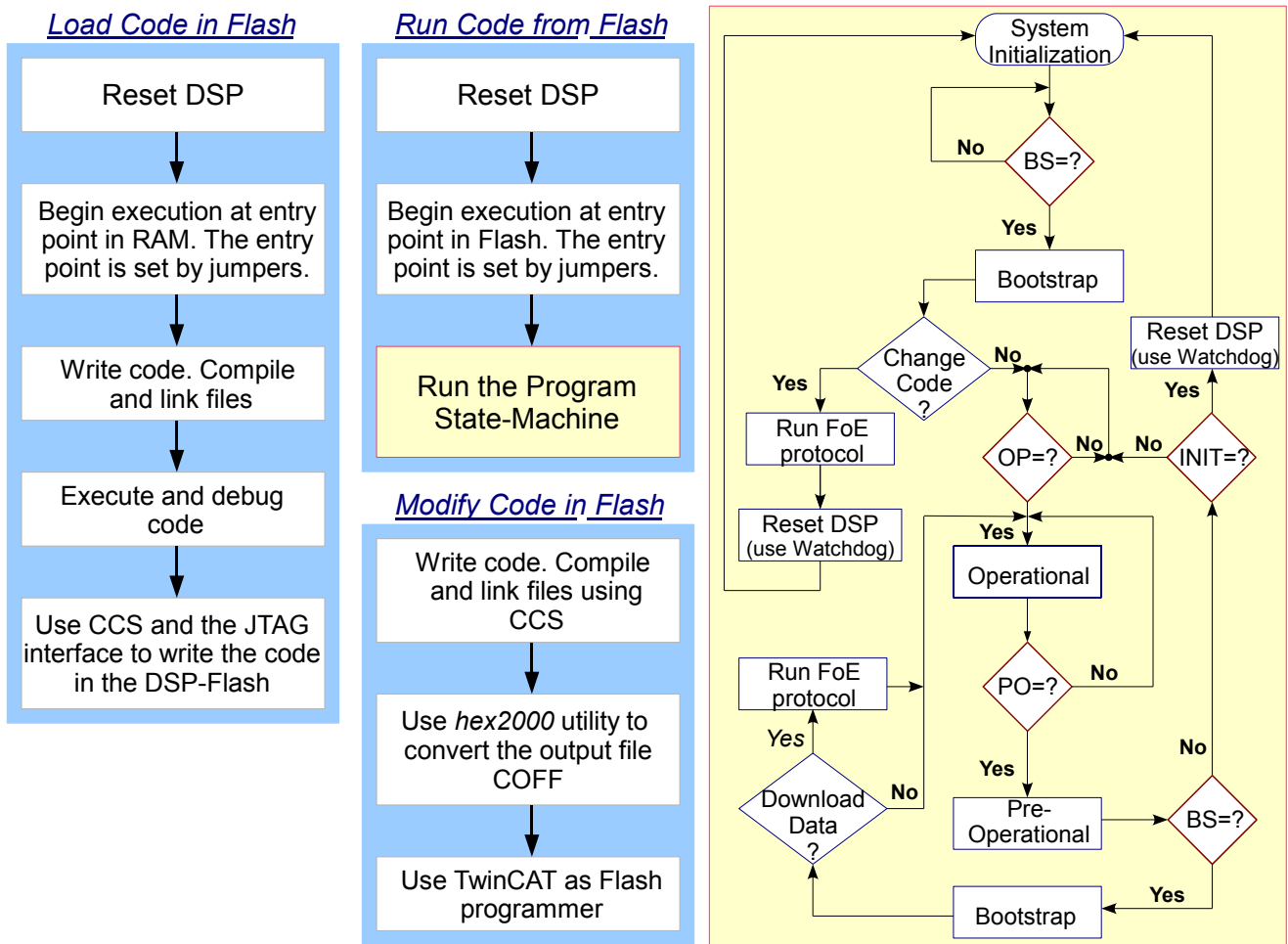Tabelle 4.2 Main code sections of an embedded servo-controller

Figure 4.6 The state-machine of the embedded servo-controllers

Once the EtherCAT state-machine and the FoE protocol have been downloaded in the DSP-Flash, it is possible to update the changeable code sections or to download general data by using TwinCAT as Flash-programmer or Flash-reader respectively. The down- and uploading process over the physical layer of Ethernet has the advantage that the communication partners are electrically isolated.

In order to update some code sections of a DCU, the program is written and compiled with the integrated development environment CCS (Code Composer Studio), installed on the CCU. From the generated COFF (Common Object File Format) output file, the modified code sections are extracted and saved in ASCII format with the help of the *hex2000* conversion utility [52]. They are further passed to TwinCAT, which will address the desired DCU by its physical address and will initiate the reliable communication with it over the FoE protocol. After the data transfer is finished, the DSP is reset with the help the Watchdog and the new code can be used without having to power-down the controller.

Fig. 4.6 shows the main operations performed on the DSP-Flash and the state-machine for a servo-controller. This is based on the EtherCAT states of the DCU. The interrupt routine for the control algorithm is started always in the operational state. From the Bootstrap state is possible to update the code sections, which requires a reset at the end, or simply to download general data for analysis without resetting the device.

5. Experimental set-up

In Fig. 1.3 the general configuration of a linear drive system was shown. This chapter presents the implementation of all units of the drive system, but focuses more on the Information Processing Unit (IPU) and the Power Processing Unit (PPU). The developed system architecture was tested in a small-scale experimental set-up, consisting of four identical stator segments and one vehicle. Each segment has a dedicated servo-controller. The block diagram representation of the experimental set-up is shown in Fig. 5.1 and the photo of the set-up is shown in Fig. 5.2.

Figure 5.1 Block diagram of the experimental set-up

5.1. The Linear Motor Unit

Four stator segments of type LSE10G from *Baumüller* are building the track in a single-cam arrangement (Fig. 5.3). The stator windings are distributed in the slots of a laminated iron core as shown in Fig. 2.1. The skewed PM is bounded on the surface of a massive back iron (Fig. 5.4). The mechanical construction of the vehicle–guideway system is shown in Fig. 5.5.
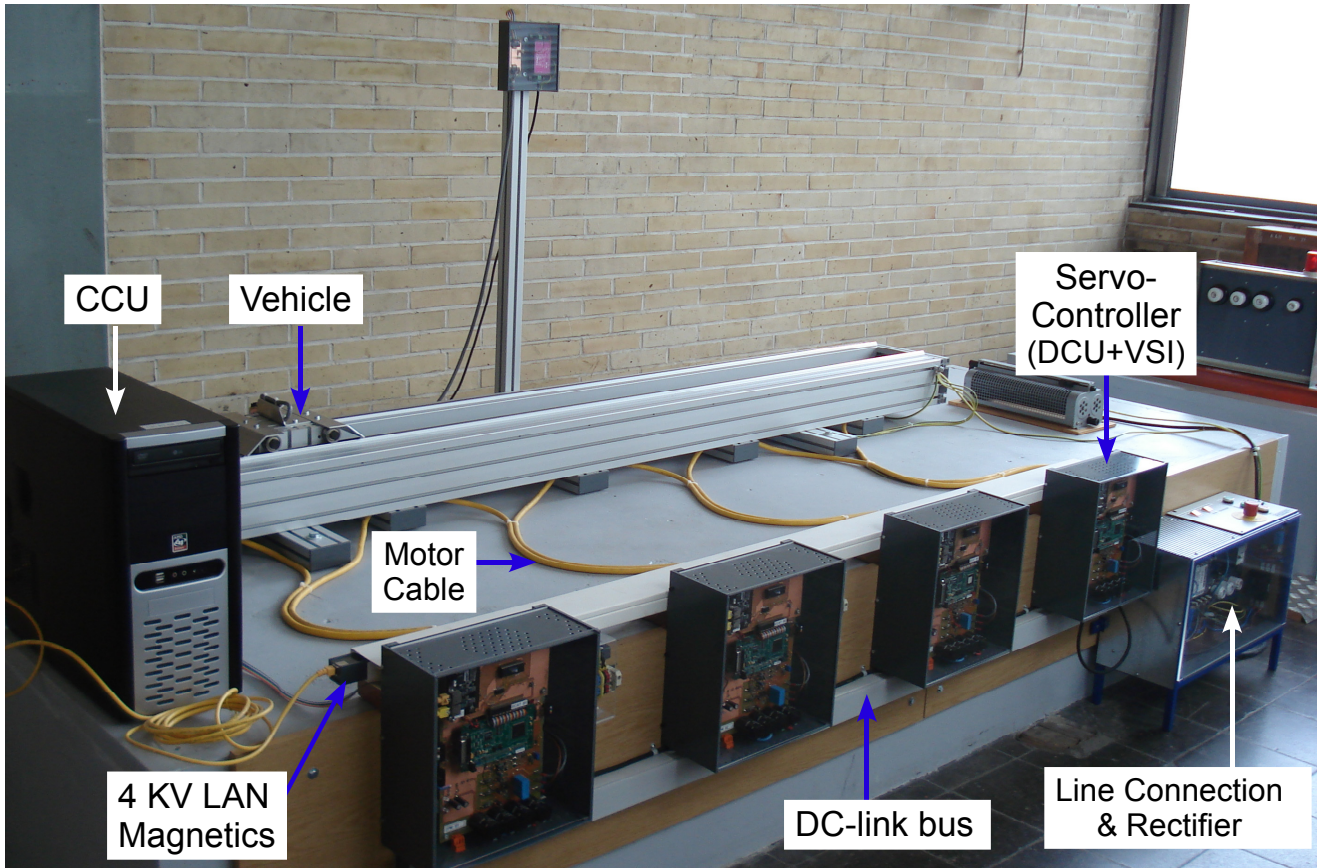
Figure 5.2 Photo of the experimental set-up

Figure 5.3 The linear track

The vehicle maintains a fix vertical position along the guideway due to the four-wheel system on the guide rail, so that there is a constant air gap of 1 mm between the PM and the stator segments.

The pole pitch of the motor is 36 mm. The PM has 4 poles and a stator has 14 poles. Due to the even number of poles of a stator and the alignment of its windings, there
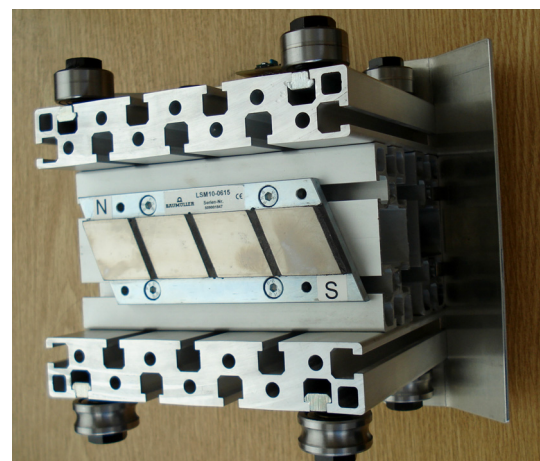

Figure 5.4 The vehicle

is no phase-shift of the electrical angle between two adjacent stators.

An odd number of stator poles would have assumed a phase-shift of 180°. The flux linkage of a phase winding at the end of a stator will continue in the same phase of the following stator. Even
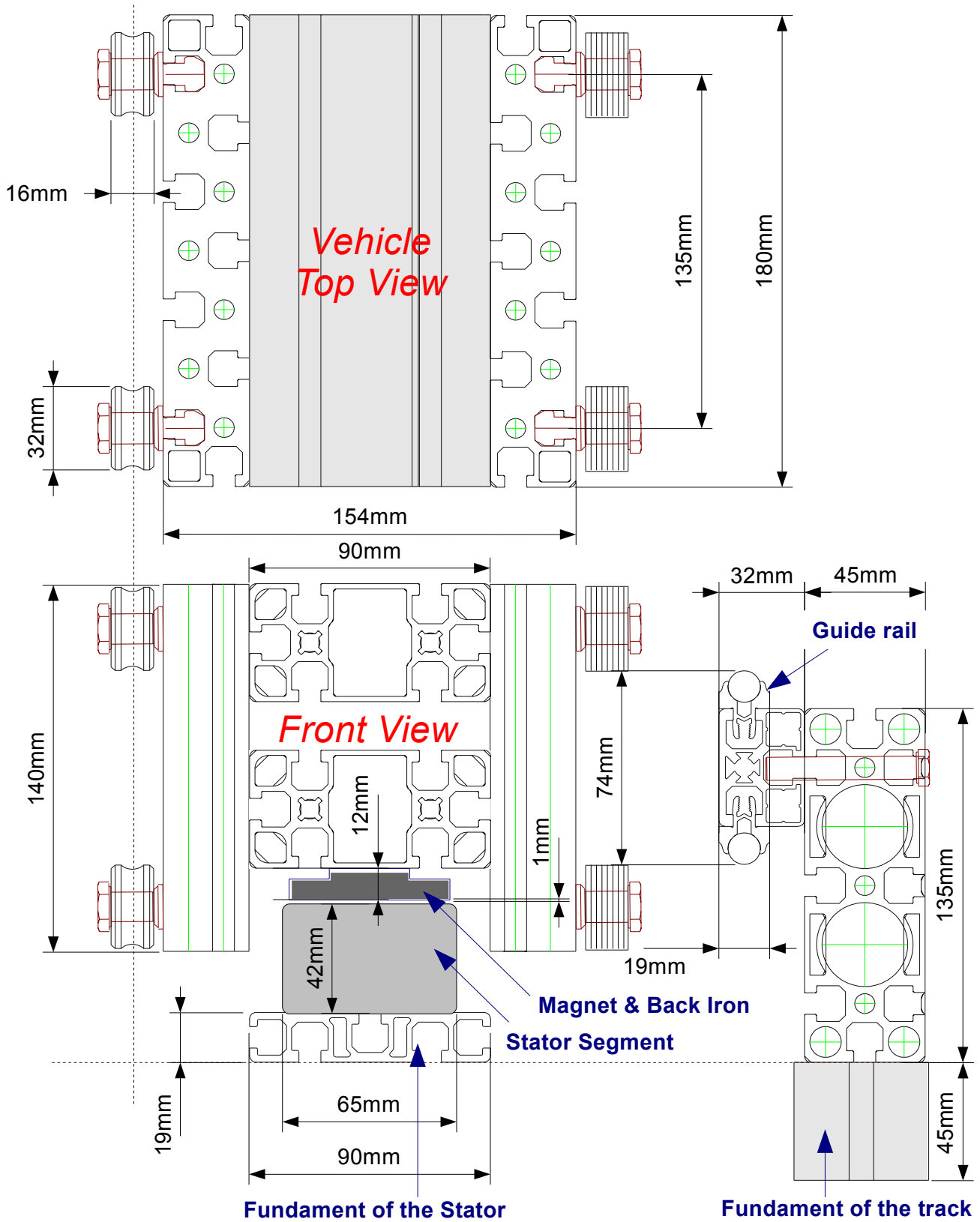
Figure 5.5 Mechanical construction of the vehicle and of the guideway

though there is no gap between the stators, there is a gap between the end-windings of two adjacent stators due the thickness of the stator enclosure. In this area the value of the reluctance will increase, leading to a decrease of the magnetomotive force for the same flux density.

Since the PM covers only 28.5% of the stator's surface, it is expected to have a low induced EMF-value. The force parameters in Table 5.1 are specified for the case when the length of the PM equals the stator length.

Maximal thrust force	$F_{th,\max}$ = 1270 N
Nominal thrust force	$F_{th,nom}$ = 210 N
Maximal current	$I_{\max}$ = 13.9 A
Nominal current	I_{nom} = 1.9 A
Force constant	k_F = 110 N/A
Phase resistance	R_S = 2.4 Ω
Phase inductance	L_S = 10.5 mH
Pole pitch length	τ = 36 mm
Stator segment length	l_m = 504 mm
PM length	l_p = 144 mm
Maximal speed	$v_{\max}$ = 4.5 m/s
Nominal speed	v_{nom} = 2 m/s
Mover's weight	M_v = 6.5 Kg
DC-link voltage	U_D = 560 V
Cooling type	Natural cooling

Table 5.1 Parameters of the linear motor

5.2. The Power Processing Unit

The PPU contains the following functional blocks:
- Line Connection Unit (LCU)
- Rectifier Unit (RU)
- Voltage Source Inverter (VSI)

5.2.1. The Line Connection Unit

The LCU contains the main switch, a line circuit breaker, line-fuses and an EMC-filter, as shown in Fig. 5.6. Over the main switch the electronic of the servo-controllers is supplied first. The line circuit breaker is closed only after a safe power-up of the electronic. Variable frequency drives are a source of electromagnetic interference. This electrical noise is generated by the fast switching voltages at the motor and supply cables, which have coupling capacitances to earth. An EMC-filter is therefore necessary to assure that this high-frequency electrical noise, in the range of a few kHz up to tens of MHz, doesn't affect the mains. At the same time it assures that electrical noise in the mains, generated by other equipments, doesn't affect the drive system. The used EMC-filter is rated at 25 A.

5.2.2. The Rectifier Unit

The RU contains a standard 3-phase diode bridge rectifier rated at 1200 V/25 A, a brake chopper and a pre-charge resistance connected over a circuit breaker between the EMC-filter and the

diode bridge (Fig. 5.6). The commutation notches of the diode bridge will insert current harmonics in the mains. This will affect the ideal sine-wave voltage characteristic at the input of the rectifier. In industrial plants where many drives are connected to the mains, the generated total harmonic distortion is of concern and have to be diminished by inserting line chokes at the LCU level.

5.2.3. The Voltage Source Inverter

The VSI builds the modular servo-controller together with the DCU (Fig. 5.1). There was no commercial solution to completely suit the requirements of this application, so that the modular servo-controller was designed and implemented in the laboratories of the institute.

The VSI contains the following components:

- 6 IGBTs and the associated free-wheeling diodes
- Gate driver circuit
- Current measurement and overcurrent protection circuit
- DC-link capacitors
- DCU-interface circuit
- Electronic power supply circuit

The power range of the inverters for this type of application lies between 1 KW and 10 KW. For a DC-link voltage of 560 V, the rated currents of the inverters are in the range of 10 A up to 70 A.
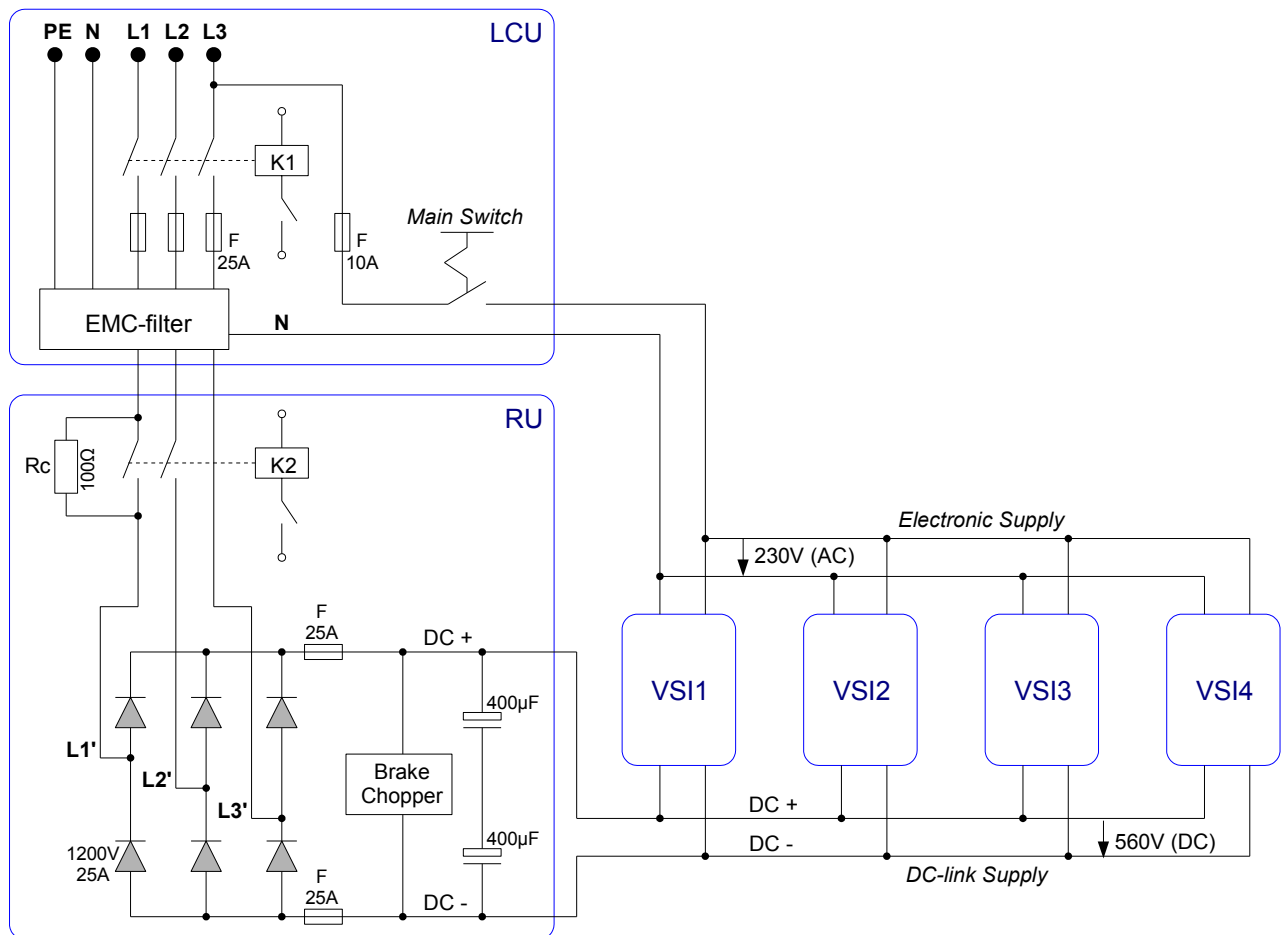

Figure 5.6 Configuration of the PPU

Intelligent power modules (IPMs) represent a cost effective and highly integrated solution for the power stage of highly scalable drive applications [53]. The IPMs use the transfer molding technology for insulation and housing and were designed initially for home appliances (600 V-IGBTs). About five years back, transfer molded IPMs in dual in-line packages (DIP) with 1200 V-IGBTs and currents up to 35 A became available for general industrial application use.
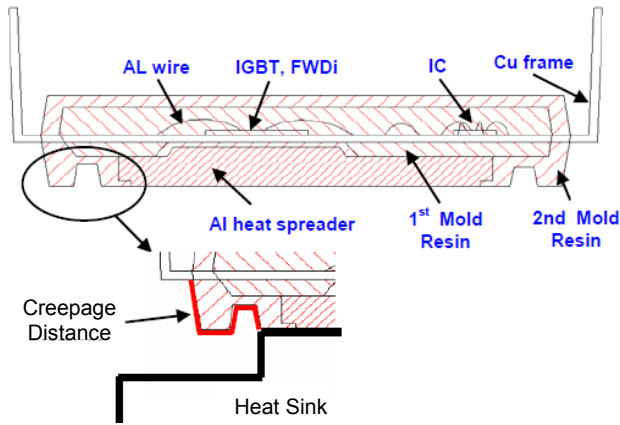

Figure 5.7 1200V DIP-IPM [54]

Here the 1200 V/25 A DIP-IPM, PS22056, from *Mitsubishi* was used. This device contains within the same package the power devices and control ICs for gate drive and protection [54]. The molded structure is shown in Fig. 5.7. The internal circuit and the pin-configuration are shown in Fig. 5.8.

Each IGBT from the high side is controlled by the HVIC (High Voltage Integrated Circuit). This integrates high voltage level shifters, which make a direct, non-isolated, connection to the DCU possible. The IGBTs from the low side are controlled by the LVIC (Low Voltage Integrated Circuit). If the HVIC is supplied over a bootstrap circuit, a single 15 V source is sufficient to supply the entire gate drive circuit.

The integrated protection circuit protects the device in case of overcurrent and under-voltage situations. Both the HVIC and the LVIC have an integrated under-voltage protection circuit (UVP).
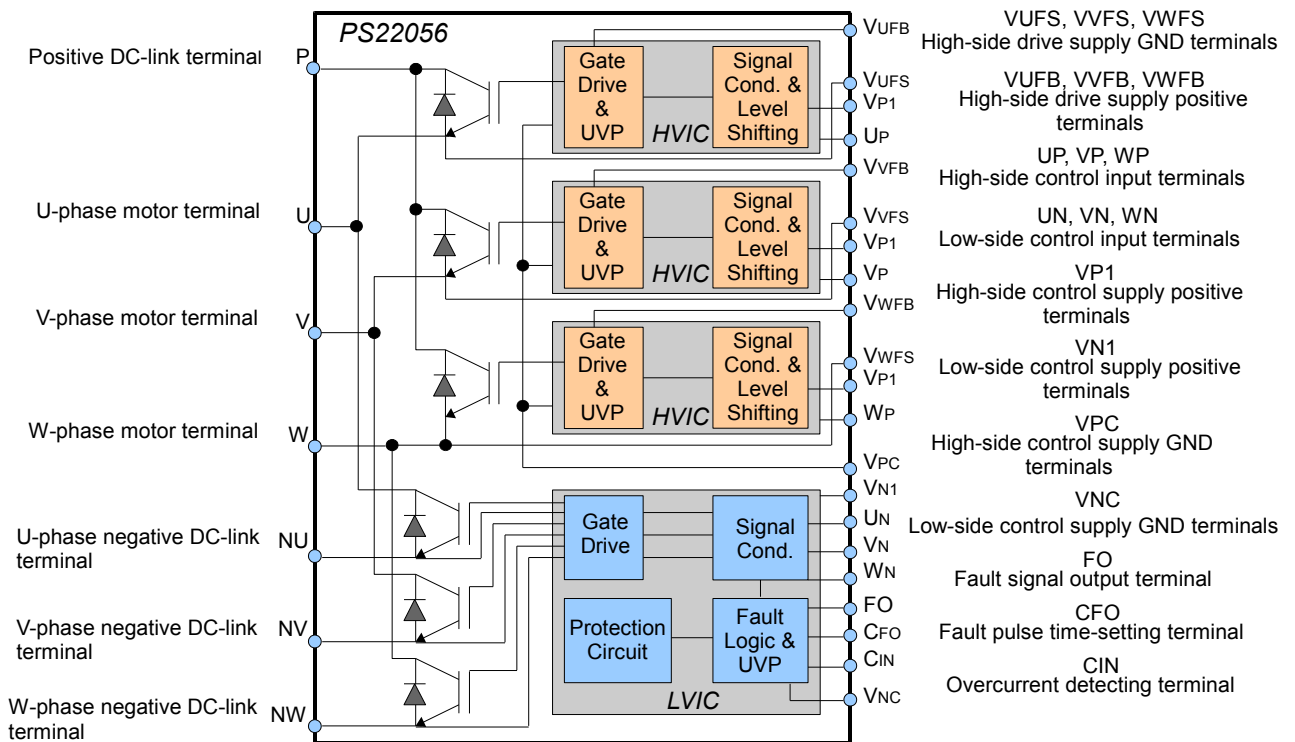

Figure 5.8 IPM PS22056: Internal circuit and pin-configuration

If the voltage drops below the 12.5 V threshold value, the IGBTs will be automatically turned off. The LVIC will also generate a fault output (FO) signal. If an under-voltage situation occurs on the HVIC-side, the high side IGBTs will be turned off but no fault signal will be generated.

An external circuit is responsible for the detection of an over-current. The C_{IN} terminal of the IPM is connected with the output of this circuit. If the voltage at this pin exceeds a certain threshold value (typically 0.5 V), the protection circuit of the IPM will recognize the over-current situation and will turn off all IGBTs. At the same time the FO signal is generated. The pulse width of this signal can be set over an external capacitor between the terminals C_{FO} and V_{NC}.

The characteristics of the IPM (e.g. maximal ratings, static and switching characteristics) are presented in the appendix.

Regarding the heat sink for the IPM, it must be mentioned that this had to be connected to the negative rail of the DC-link (ground of the electronic). There are parasitic capacitances between the IGBTs and the aluminium heat spreader of the IPM and the heat sink, which increases very much the value of the generated EMI. This high EMI disturbs the proper functioning of the electronic. By connecting the heat sink to ground (i.e. negative DC-link), a small-impedance path is created for the parasitic currents and the generated EMI is kept therefore at low values.

5.2.3.1. Bootstrap circuit

One voltage source (typical recommended value of 15 V) will supply the LVIC circuitry. By using bootstrap capacitors, the same voltage source is used to supply also the gate drivers of the HVIC units, as shown in Fig. 5.9. For each inverter phase the bootstrap circuit consists of an ultra fast recovery diode D_B, a charge current limiting resistor R_B and a floating supply capacitor C_B. The diode must block voltages equal to the maximal rated collector-emitter voltage of the IPM (1200V) and must have a recovery time below 100 ns. In order to protect the circuit from dangerous transients of the voltage supply, one Zenner-diode will be used to clamp the voltage at a certain level. Undesired high-frequency oscillations are eliminated by low-impedance ceramic capacitors. Before the PWM-operation starts, the low-side IGBTs are turned on, in order to allow the charging
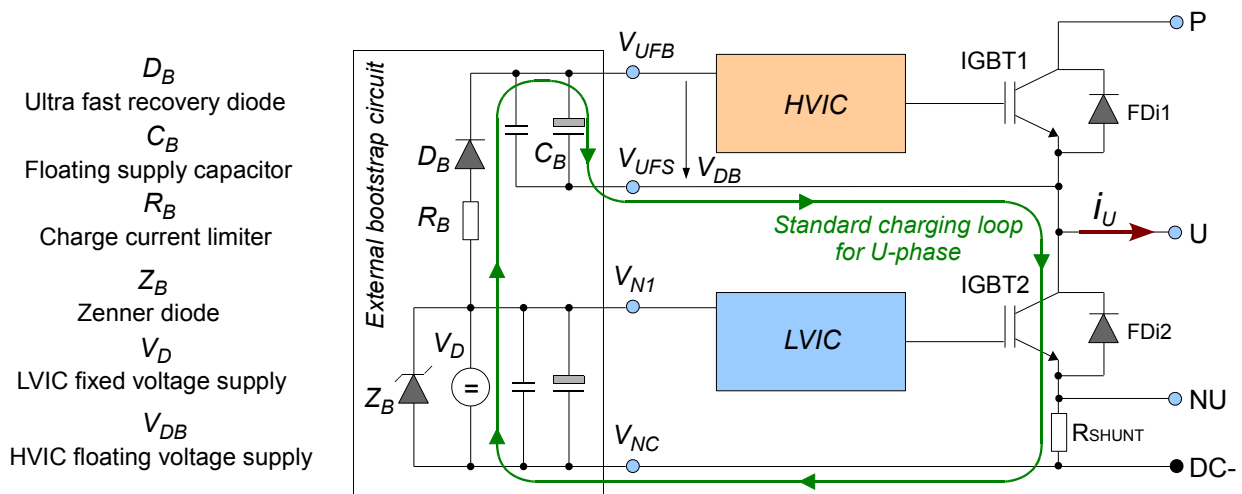

D_B
Ultra fast recovery diode
C_B
Floating supply capacitor
R_B
Charge current limiter
Z_B
Zenner diode
V_D
LVIC fixed voltage supply
V_{DB}
HVIC floating voltage supply

Figure 5.9 The bootstrap circuit for one IPM-leg

of the bootstrap capacitors. In Fig. 5.9, during the PWM operation, the voltage of the capacitor C_B will float depending on the potential of the terminal V_{UFS}. When IGBT1 is turned on, the bootstrap voltage V_{DB} will decrease due to the current consumed by the drive circuit. Before turning on IGBT2, there will be a dead time when both switches are turned off. If the motor current in the U-phase is positive, than the diode FDi2 will conduct and the bootstrap capacitor can recharge. For a negative phase current, V_{DB} will continue to decrease as the diode FDi1 is conducting. When IGBT2 is turned on the bootstrap voltage will increase again.

5.2.3.2. Current measurement and over-current protection

The current in each motor phase was measured by shunt resistors, which are connected between the emitters of the low-side switches and the negative rail of the DC-link. Their advantages in comparison with hall-effect sensors are the low price and the linearity within a wide range of frequency spectrum. The following aspects must be considered though when using this measurement method:

- The current can be measured only if the low-side switches are turned on. For the common PWM techniques this is usually done during the zero voltage vector $\underline{U}_0$ (Fig. 2.5)
- The modulation method is important for the accuracy of the measurement at high switching frequencies and high modulation indexes
- It is not possible to detect eventual short circuits between the motor phases and the grounded motor enclosure
- The ground of the measurement circuitry is connected to the negative rail of the DC-link
- The shunts must have small tolerance, very low inductance and should be stable with temperature variations

The star connection of the motor phases allows the measurement of only two phase-currents because the third is redundant. The measurement is possible only when the low-side switches are turned on and at modulation indexes near to one, an accurate measurement can fail due to the transients of the measurement circuit. Using a shunt for each phase allows the measurement of those two phase-currents for which the low-side switches have the largest turn-on times. Even so, there are some values of the voltage space vector for which a precise current measurement is still difficult, as shown in Fig. 5.11.

Regarding the modulation methods, these can be split in two main categories:

- Continuous modulation methods, where a switching action occurs in each inverter leg at every sampling interval. These methods are using both zero voltage vectors $\underline{U}_0$ and $\underline{U}_7$
- Discontinuous modulation methods, where switching actions occur only in two inverter legs at every sampling interval. These methods are using only one of the zero voltage vectors, so that the non-switching inverter leg is clamped either to the positive or the negative DC-link

The assessment of the modulation methods is made in the literature [27], [55] by means of the produced current distortion for different modulation indexes. For modulation indexes smaller than 0.8, the total harmonic power losses are smaller for continuous modulation methods, as

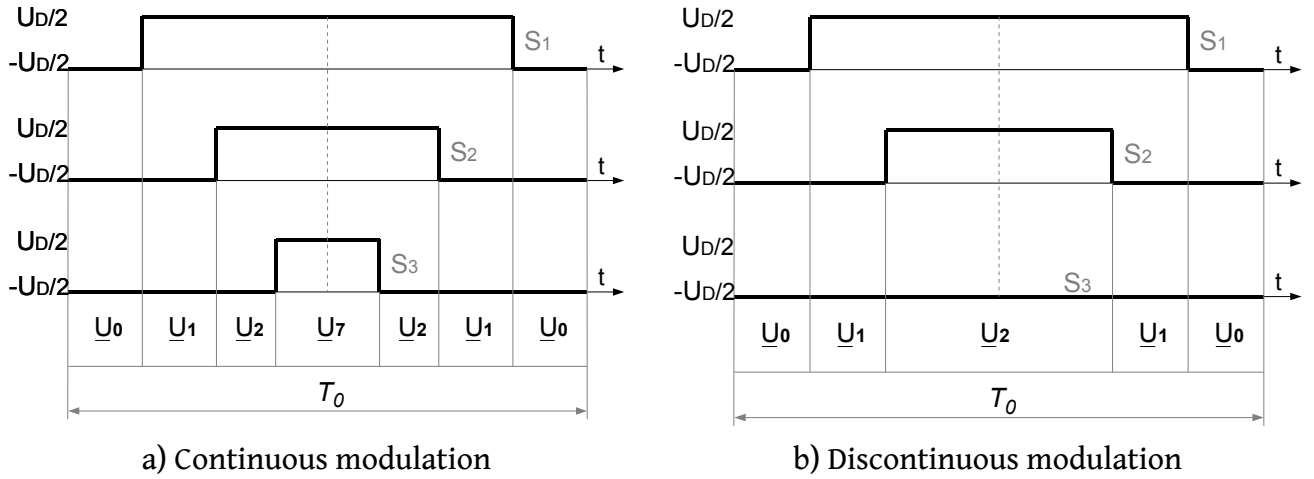| a) Continuous modulation | b) Discontinuous modulation |

Figure 5.10 Modulation methods

those presented in the Fig. 2.7, compared with discontinuous modulation methods (e.g. 60° and 120° Flat-Top). For higher modulation indexes the situation reverses. Regarding the harmonic power losses, the average value of the modulation index is therefore a factor in deciding upon the most appropriate modulation method. In applications where the value of the common-mode voltage is of big concern, discontinuous modulation methods are more appropriate. For this experimental set-up the modulation shown in Fig. 2.7b was used (continuous modulation method). The conventional space vector modulation is a continuous modulation method, where the phase of the reference voltages u_{Saref}, u_{Sbref} define the active sector and their amplitudes decide upon the turn-on period of the switches. For the carrier based continuous modulation methods the commutation times for each inverter leg are calculated easy from the reference phase voltages. Two such methods were presented in the second chapter in Fig. 2.7. For these methods, by adding the offset voltage component u_{ofs} to the inverter's output voltages, the potential of the star point u_{S0} is modified without affecting the phase voltages (defined in the Figs. 2.5 and 2.6). The upper index md in the equation (5.1) denotes the modified value of a variable due to u_{ofs}.

$$u_{S1}^{md} = \frac{2}{3}\left(\underbrace{u_{10}+u_{ofs}}_{u_{10}^{md}}\right) - \frac{1}{3}\left(\underbrace{u_{20}+u_{ofs}}_{u_{20}^{md}}\right) - \frac{1}{3}\left(\underbrace{u_{30}+u_{ofs}}_{u_{30}^{md}}\right) = u_{S1}$$

$$u_{S0}^{md} = \frac{1}{3}\left(u_{10}+u_{ofs}+u_{20}+u_{ofs}+u_{30}+u_{ofs}\right) = \frac{u_{10}+u_{20}+u_{30}}{3}+u_{ofs} = u_{S0}+u_{ofs}$$

(5.1)

The mean value of the inverter's output voltage over a sampling period will be determined by the turn-on period t_{onY} of the low-side switches:

$$u_{Y0} = \frac{1}{T_0}\left[-\frac{U_D}{2}t_{onY}+\frac{U_D}{2}\left(T_0-t_{onY}\right)\right] = U_D\left(\frac{1}{2}-\frac{t_{onY}}{T_0}\right) \quad ; \quad (Y=1,2,3)$$

$$t_{onY} = \left(\frac{1}{2}-\frac{u_{Y0}}{U_D}\right)T_0 \quad ; \quad u_{Y0} = u_{SYref}+u_{ofs}$$

(5.2)

The maximal turn-on periods t_{onY} of the low-side switches at maximal modulation index is:

Carrier based modulation (Fig. 2.7a and equation (2.22))

$$u_{S1ref} = u_{S1,min} = -\frac{U_D}{\sqrt{3}} \quad ; \quad u_{S2ref} = u_{S3ref} = \frac{U_D}{2\sqrt{3}}$$

$$U_{ofs} = -\frac{\left(u_{S2ref} + u_{S1,min}\right)}{2} = \frac{U_D}{4\sqrt{3}}$$

$$t_{on1,max} = T_0 \left(\frac{1}{2} - \frac{\frac{U_D}{4\sqrt{3}} - \frac{U_D}{\sqrt{3}}}{U_D} \right) = 93,3 \mu s \quad ; \quad T_0 = 100 \mu s \tag{5.3}$$

$$t_{on2,max} = t_{on3,max} = T_0 \left(\frac{1}{2} - \frac{\frac{U_D}{4\sqrt{3}} + \frac{U_D}{2\sqrt{3}}}{U_D} \right) = 6,7 \mu s$$

Carrier based (Schörner [28]) modulation (Fig. 2.7b and equation (2.23))

$$u_{S1ref} = u_{S1,min} = -\frac{U_D}{\sqrt{3}} \quad ; \quad u_{S2ref} = u_{S3ref} = \frac{U_D}{2\sqrt{3}} \quad ; \quad \left| \underline{u}_{S,max} \right| = \frac{\sqrt{3}}{2} U_D$$

$$U_{ofs} = -\frac{\left| \underline{u}_{S,max} \right|}{\sqrt{3}} - u_{S1,min} = -\frac{U_D}{2} + \frac{U_D}{\sqrt{3}}$$

$$t_{on1,max} = T_0 \left(\frac{1}{2} - \frac{-\frac{U_D}{2} + \frac{U_D}{\sqrt{3}} - \frac{U_D}{\sqrt{3}}}{U_D} \right) = 100 \mu s \quad ; \quad T_0 = 100 \mu s \tag{5.4}$$

$$t_{on2,max} = t_{on3,max} = T_0 \left(\frac{1}{2} - \frac{-\frac{U_D}{2} + \frac{U_D}{\sqrt{3}} + \frac{U_D}{2\sqrt{3}}}{U_D} \right) = T_0 \left(1 - \frac{\sqrt{3}}{2} \right) = 13,4 \mu s$$

The equations 5.3 and 5.4 show that for the current measurement at unity modulation indexes the Schörner modulation is more adequate than the modulation of Fig. 2.7a, because the maximal turn-on periods of the low-side switches are significantly larger. At maximal modulation index, the Schörner modulation becomes discontinuous. As shown in Fig. 5.11, the phase currents are always measured in the middle of the zero-voltage vector $\underline{U}_0$, at the beginning of each control cycle. Therefore the maximum allowed oscillation time of the measurement circuit t_{osc} is half of the maximal turn-on period of the low-side switches. The maximal value of t_{osc} is 3.35 µs for the modulation of Fig. 2.7a and 6.7 µs for the Schörner modulation. These are ideal values though because the dead-time effect was neglected. As shown in the appendix, the IPM requires a very large dead-time, namely 3.3 µs, so that the required value of t_{osc} becomes 3.4 µs for the Schörner modulation A reliable measurement isn't possible in this case with the modulation of Fig. 2.7a.
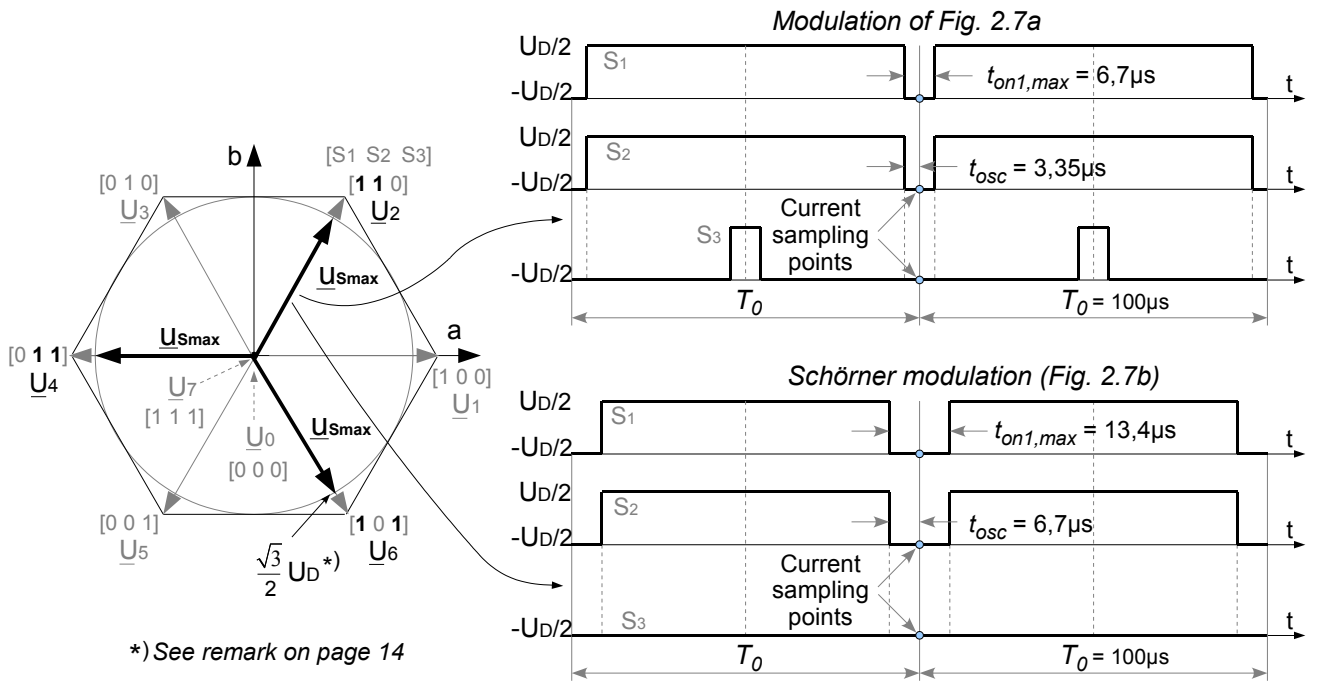
Figure 5.11 Characteristics of the modulation methods at unity modulation index

The measured value for t_{osc} is 4.9 µs (Fig. 5.12). This value exceeds with 1.5 µs the required value. An easy solution to avoid this inconvenient is to start the analog-to-digital conversion not at the beginning of the interrupt service routine, but with a fix delay of minimum 1.5 µs.
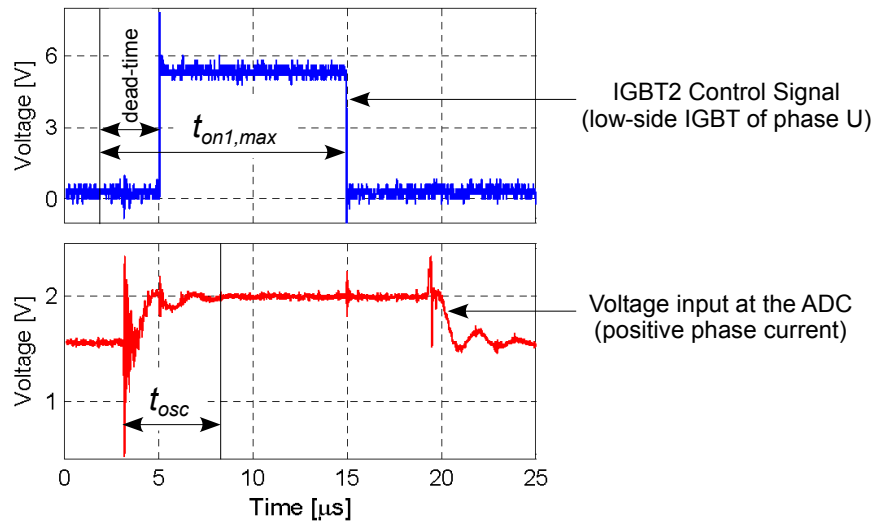

Figure 5.12 Characteristics of the current measurement circuit at unity modulation indexes

Conclusion: As known from literature [27], [55], discontinuous modulation methods are producing, for high modulation indexes (> 0.8), less harmonics than the continuous modulation methods (assuming a 50% increase in the switching frequency for the discontinuous modulation methods). For lower modulation indexes, the continuous modulation methods are offering better results. In this set-up, the Schörner modulation was used, as it offers the largest turn-on periods of the low side switches among the continuous modulation methods.
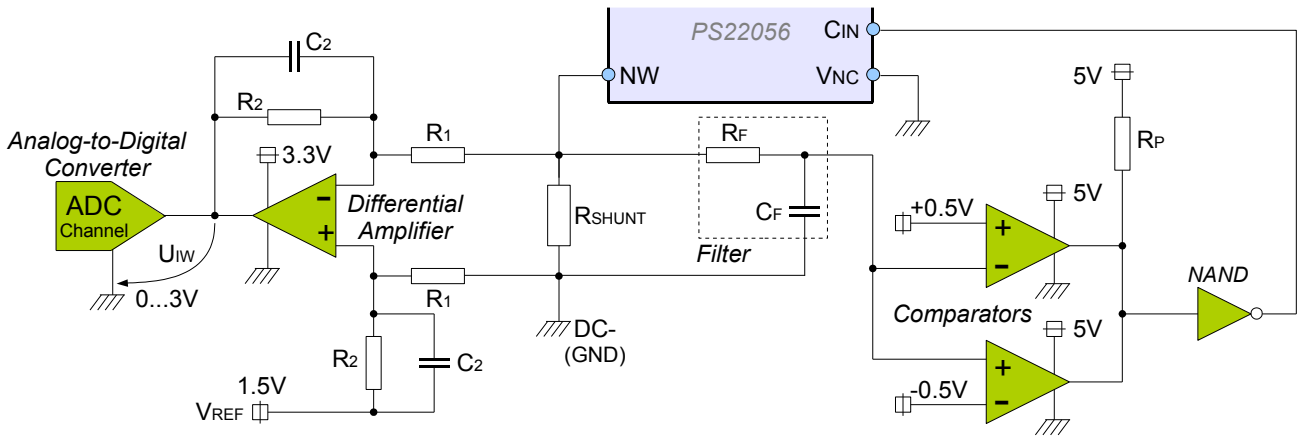
Figure 5.13 Current measurement and over-current protection for one inverter leg

The voltage drop on the shunt resistances will be amplified, level shifted and then digitally converted, as shown in Fig. 5.13. The shunt resistance is rated at 35 mΩ/3 W, has a tolerance of 0.5% and an inductance smaller than 3 nH. A positive current value of +12.5 A will correspond to an input voltage of 3 V at the ADC and a negative value of -12.5 A will correspond to 0 V. This is the maximum conversion range of the 12bit ADC.

The main controller of the DCU, the TMS320F2812 DSP from Texas Instruments, will turn off all switches if one of the phase currents reaches ±12.5 A. Beside this software protection, a hardware protection based on comparators was implemented. Two comparators are used for each inverter leg to detect both positive and negative currents. An overcurrent is detected around the value of ±15 A. The outputs of all six comparators are forming an AND-connection. This is connected to the C_{IN} terminal of the IPM over a NAND-gate (Fig. 5.13). The input of the comparators has to be low-pass filtered in order to avoid undesired fault conditions due to noise. The time constant of this filter was set at 1.5 μs. Fig. 5.14 shows the reaction of the protection circuit in case of an overcurrent. The active-low fault signal is connected with the PDPINT terminal of the mentioned DSP, which assures that all switches are turned off.
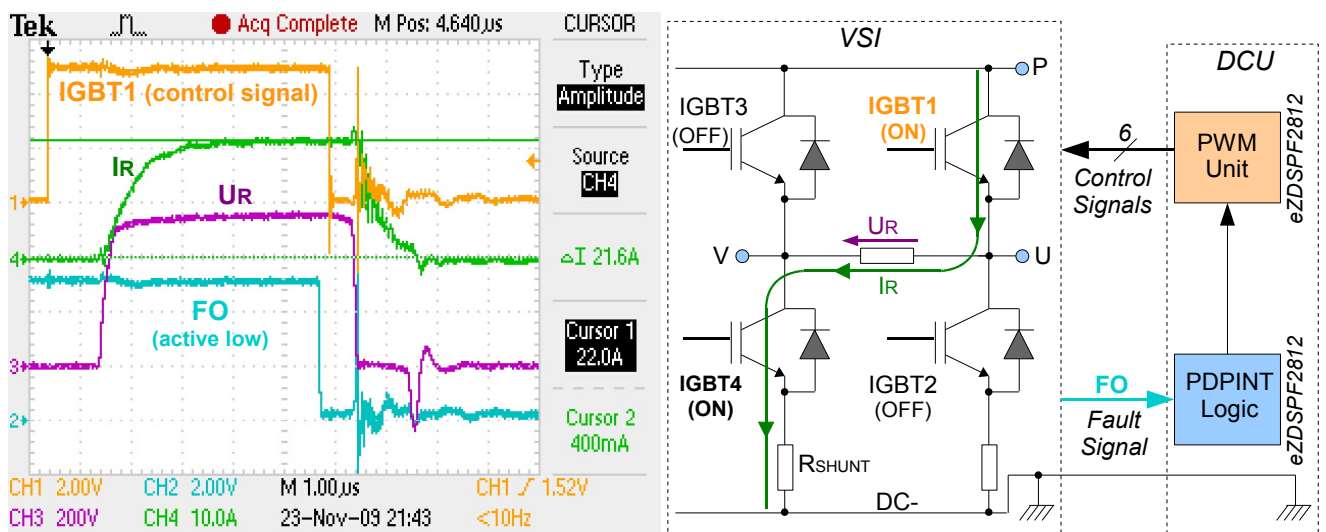

Figure 5.14 Overcurrent protection test for one inverter leg

5.2.3.3. Dimensioning of the DC-link capacitors

The DC-link of a VSI contains four aluminium-electrolytic capacitors, connected as shown in Fig. 5.15, the corresponding voltage-sharing resistors and a snubber capacitor. The electrolytic capacitors are used to compensate the difference between the power requirement of the inverter and the output power of the diode bridge rectifier. They supply the input current of the inverter with pulse frequency and are a source of transient power peaks. The instantaneous value of the current flowing through the DC-link capacitors is the difference between the AC-component of the rectifier's output current and AC-component of the inverter's input current.

$$i_C = i_{D,ac} - i_{ac} \tag{5.5}$$

In [56] was shown that the current stress of the DC-link capacitors can be analytically determined in the time domain with sufficient accuracy for sinusoidal inverter output currents and constant DC-link voltage. Due to the symmetry of the ideal three-phase system and due to the phase-symmetric structure of the inverter, the current analysis was limited to a 60° interval of the inverter's output voltage fundamental period. By this, the RMS-value of the DC-link capacitor current is:

$$I^2_{C,RMS} = \frac{3}{\pi} \int_{\pi/3}^{2\pi/3} i^2_C \, d\varphi \tag{5.6}$$

where $\varphi = 2\pi f_N t$ and f_N is the output frequency of the inverter. Inserting (5.5) in (5.6) yields to:

$$I^2_{C,RMS} = I^2_{D,ac,RMS} + \frac{3}{\pi} \int_{\pi/3}^{2\pi/3} i_{D,ac} i_{ac} \, d\varphi + I^2_{ac,RMS} \tag{5.7}$$

As the terms $i_{D,ac}$ and i_{ac} do not contain harmonics in the same frequency range, the integral term of (5.7) can be neglected, so that:

$$I^2_{C,RMS} = I^2_{D,ac,RMS} + I^2_{ac,RMS} \tag{5.8}$$

The current contribution determined by the mains-commutated input rectifier depends on the imposed voltage ripple of the DC-link voltage. The output voltage of the bridge rectifier has a period of $f_G = 300 \, Hz$. Inside this period the DC-link capacitors will be loaded during the time:

$$t_C = \frac{\arccos\left(\dfrac{U_{D,min}}{U_{D,max}}\right)}{2\pi \underbrace{f_{mains}}_{50Hz}} \tag{5.9}$$

The difference between the maximal DC-link voltage $U_{D,max}$ and the minimal value $U_{D,min}$ defines the voltage ripple. The current peak value during the charge time is:

$$I_{t_C} = C_{EL} \frac{U_{D,max} - U_{D,min}}{t_C} \tag{5.10}$$

where C_{EL} represents the DC-link capacitance of one VSI.

The corresponding RMS-value is:

$$I_{t_C,RMS} = \sqrt{I^2_{t_C} \cdot t_C \cdot f_G} \tag{5.11}$$

Similarly for the discharging time t_{DC}, the corresponding RMS-value is:

$$I_{t_{DC},RMS} = \sqrt{I^2_{t_{DC}} \cdot t_{DC} \cdot f_G} \tag{5.12}$$

The total current RMS-value from the rectifier side will be:

$$I_{D,ac,RMS} = \sqrt{I^2_{t_C,RMS} + I^2_{t_{DC},RMS}} \tag{5.13}$$

The worst-case current stress estimation, presented in [56] as a basis for the dimensioning of the DC-link capacitor is:

$$I_{ac,RMS} \approx \frac{I_{N,RMS}}{\sqrt{2}} \tag{5.14}$$

The selected electrolytic capacitor is rated at 330 µF/400 V and has a tolerance of ±20%. The total capacitance of the DC-link is approximately 1.5 mF. The value of the desired voltage ripple was set at ±2 V. With these values, by using the equations (5.8)-(5.14) the current RMS-value for the DC-link capacitors of one VSI is $I_{C,RMS} \approx 5.85\,A$. The maximal continuous current supported by the selected capacitor is 3.84 A, so that the parallel connection from Fig. 5.15 had to be used, where each capacitor conducts the half of the current stress value $I_{C,RMS}$.

The voltage rating of the electrolytic capacitor is selected based on the DC-link voltage and tolerance values of the capacitors. The minimal voltage value, which has to be supported by one electrolytic capacitor, is:

$$U_{Cap,\min} = \frac{U_D \cdot tolerance_{\max}}{tolerance_{\max} + tolerance_{\min}} = \frac{560V \cdot 1.2}{1.2 + 0.8} = 336\ V \tag{5.15}$$

Because stray inductances are present between the electrolytic capacitors and the P, NU, NV, NW terminals of the IPM, a snubber capacitor must be used to protect the IPM against high surge voltages. It provides a low inductance path during the switching operation and therefore is placed as closed as possible to the IPM terminals.

5.2.3.4. The interface with the Distributed Control Unit and the electronic supply

The interface between the VSI and the DSP-board of the DCU is shown in Fig. 5.15. The current measurement circuit is connected with the analog circuit of the DSP-board. On the digital side of the interface, voltage transceivers are used. They act like line drivers and translate also the voltage between the DSP-board and the IPM from 3.3 V to 5 V respectively and vice versa, as the DSP is only 3.3 V compatible. The electronic supply of a servo-controller unit is realised by an AC/DC converter, which has to isolate, in continuous operation mode, the voltage $U_D/2$. Voltage regulators are used to obtain other necessary voltage levels than those generated by the AC/DC
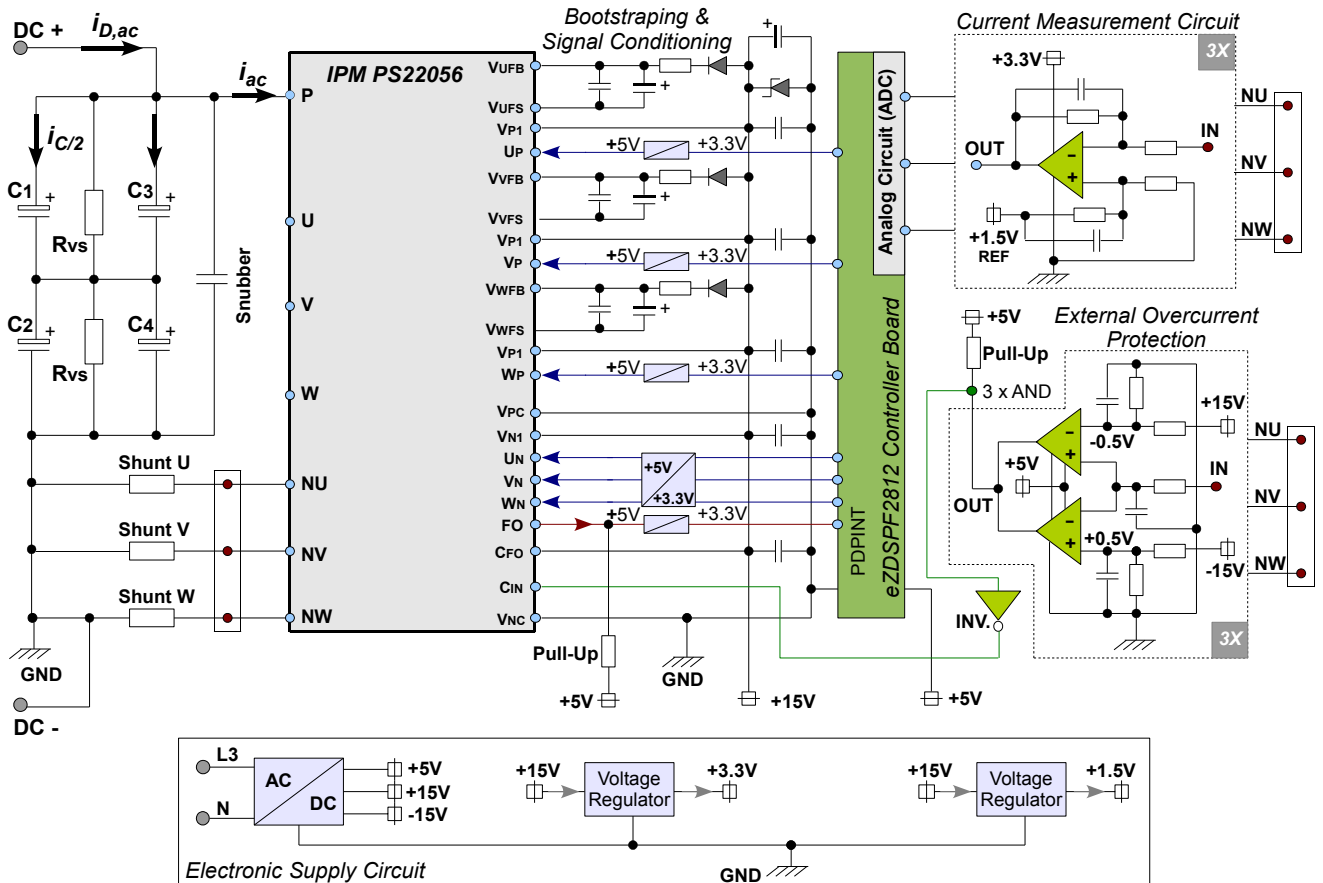
Figure 5.15 Structure of the VSI and the DCU interface

converter. In case of a failure of the AC/DC converter or of an interruption of the mains' voltage during normal operation, the bootstrap circuit as well as the DC-link capacitance are still charged. The bootstrap voltage remains above the under voltage threshold value of the IPM for few milliseconds during which short circuits could occur. A single voltage transceiver is used for the six control signals (+3.3 V to +5 V translation). In order to avoid possible short circuits in this case, pull-down resistances (not shown in Fig. 5.15) are used for the outputs of this transceiver, which avoid erroneous switching if the control signals from the DSP are floating or if they are in high impedance state.

5.3. The Information Processing Unit

At the IPU-level there are four DCUs and the CCU. One DCU together with a VSI builds a modular servo-controller.

5.3.1. The Distributed Control Unit

The DCU contains a main controller and the associated communication interfaces:

- The position sensor interface
- The interface with the adjacent DCUs (SPI-interface)
- The interface with the CCU (EtherCAT-interface)

The main controller is the TMS320F2812 DSP from Texas Instruments, which has a fixed-point arithmetic and a maximal processing frequency of 150 MHz. Its cost and characteristics of the CPU and peripheral units makes it a suitable solution for servo-drive applications [57]. The DSP-board eZDSPF2812 was selected for the set-up. Its main characteristics are shown in table 5.2.

The virtual floating-point engine *IQmath* from Texas Instruments was used in order to avoid the difficulties due to the fixed-point arithmetic. The *IQmath* routines for e.g. computing trigonometrical functions are executed very fast and with a very good accuracy [58].

			Main board components	Functionality
eZDSPF2812 Board	TMS320F2812 Controller	CPU	150 MHz, 32-Bit Harvard Bus-Architecture, 32x32 Bit MAC Operations, C/C++ Code Compilers, Fixed-point Arithmetic, 8 Level Pipeline	Fast code execution. The initialisation procedures, the sensorless field oriented control and the communication tasks are executed in less than 100 µs.
		Peripheral Units	IEEE 1149.1 JTAG Interface	Connection with the JTAG Controller.
			External Memory Interface (XINTF)	Connection with the EtherCAT ASIC and other external memories.
			126 kW internal Flash-memory	Stores the code of the embedded system.
			EVM-PWM	Inverter control with integrated dead-time.
			EVM-QEP	Decoding of the signals from the position sensor.
			AD Converter Module	Simultaneous sampling of two phase-currents.
			SPI, McBSP (SPI-Compatible)	Direct connection between two adjacent DCUs.
	64 kW external memory			Storage of different state variables.
	JTAG Controller (Connection with the PC)			Program debugging and internal Flash writing.
	I/O Analog and Digital Ports			Access to almost all pins of the controller.

The AD converter module has a total of 16 channels, equally separated in two sequencers, a 12-bit converter and two dual sample and hold units. The output voltages of the differential amplifiers, corresponding to the motor phase-currents, are connected to six AD-channels, as shown in Fig 5.16. It is possible like this to measure simultaneously any two phase-currents for which the low-side switches have the largest turn-on times. At the end of a control cycle a pair of channels, that is to be converted in the next cycle, is selected. The start of conversion is hardware-triggered with a delay of 1.5 µs after the beginning of a control cycle.

The high gain and offset errors of the ADC unit had to be first compensated before using the DSP-board for the current measurement.

The DSP has two identical event manager (EVM) modules. One module includes general-purpose timers, a PWM unit, a capture unit and a quadrature-encoder pulse (QEP) unit. The PWM unit can generate three independent output pairs with programmable dead-time and output polarity.
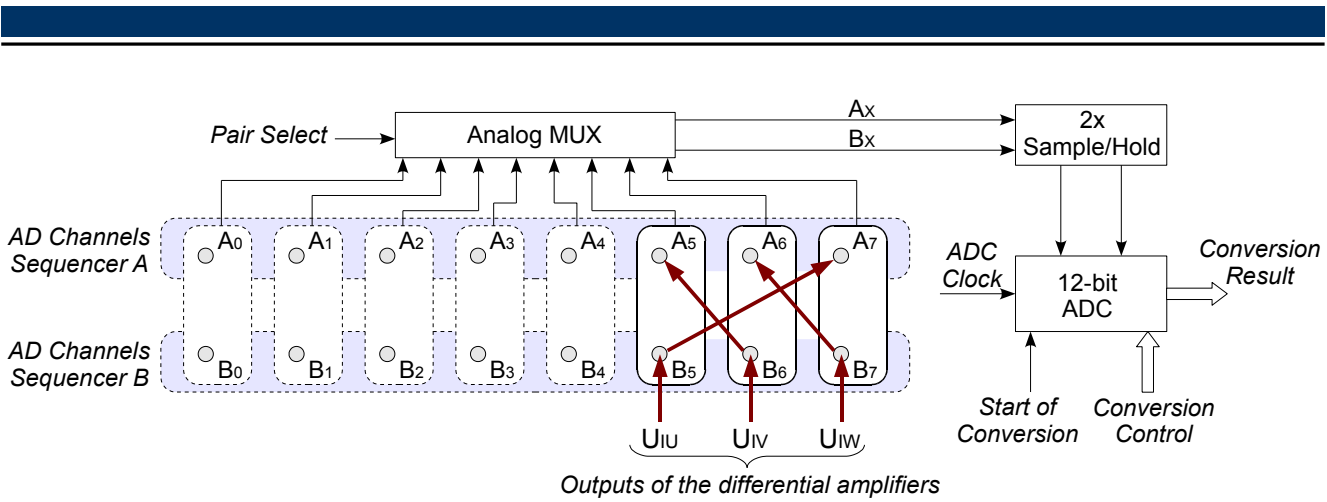
Figure 5.16 Simultaneous sampling and conversion of any two phase-currents

5.3.1.1. The interface with the position sensor

The incremental position sensor mounted on the vehicle delivers the position by means of two symmetrical digital signals, which are phase-shifted by 90°. These signals are transmitted over the same RS485 lines to all four DCUs, as shown in Fig. 5.17.

It is the QEP circuit of the DSP, which is responsible for decoding these signals. Because the electronic of the servo-modules is tied to the negative rail of the DC-link and the sensor unit is connected to protection earth (PE), the sensor interface must be electrically isolated. This was realized with digital isolators. A PE line and a 5 V line are also transmitted along the sensor data cable, in order to supply the local RS485 receivers and digital isolators.
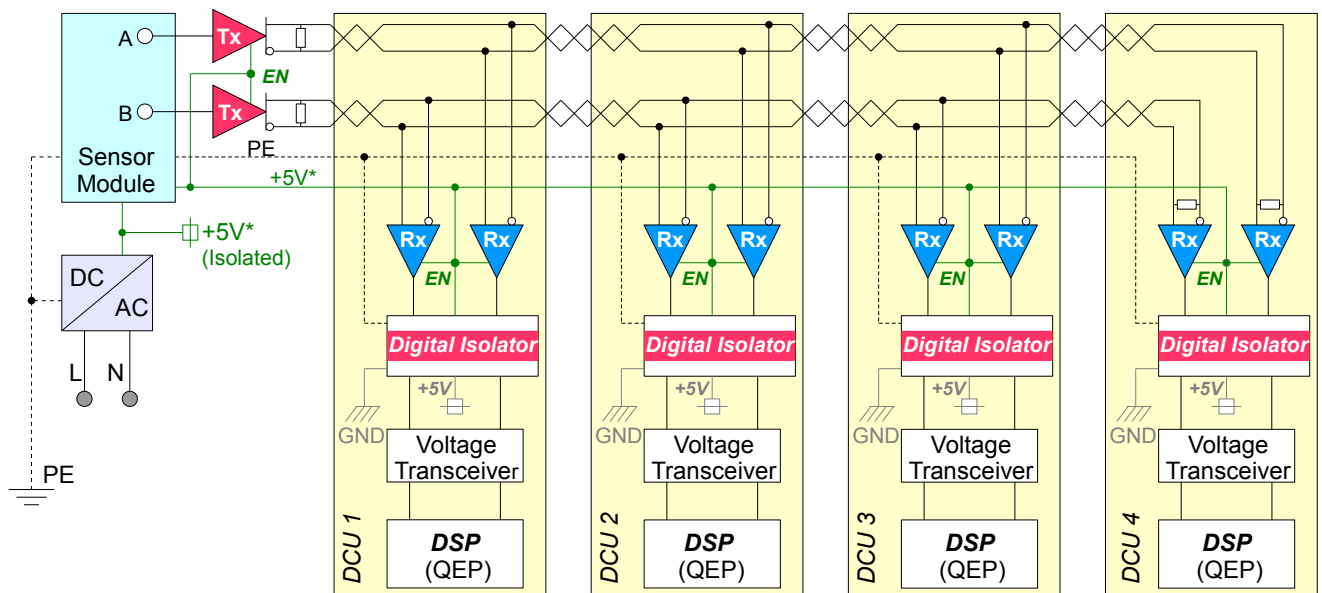

Figure 5.17 Interface between the DCUs and the sensor unit

5.3.1.2. The interface with the adjacent Distributed Control Units

As presented in the third chapter, the modular servo-controller must be able to communicate with two adjacent modules. For this task the two SPI compatible units of the DSP were used:

- The SPI unit

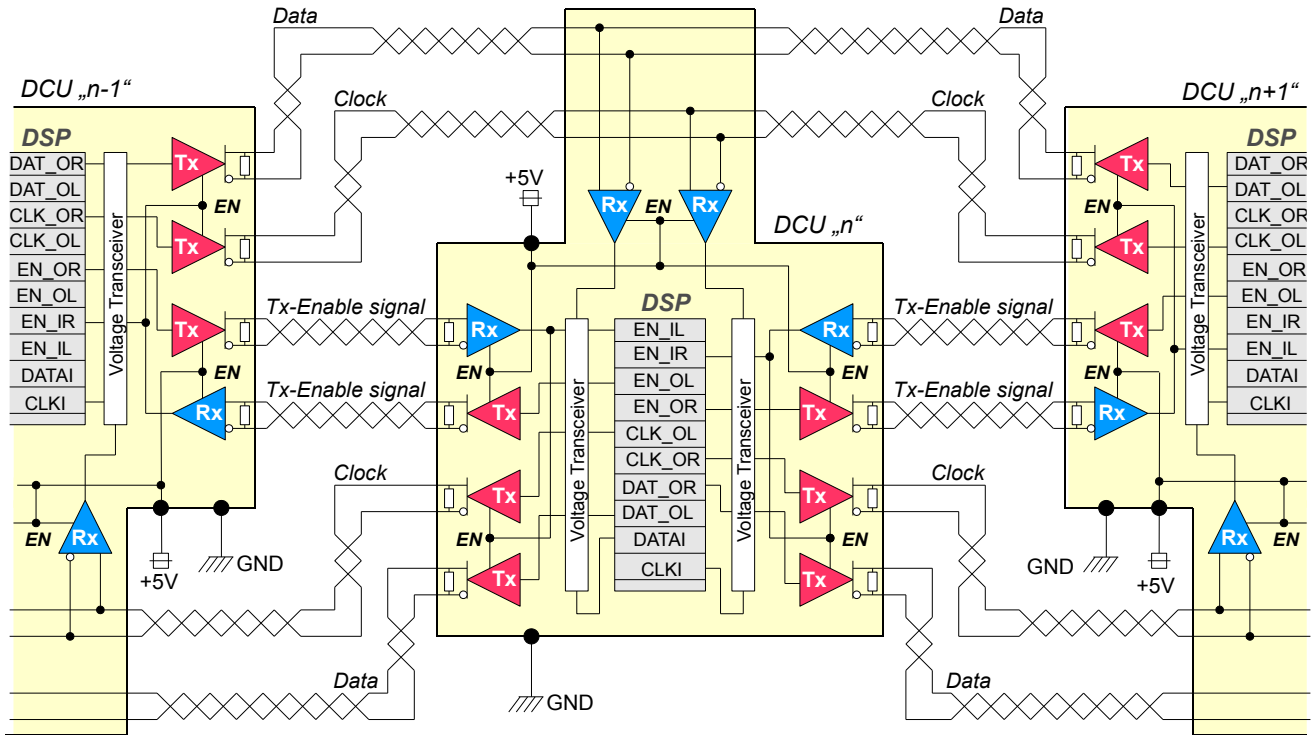- The multi-channel buffered serial port (McBSP) unit.

Figure 5.18 SPI-based interface for communication with the adjacent modules

DAT_OR, CLK_OR	SPI data and clock output signals towards the DCU on the right side
DAT_OL, CLK_OL	SPI data and clock output signals towards the DCU on the left side
EN_IR, EN_OR	Transmit-enable input and output signals from/to the DCU on the right side
EN_IL, EN_OL	Transmit-enable input and output signals from/to the DCU on the left side
DATAI, CLKI	SPI data and clock input signals

Table 5.3 Signal description of the SPI-based interface

The maximal data transfer speed allowed by the DSP-board is 12.5 Mbps, which fully satisfies the bandwidth demands in this case. At the physical layer the RS485 differential data transmission protocol is used, as the data transmission must be immune to the switching noise and the RS485 transceivers are cheap and robust. Each DCU contains six transmitter and four receiver ports. The SPI data and clock signals can be transmitted or received only to or from one neighbour DCU at a time, in order to avoid short-circuits on the communication lines. All receiver ports and two of the transmitter ports are always enabled. The other four transmitter ports, responsible for the data and clock signal transfer to the adjacent modules, are enabled/disabled by external signals coming from the corresponding adjacent DCUs (Fig. 5.18).

The transmit-enable input and output signals from table 5.3 are GPIO signals and are not part of the SPI protocol.

5.3.1.3. The interface with the Central Control Unit

The CCU communicates with the DCUs over the EtherCAT fieldbus. The standardized EtherCAT protocol is completely hardware implemented and there are now many ASICs available, which

implement it. For this application the slave controller ET1100 was used to transform the DCU in an EtherCAT slave unit [59]. It has three different process data interfaces (PDI):

- A 16/8-bit asynchronous microcontroller interface
- An SPI interface
- A 32-bit digital I/O interface

Only one PDI interface can be used at a time. The EtherCAT slave-board FB1111-140 from *Beckhoff* offers an easy access to the microcontroller interface of this ASIC and was used here for a fast integration of EtherCAT in the structure of the DCU. The DSP sees the ESC as a common memory unit. The external memory interface of the DSP allows the connection of up to three different memory units. One memory unit is the 64 kWord RAM already available on the DSP-board, the second unit is the ESC and the third unit is a 128 kByte Flash chip, which serves as an additional non-volatile memory for general data. These three memory units share the same non-multiplexed address and data buses and are accessed by the DSP over different chip-select signals. The EtherCAT interface along with the other two memory interfaces is shown in Fig. 5.19. The abbreviations in Fig. 5.19 are explained in the Table 5.4.
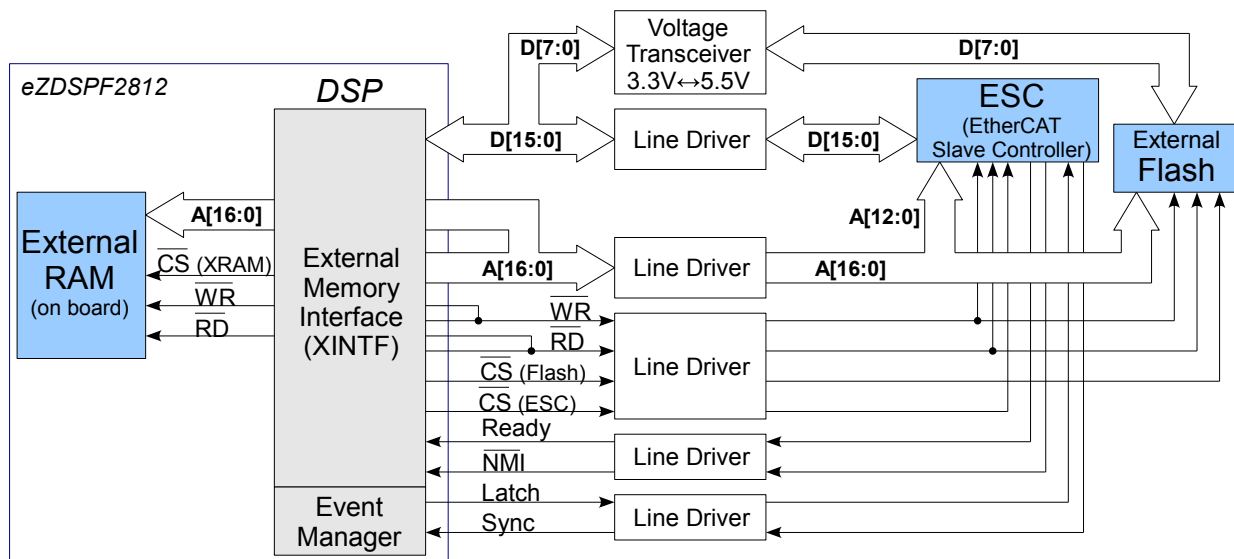

Figure 5.19 The EtherCAT and memory interfaces for the DSP

CS	Chip-select signal (active low)
WR	Memory write-access signal (active low)
RD	Memory read –access signal (active low)
Ready	Signal used by the ESC to extend the active time of the read/write access
NMI	Non-maskable interrupt signal used by the ESC for high-priority events (active low)
A[16:0]	Address signals
D[15:0]	Data signals
Latch	Signal used by the ESC to time-stamp different DSP actions
Sync	Signal generated at specific system times according to an internal clock of the ESC

Table 5.4 Signal description of the EtherCAT interface for the DSP

The external Flash is 5 V compatible. The ESC and the DSP are 3.3 V compatible. A voltage transceiver is required for the data lines between the DSP and the external Flash. For the address lines between them, a voltage translation wasn't necessary because the TTL inputs of the Flash are compatible with the LVTTL outputs of the DSP. The signal wiring between the DSP board and the ESC board reaches lengths of up to 30 cm and is situated in the proximity of the IPM, being therefore exposed to high EMI values. Line drivers had to be implemented to amplify the power of these signals.

The process memory of the ESC has 8 kByte, so that 13 address lines were used to access it.

Most part of the EtherCAT interface is implemented using the external memory interface of the DSP. The last two signals of the table 5.4, *Latch* and *Sync*, are not part of this XINTF, as shown in Fig. 5.19. *Latch* is a general-purpose output signal and *Sync* is connected to the capture unit of the EVM. Usually these signals are dedicated to the "Distributed Clock" unit of the ESC.

At the physical layer, the interface between the DCUs and CCU is specified by the IEEE 802.3 standards, which implies voltage isolation between the communication nodes by pulse transformers. These transformers are typically rated for an isolation voltage of 1.5 kV. This is also the case for the network board of the EtherCAT master and the above mentioned EtherCAT slave-board. This voltage is of course sufficient for the connection between two adjacent modules, which have the ground potential connected to the same negative rail of the DC-link. But because the potential of the EtherCAT master unit (PC) is at PE, the connection to the first EtherCAT slave-unit must guarantee the same isolation voltage level as the IPM, namely 2.5 kV. This value depends on the voltage blocking value of the IGBTs [60] and corresponds to the standard IEC1287.

For this reason, a simple network-isolating board having a 4 kV pulse transformer was implemented as shown in Fig. 5.20, in order to connect the master PC with the first EtherCAT
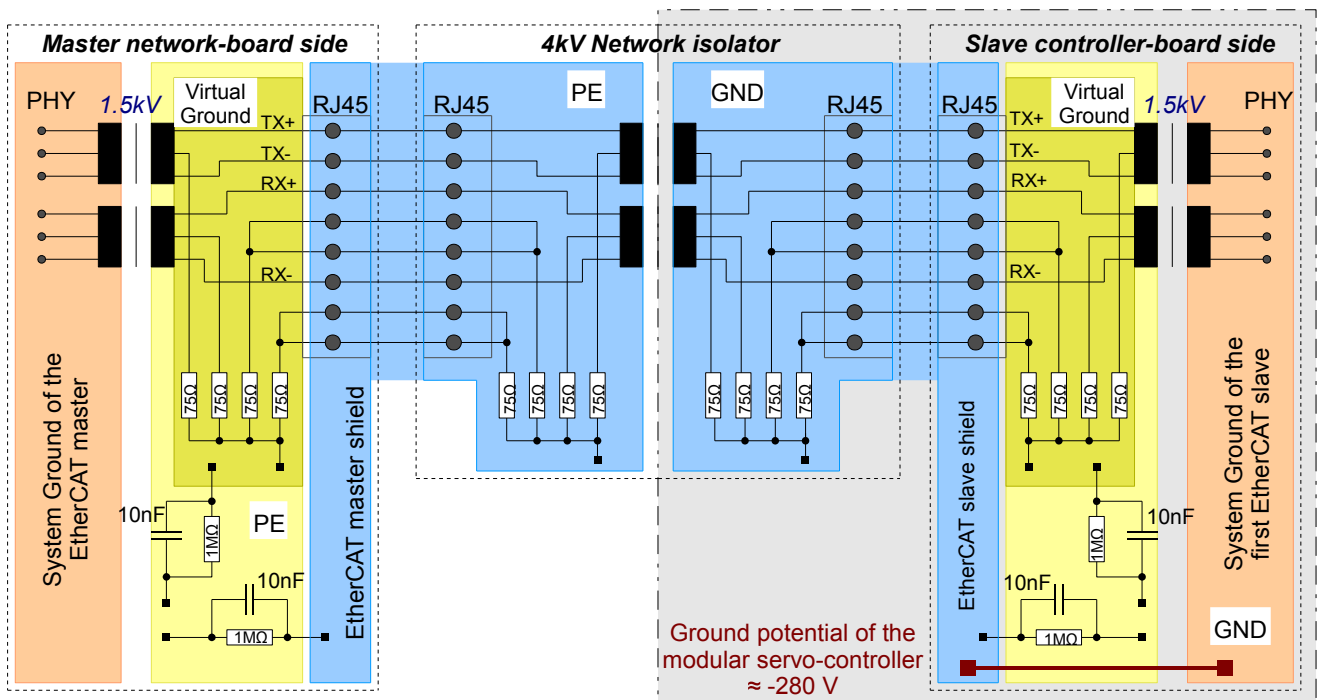

Figure 5.20 The implemented network isolator

slave unit in the system. The centre taps of the pulse transformers are connected to a virtual local ground over 75 Ω terminators in order to reduce the common-mode interference on the two pairs of active wires. The unused pairs of signals are tied directly, also over 75 Ω terminators, to the same virtual ground. The virtual ground and the shield are usually connected to PE over a 10 nF/500 V capacitor in parallel to a 1 MΩ resistance. For the first EtherCAT slave unit, the isolating property of the 1.5 kV on-board transformer is eliminated by a direct connection of the negative ground potential (-280 V) with the shield. Only the 4 kV transformer will support therefore eventual voltage stresses. This additional transformer will insert obviously more power losses on the transmission path and stress on the PHYs. The insertion-loss value as well as the return-loss and cross-talk values have been determined for the topology in Fig. 5.20 according to the IEEE802.3 specifications and they are not exceeding the imposed values.

The block diagram with the structure of the modular servo-controller is shown in Fig. 5.21.

5.3.2. The Central Control Unit

An ordinary PC represents the CCU. It contains the software protocol stack required for the EtherCAT master. It needs at the hardware level only a standard network board with direct memory access (DMA) and the processor should have a low jitter (typically bellow 2 μs). No other special boards are required. At the software level the CCU contains the main following tools:

- TwinCAT, which implements the EtherCAT master functionality
- The operator interface, which includes the algorithms for motion coordination and monitoring (Visual Basic application)
- The CCS (Code Composer Studio), which is used for programming and debugging of the DSPs in the initial test phases. It is also used to download program code in the internal Flash memory of the DSPs
- MATLAB, which is used for off-line data analysis and representation

5.4. The Position Sensor Unit

The sensor unit is made of an incremental sensor module and a 2 m-long linear magnetic scale, which is mounted along the guideway and has a fixed pole pitch of 1 mm. The sensor module contains an anisotropic magneto-resistive (AMR) position sensor and a high-resolution 13bit interpolator. The measuring concept is based on the AMR-effect found in ferromagnetic materials, where the resistance of the material will change together with the angle between the current flowing through the material and a crossing magnetic field. The sensor module is mounted on the vehicle, so that the active head of the sensor is perpendicular and as close as possible to the magnetic scale. In this case the current vector is constant and the movement of the vehicle along the magnetic scale will produce the changing magnetic field. Two resistance bridges of the sensor, shifted in space by 90°, generate sine and cosine signals, which are afterwards digitally converted by the interpolation circuit and supplied at the output of the sensor module as quadrature encoded signals. The resolution of the sensor module is configured to 200 increments/mm.

This sensor unit is cheap, accurate and was easy to interface it with the DSP, but it is not an end solution for topologies with passive vehicles. For such topologies the optical sensors are the most common solution nowadays in industrial applications. They are very accurate but also very expensive (price/covered length). A cost-effective alternative, namely the capacitive sensor, has been recently investigated in [61], [62]. Beside the capacitive sensor, another relative cheap solution is the magnetostrictive sensor. It is an absolute sensor and has the advantage that it can measure the position also in curves, but it cannot deliver the actual position at every 100 µs [63].
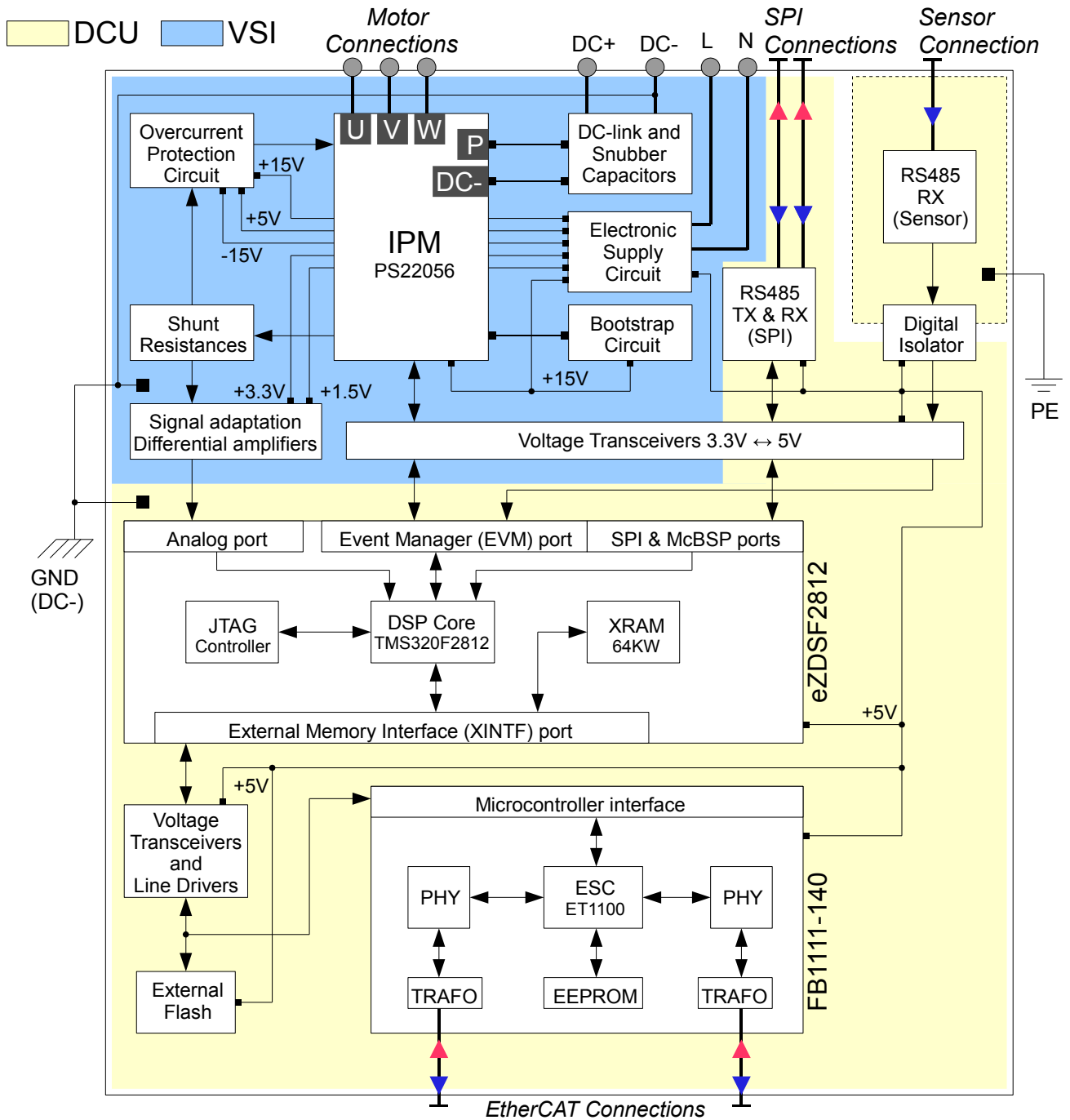

Figure 5.21 Structure of the modular servo-controller

6. Control results

As shown in Fig. 2.8 the position of the vehicle can be measured by means of a linear sensor or it can be estimated by using an EMF-based method, this if the vehicle moves with a certain minimal speed. Therefore, the EMF-based method alone cannot be used. A sensor is necessary for starting and stopping the vehicle. By differentiating the sensor's position, the speed of the vehicle is obtained. The value of the speed has a big noise component and must be filtered before being used as a feedback for the speed controller.

6.1. Sensor based control

6.1.1. Characteristic of the induced voltages

Before testing the control algorithm, it must be assured that the induced voltages in two adjacent segments are in phase, as expected from the mechanical construction. Otherwise phase compensation would have been necessary. Therefore, an off-line measurement was realized, where the vehicle was moved with an approximately constant speed during the transition between the first two segments. The voltage in the first motor phase, which corresponds to the induced voltage e_{Sa}, was measured simultaneously for both segments (Fig. 6.1).
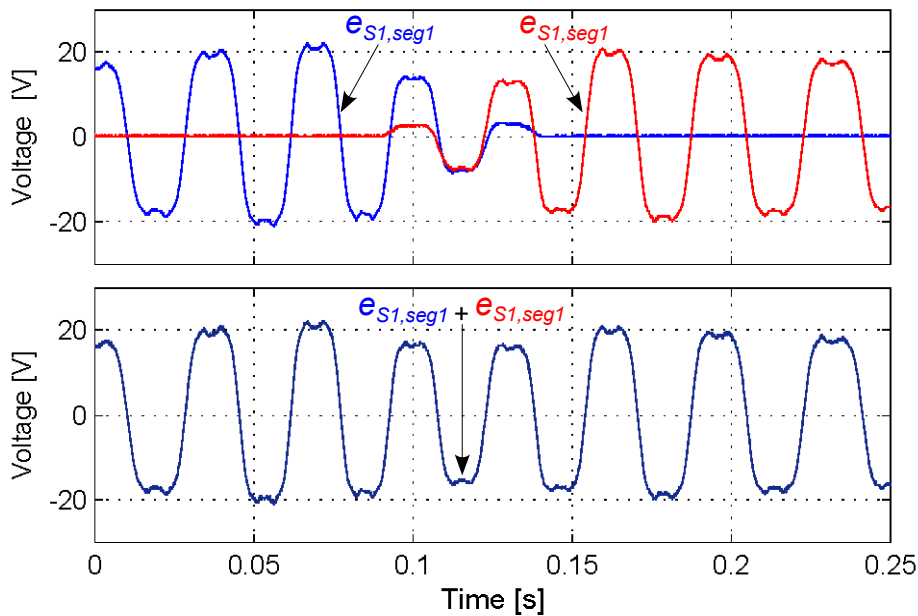

Figure 6.1 Off-line measurement of the induced voltages during the vehicle's transition period over the first two segments

Fig. 6.1 shows that the induced voltages in the first two segments are in phase and that there is a voltage drop in the sum of the two induced voltages during the transition period of the vehicle. Similar results were obtained for the other two segment transitions.

6.1.2. Position control of the vehicle

The following experimental results show the controlled position over the four stator segments. The vehicle starts from the initial position on segment $S1$ and crosses over segment $S2$, where it reaches the first position reference at 700 mm. Then it crosses over to the segments $S3$ and $S4$ respectively, where it finally reaches the last position reference at 1700 mm.
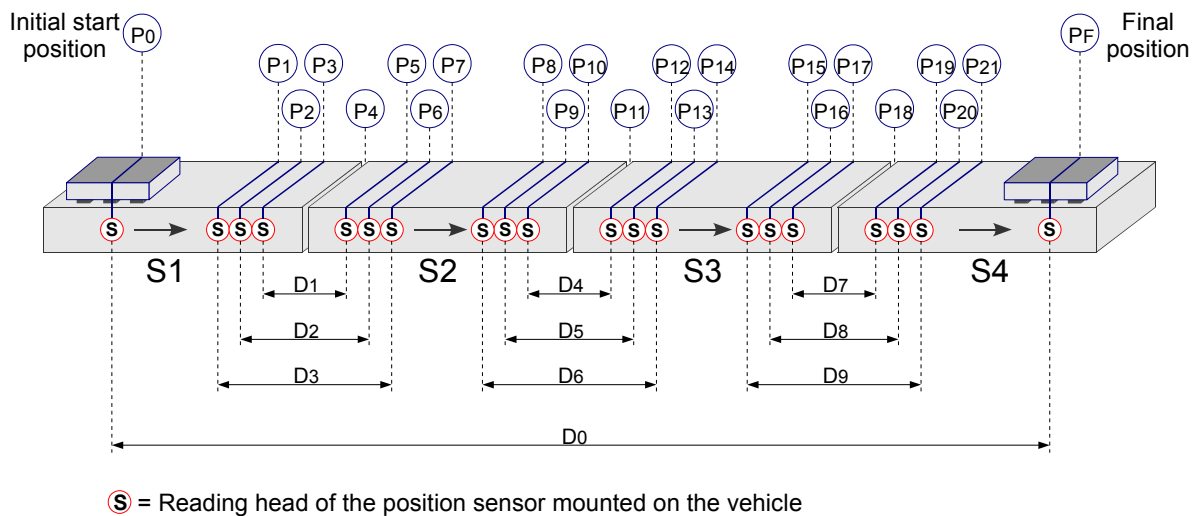

Ⓢ = Reading head of the position sensor mounted on the vehicle

Figure 6.2 Main vehicle positions during the controlled transition over the four segments

Position	Associated action
P1	DCU1 sends a communication request to DCU2. The communication is acknowledged.
P2	VSI2 begins the commutation process and DCU2 controls the q-current to zero.
P3	DCU2 becomes a slave controller and controls the q-current according to the received reference value from DCU1.
P4	The middle point between the stator segments. The mastership for position control will be transferred to DCU2 shortly after this point, when DCU1will control the q-current according to the received reference value from DCU2.
P5	DCU1 starts to control the q-current to zero. The vehicle covers only the second stator segment.
P6	VSI1 stops its commutation process. Only VSI2 is active.
P7	DCU2 and DCU1 interrupt their point-to-point communication.

Distance	Associated state
D1	The thrust force is produced by both VSI1 and VSI2.
D2	Both VSI1 and VSI2 are active.
D3	Point-to-point communication running between DCU1 and DCU2.

Table 6.1 Actions during the vehicle transition over two segments

As the vehicle crosses from segment $S1$ to segment $S2$, it passes through the positions marked in Fig. 6.2. Each position has an associated action as shown in Table 6.1. Similar actions occur also during the other two segment transitions. An algorithm implemented in the DCUs defines the transition process of the vehicle. This algorithm is represented by the flowchart of Fig. 6.3.
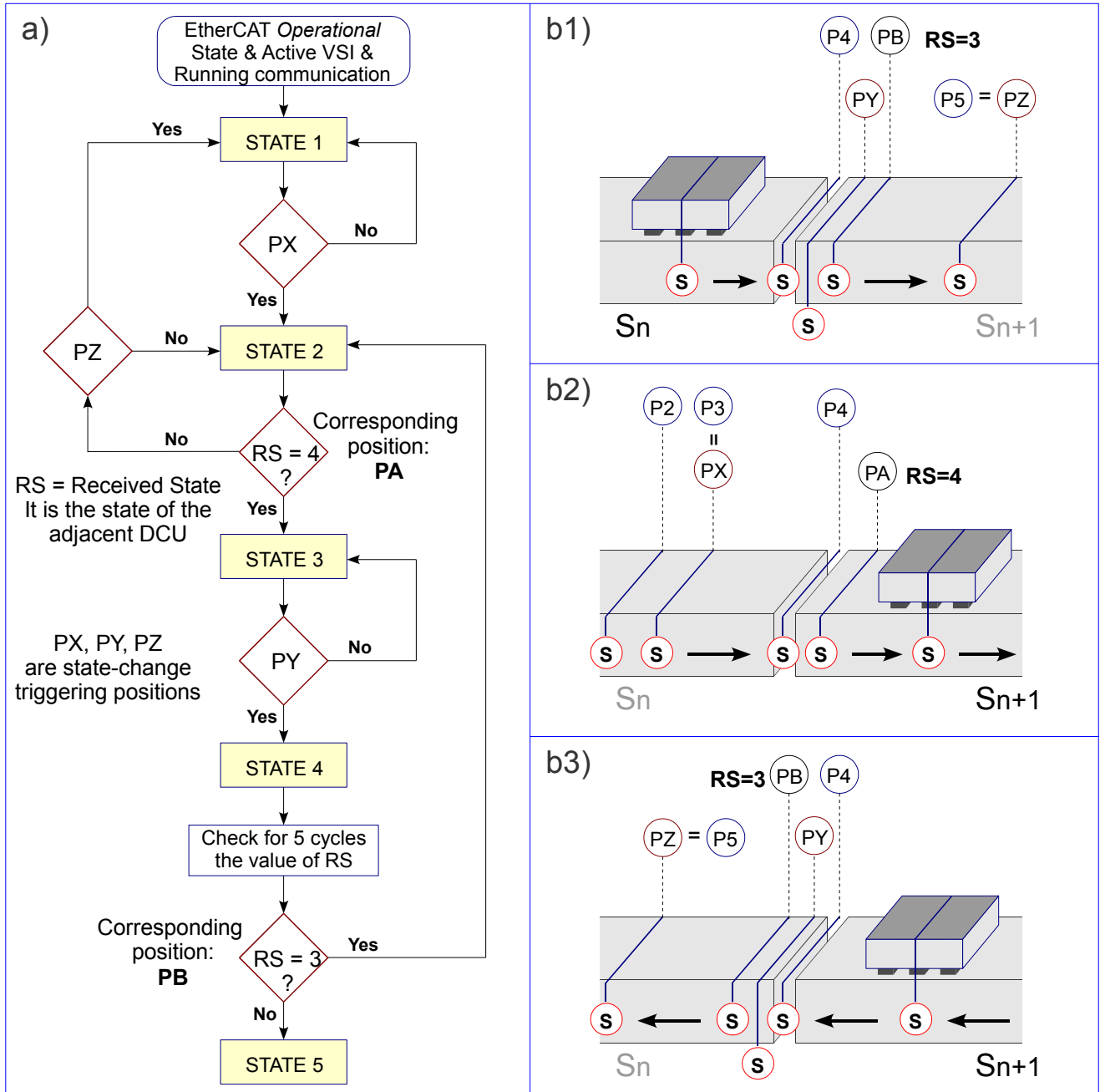

Figure 6.3 Description of the vehicle's transition process between two stator segments

a) Flowchart of the transition process

b1) Transition between Sn and $Sn+1$ seen from the point of view of DCUn

b2) Transition between Sn and $Sn+1$ seen from the point of view of DCUn+1

b3) Transition between $Sn+1$ and Sn seen from the point of view of DCUn+1

The flowchart begins with the initial state, which implies that the DCU is in the EtherCAT-state *Operational*, the inverter is active and the communication with the adjacent DCU is running.

State	Description
1	The q-current is controlled to zero.
2	The DCU is a slave controller and controls the q-current according to the received reference value.
3	The DCU is a master controller. It controls the position and speed of the vehicle.
4	Intermediate state required for the transfer of the mastership between the DCUs.
5	This state signals an error in the communication and transition process respectively.

Table 6.2 State description for the vehicle's transition process

Fig. 6.3-b1) describes the transition between the segments Sn and $Sn+1$ as seen from DCUn. As the vehicle starts from segment Sn, DCUn is a master controller (State 3). When the triggering position, PY, is detected, DCUn changes to State 4. The position PY does not coincide with the middle point between the segments ($P4$), but has a displacement of one millimeter. This helps to avoid abnormal state changes. In the same control cycle when PY was detected, DCUn is still the master controller. At the end of this cycle its actual state as well as the state-variables of its position and speed controllers are sent to DCUn+1. In the next cycle DCUn releases the mastership and becomes a slave controller. DCUn+1, which at this moment is in State 2, receives the state number of DCUn and changes to State 3. DCUn checks though if DCUn+1 really become the master controller. If DCUn doesn't receive this acknowledgment from DCUn+1 during five control cycles, will change to State 5. In this state DCUn will stop the vehicle and signal the CCU that an error occurred. In case of a successful mastership exchange, DCUn will change first to State 2 and when the triggering position, PZ, is detected, it will change to State 1.

Fig. 6.3-b2) presents the same transition but as seen from DCUn+1, which begins from State 1.

In Fig. 6.4 the reaction of the current controllers in all stator segments are shown, as well as the controlled speed and position. For this measurement, the speed was limited to 2 m/s (approximately half of the maximal speed) and the q-current was limited to about half of the maximal current. A 5 ms first order digital filter was used to filter the speed obtained from the position sensor. From the current waveforms one can recognize the transition periods where the inverters of two adjacent DCUs are active, as well as the periods where only the inverter of one segment remains active, as the vehicle completely leaves the other segment. The positions marked in this figure correspond to the positions of Fig. 6.2.

From the position and speed profiles it can be seen that the transitions between the stator segments is smooth and bump less, i.e. the initial values of the incoming controllers were set correctly.

Fig. 6.5 shows in detail the three transition periods of the vehicle: from segment $S1$ to $S2$, then from segment $S2$ to $S3$ and finally from segment $S3$ to $S4$. The state changes of the DCUs (according to the description in Fig. 6.3) are shown for each transition.
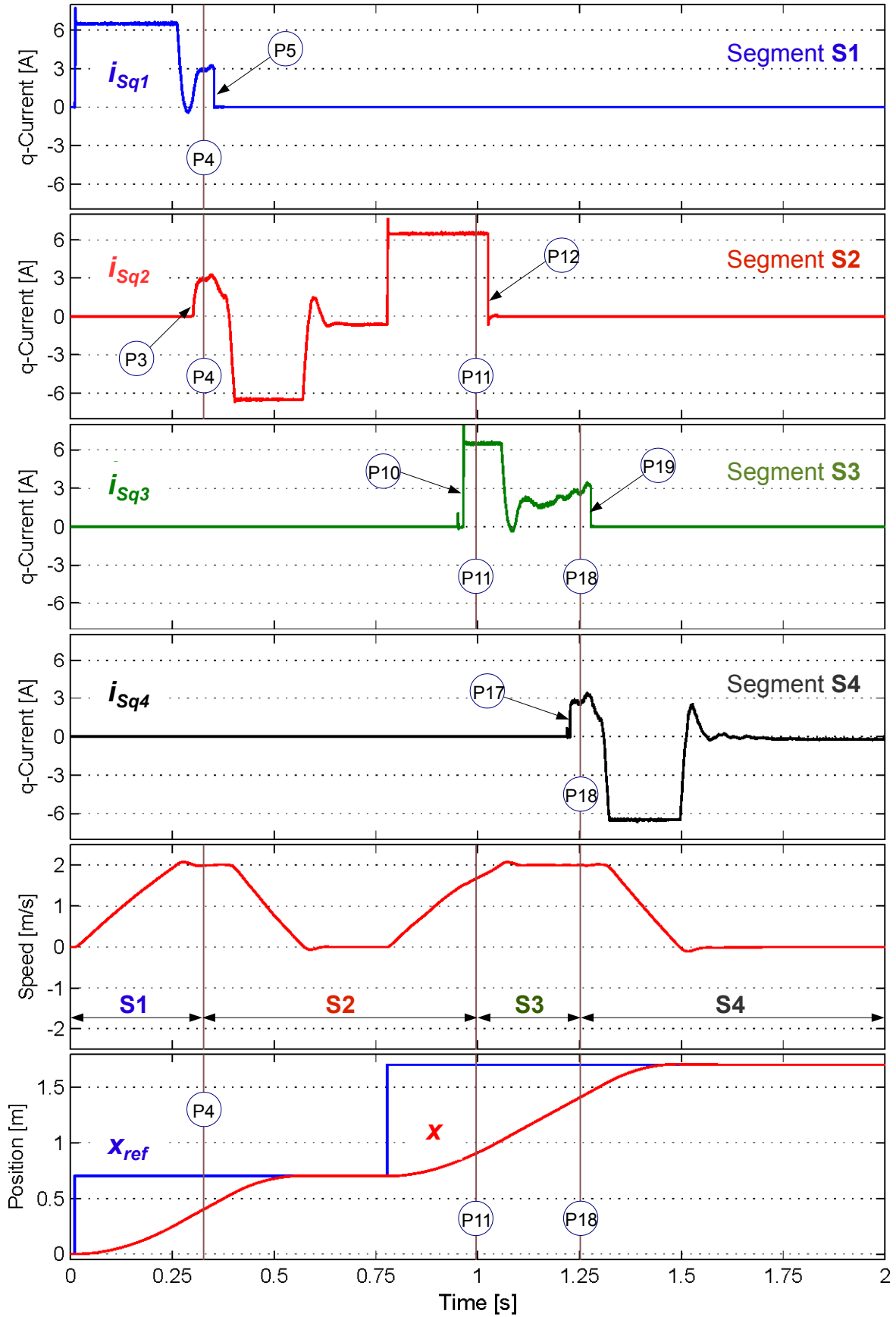
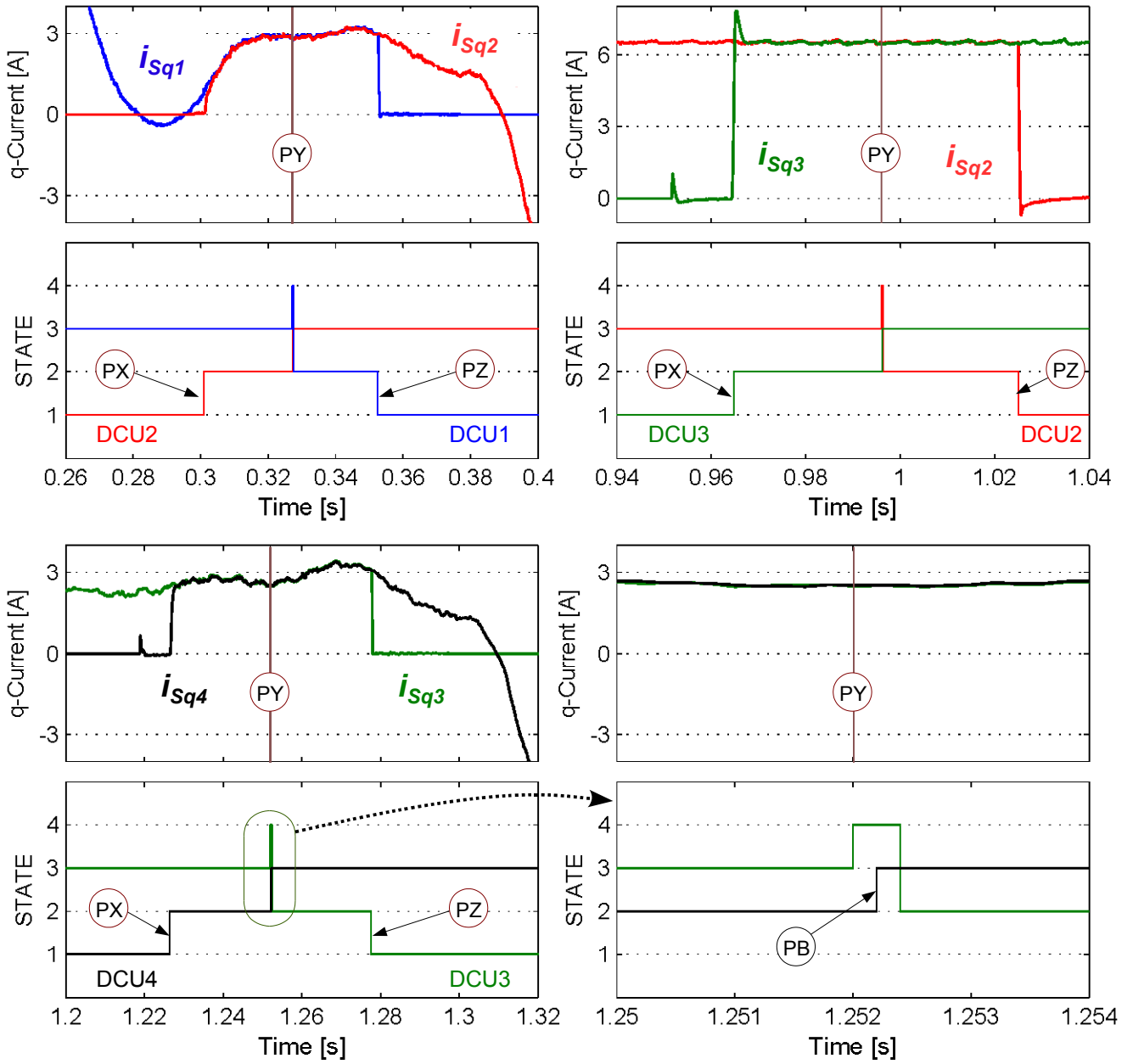Figure 6.4 Experimental results for the position control over four stator segments

Figure 6.5 Zoom of the vehicle's transition periods

6.2. Sensorless, EMF-based control

The track of the linear direct drive system contains areas where materials are processed and areas where materials are only transported. Along the processing areas, the presence of a position sensor is absolute necessary to achieve the desired positioning accuracy, precision and dynamics. Outside these processing areas a sensorless, EMF-based, control is used instead in order to save costs. This idea is illustrated in Fig. 6.6 on the basis of a simple processing line example.
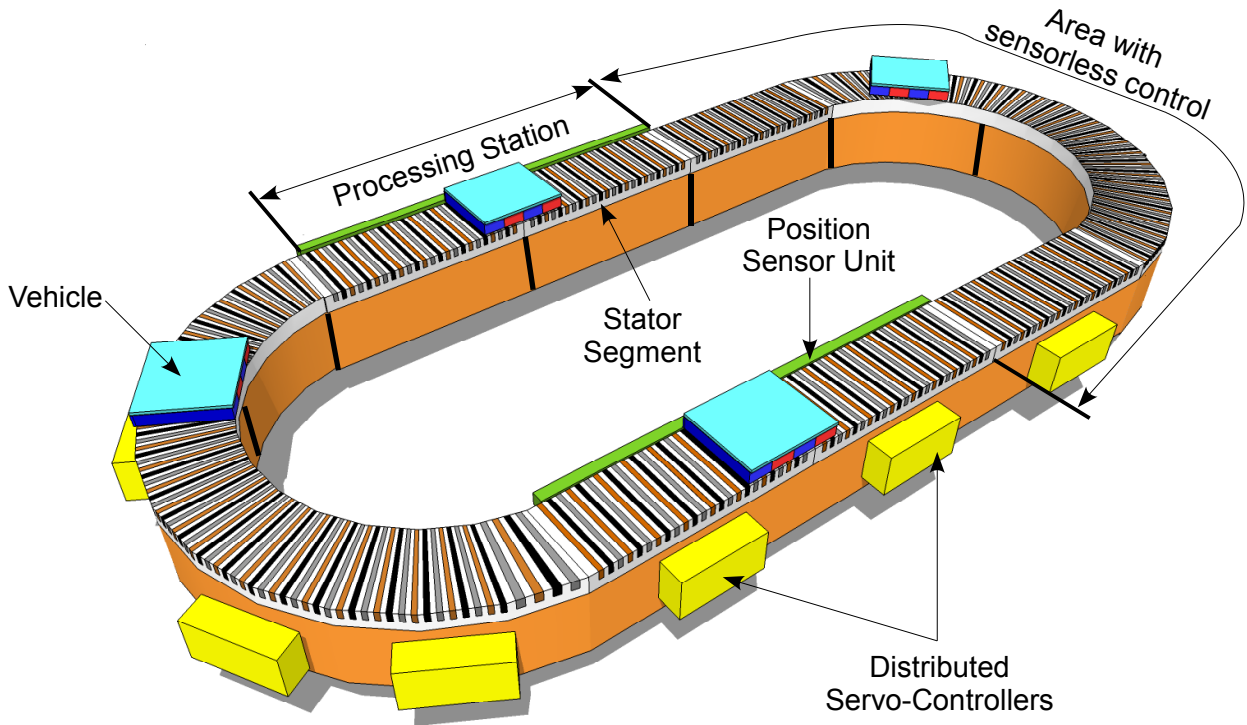

Figure 6.6 A simple processing line example with sensor-based and sensorless control

Further in this subchapter the term sensorless control refers only to the EMF-based control.

The sensorless control algorithm contains, as shown in Fig. 2.9, 2.10 and 2.11, two functional blocks. The first block implements an EMF-observer, while the second block implements the position and speed observer. During the vehicle's transition period, the EMFs are observed independently by both DCUs. The master-controller receives over the SPI-bus the EMF-value observed by the slave-controller, computes the sum of the EMFs and estimates the position and the speed of the vehicle with the help of a mechanical model of the motor.

Starting from the equation (2.7), the estimated values of the induced voltages in the stator reference frame (ab) can be simply expressed by:

$$\hat{e}_{Sa}(t) = u_{Sa,ref}(t) - R_S i_{Sa}(t) - L_S \frac{di_{Sa}(t)}{dt}$$

$$\hat{e}_{Sb}(t) = u_{Sb,ref}(t) - R_S i_{Sb}(t) - L_S \frac{di_{Sb}(t)}{dt}$$

$$(6.1)$$

The space vector of the real EMF-voltage is given by:

$$\underline{e}_S(t) = e_{Sa}(t) + je_{Sb}(t)$$
$$\underline{e}_S(t) \cdot e^{-j\beta} = e_{Sd}(t) + je_{Sq}(t)$$

(6.2)

The equation (6.4) shows the dependency of the estimated induced voltages in (dq)-frame with the orientation error $\Delta\beta$ and the position-dependent value of the flux linkage Ψ_{PM}. The characteristic of the flux linkage, which implies a reduction in the sum of the EMF-values of two stator segments during a transition period, doesn't make possible the speed estimation based on the EMF-magnitude. This approach is popular for rotating PMSM, where for small values of $\Delta\beta$ (< 30°) the estimated speed can be obtained directly from the estimated value $\hat{e}_{sq}$ and the term $\hat{e}_{Sd}$ is controlled to zero, in order to correct the value of $\hat{\beta}$. However, this is not possible for linear segmented motors and the speed-estimation must be based on the EMF-phase.

Figure 6.7 Vector diagram of the induced voltages
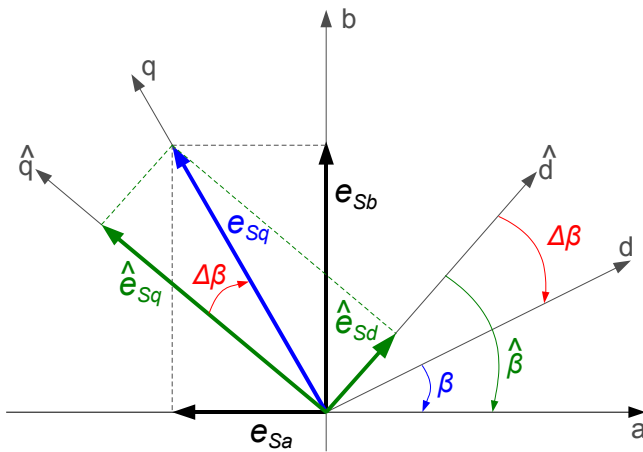
$$e_{Sd}(t) = 0$$
$$e_{Sq}(t) = \frac{3\pi}{2\tau}\Psi_{PM}(x)\cdot v(t)$$

(6.3)

$$\hat{e}_{sd}(t) = \frac{3\pi}{2\tau}\Psi_{PM}(\hat{x})\cdot\hat{v}(t)\cdot\sin(\Delta\beta)$$
$$\hat{e}_{sq}(t) = \frac{3\pi}{2\tau}\Psi_{PM}(\hat{x})\cdot\hat{v}(t)\cdot\cos(\Delta\beta)$$

(6.4)

$$\Delta\beta = \hat{\beta} - \beta$$

The design of the EMF-observer starts from equation (6.1). It is a disturbance observer based on the electrical model of the motor [64]. As it is difficult to measure the phase voltages of the motor, the command voltages $u_{sa,ref}, u_{sb,ref}$ are used instead. The accuracy of the EMF-estimation is related therefore with the accuracy of these command voltages. Due to the inverter's characteristics, e.g. dead-time, on-state voltages and turn-on/turn-off times, the command voltages will never entirely correspond to the actual values.

The dead-time effect is a very important issue for this application, as it will be explained further.

6.2.1. Dead-time effect and compensation

The dead-time is absolutely required in order to avoid a short-circuit in an inverter leg and its value depends on the switching devices used. It is preferable to keep it as low as possible, because the compensation of its effects is quite difficult.

The effect upon the reference output voltages of the inverter, due to the dead-time, the turn-on/turn-off times and the on-state voltage of the switching devices, is shown in Fig. 6.8. During the dead-time, the potential at the motor terminals is determined by the polarity of the phase

currents. A positive current causes a voltage loss while a negative current causes a voltage gain at the motor terminals.

For
$i_{S1} > 0$

$$u_{10} = \frac{1}{T_0} \left[(t_{on1} - t_{DEAD} - t_{C,ON} + t_{C,OFF})(\frac{U_D}{2} - U_{tx}) + \right.$$

$$\left. + (T_0 - t_{on1} + t_{DEAD} + t_{C,ON} - t_{C,OFF})(-\frac{U_D}{2} - U_{di}) \right]$$

For
$i_{S1} < 0$

$$u_{10} = \frac{1}{T_0} \left[(t_{on1} + t_{DEAD} - t_{C,OFF} + t_{C,ON})(\frac{U_D}{2} + U_{di}) + \right.$$

$$\left. + (T_0 - t_{on1} - t_{DEAD} + t_{C,OFF} - t_{C,ON})(-\frac{U_D}{2} + U_{tx}) \right]$$

(6.5)

where $t_{DEAD}, t_{C,ON}, t_{C,OFF}$ are the dead-time and the turn-on and turn-off times of the IGBT. U_{di}, U_{tx} are the on-state voltages of the diode and the IGBT. The switching time t_{on1} is calculated according to equation (2.20).
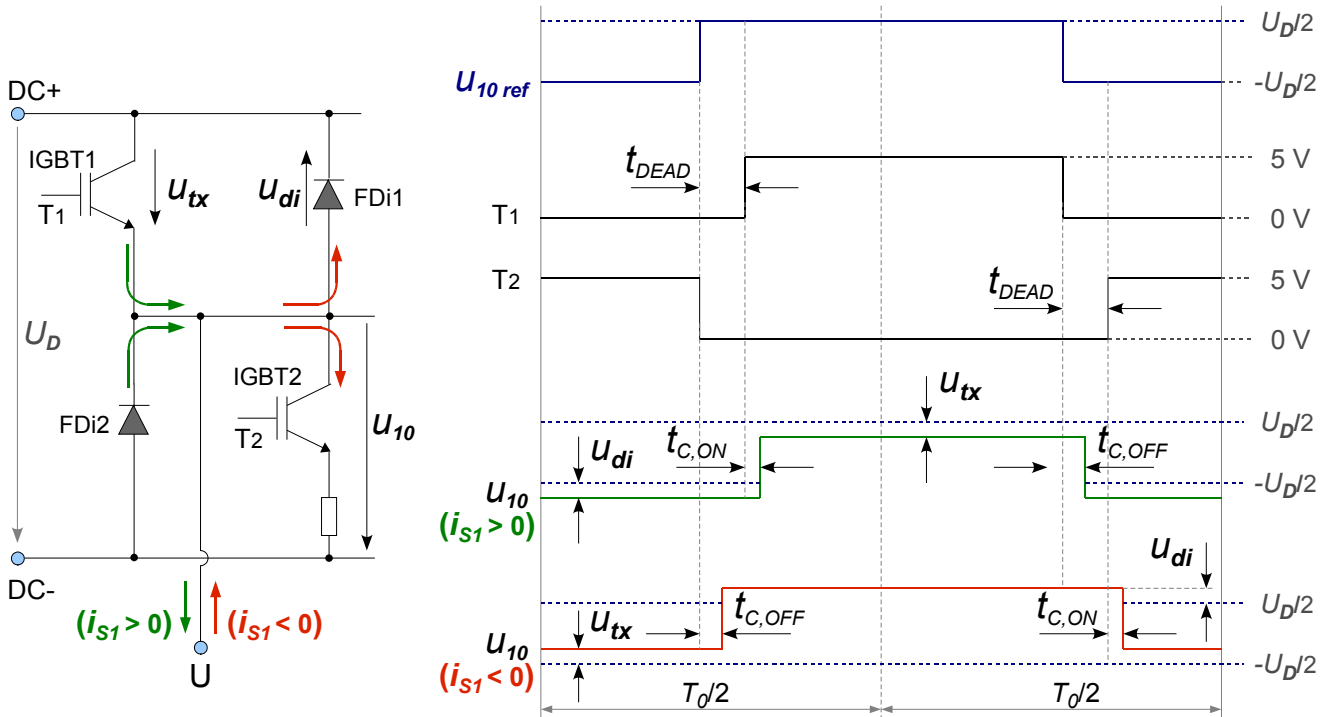

Figure 6.8 Distortion of the inverter's output reference voltages

The average value of the voltage deviation in one control cycle, according to the sign of the phase current, is expressed as:

$$U_{DV1} = \text{sgn}(i_{S1}) \frac{T_{DV1}}{T_0} U_D$$

(6.6)

The corresponding time deviation T_{DV1} is:

$$T_{DV1} = t_{DEAD} + t_{C,ON} - t_{C,OFF} + \frac{U_{dt}}{U_D} T_0$$

(6.7)

where U_{dt} is the average on-state voltage in a control cycle of both diodes and IGBTs. Similarly, the deviation voltages for the other two phases can be determined. According to the data-sheet of the PS22056 IPM, a dead-time period of at least 3.3 μs is required. The dead-time generator of the DSP was set at 3.4 μs. This large dead-time value corroborated with the high DC-link voltage and switching frequency values, leads to very high deviation voltages with values between ±20 V.

There are many proposals in the literature about how to calculate the compensation values for the

U_D	T_0	t_{DEAD}	$t_{C,ON}$	$t_{C,OFF}$	U_{DV}
560 V	100 μs	3.4 μs	0.9 μs	0.9 μs	≈ (±20 V)

Table 6.3 Characteristics of the VSI

inverter's output voltage. Many considerations start from the idea of adding compensation voltages to the command voltages of the current controllers [65]-[70]. Another approach was presented in [71], where the compensation is realised by the adjustment of the symmetric PWM pulses in every control cycle.

Remark: In spite of the large dead-time (3.4 μs) the current control loop is able to generate close to sinusoidal current waveforms even without any compensation in the control loop. This is shown in the measurement of Fig. 6.10a. But the large dead-time is a big problem for the EMF-observer and a compensation is for the observer mandatory. Fig. 6.9 shows that the compensation is used for the EMF-observer, but the current control loop needs no compensation.

The compensation methods are confronted with one or many of the following impediments:

- An accurate measurement of the current polarity is difficult due to the switching noise and the current clamping effect
- The characteristics of the inverter and the motor parameters are changing along with the operating conditions
- Variation of the DC-link voltage

The method presented in [70], depends only on the electrical model of the PMSM, as it implements a disturbance observer in order to calculate the deviation voltages. Anyhow, this method cannot be used in this case because the observer requires the EMF values.

Here an approach similar with the ones in [67] and [69] was adopted, where the compensation voltage is adjusted according to the load current. This is necessary because of the variation of the
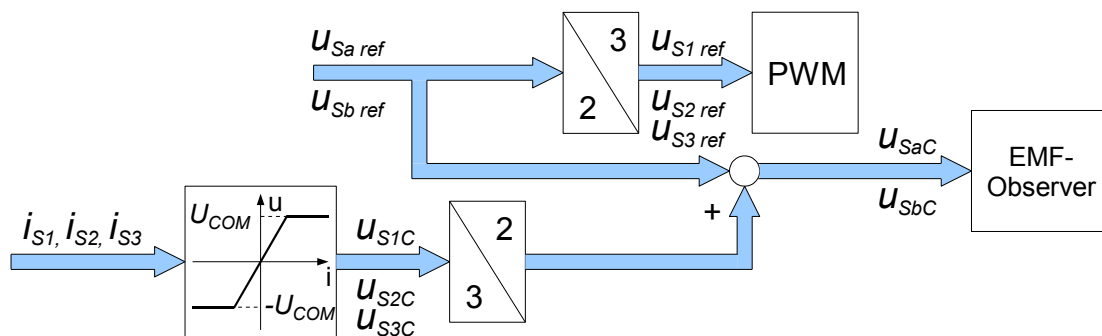

Figure 6.9 Dead-time compensation for the implemented EMF-Observer

turn-off time due to the parasitic capacitance of the switching devices [69].

For the measurement in Fig. 6.10 and 6.11 the vehicle was removed from the stator segment (no

a) Uncompensated command voltages   b) Compensated command voltages
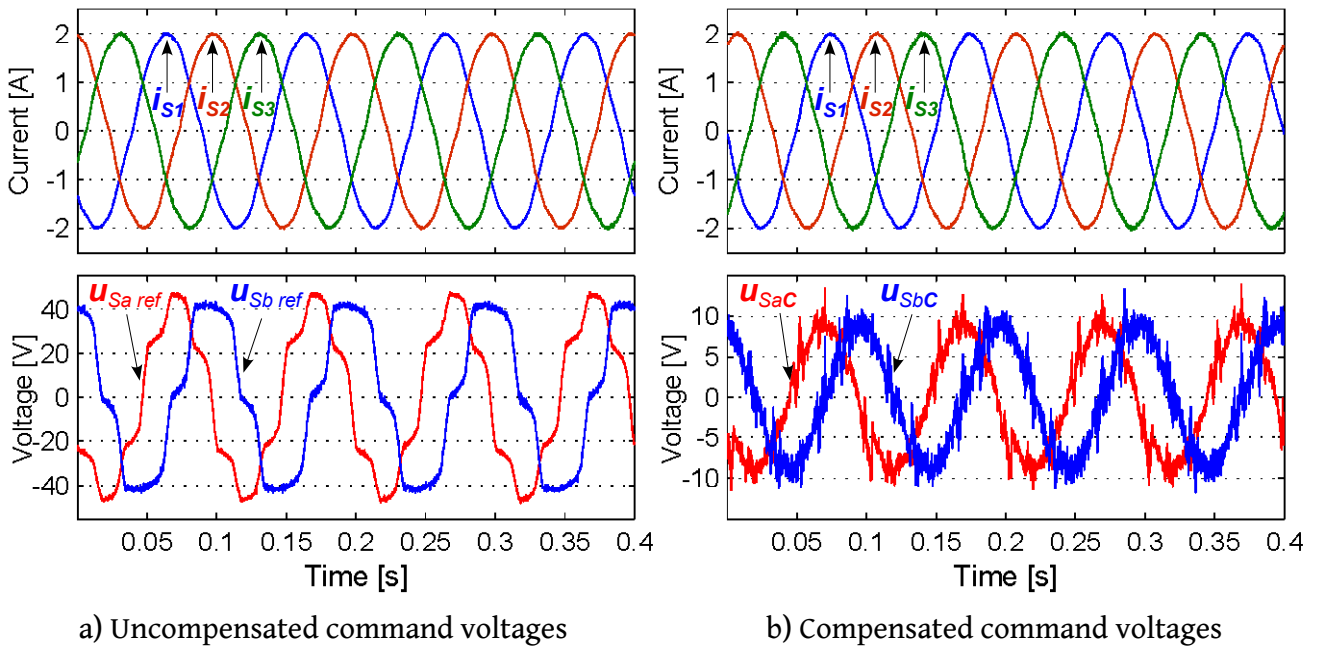
Figure 6.11 Uncompensated and compensated command voltages for a phase current of 2 A

EMF) and the frequency of the orientation angle was set at 10 Hz. It can be seen that the inaccuracies in the computation of the deviation voltages are still present and do not depend on the load-current. Both Fig. 6.10 and Fig. 6.11 show experimental results. An exact compensation would require a precise current measurement, a precise model of the diodes and switches and DC-link voltage measurement. The worst-case will always occur at small load-currents and small values of the induced voltage (small speed).
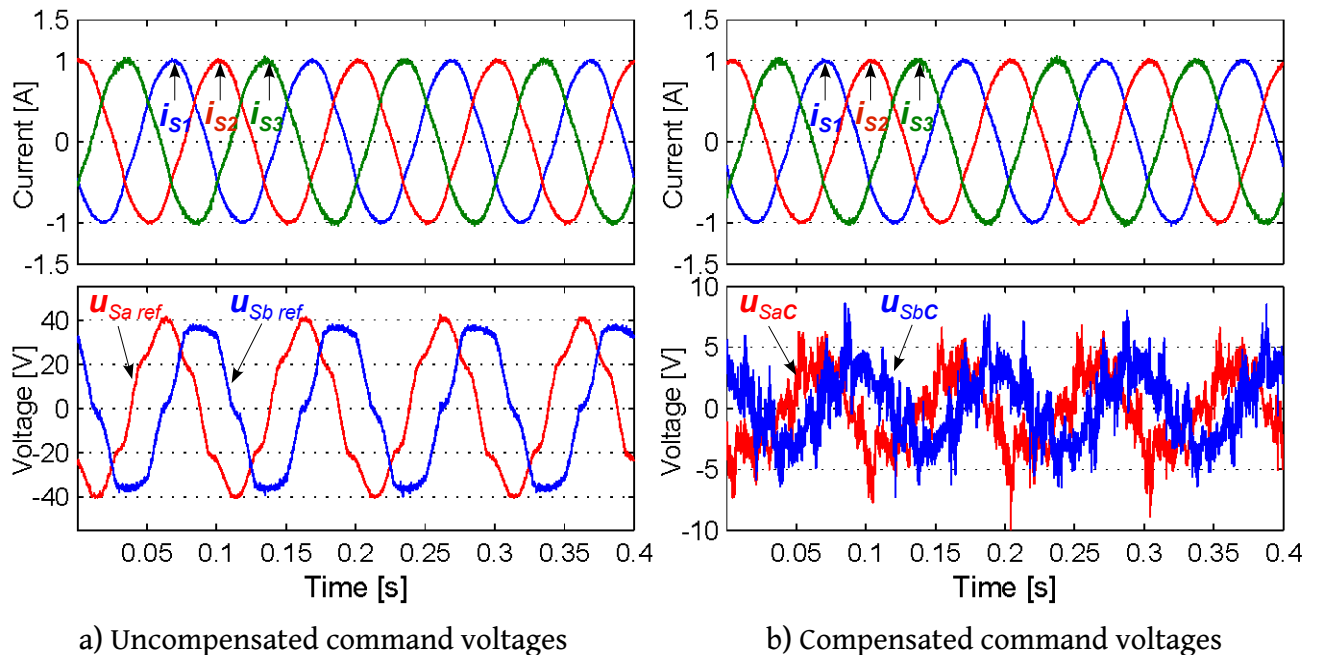

a) Uncompensated command voltages   b) Compensated command voltages

Figure 6.10 Uncompensated and compensated command voltages for a phase current of 1 A

6.2.2. The EMF observer

The EMF-observer is a disturbance observer based on the electrical model of the motor. Starting from the equation (2.7) the equivalent linear second order system with disturbance can be defined in matrix form as:

$$\frac{d}{dt}\underbrace{\begin{bmatrix} i_{Sa} \\ i_{Sb} \end{bmatrix}}_{\mathbf{x}} = \underbrace{\begin{bmatrix} -\dfrac{R_S}{L_S} & 0 \\ 0 & -\dfrac{R_S}{L_S} \end{bmatrix}}_{\mathbf{A}}\begin{bmatrix} i_{Sa} \\ i_{Sb} \end{bmatrix} + \underbrace{\begin{bmatrix} \dfrac{1}{L_S} & 0 \\ 0 & \dfrac{1}{L_S} \end{bmatrix}}_{\mathbf{B}}\underbrace{\begin{bmatrix} u_{Sa} \\ u_{Sb} \end{bmatrix}}_{\mathbf{u}} + \underbrace{\begin{bmatrix} -\dfrac{1}{L_S} & 0 \\ 0 & -\dfrac{1}{L_S} \end{bmatrix}}_{\mathbf{K}}\underbrace{\begin{bmatrix} e_{Sa} \\ e_{Sb} \end{bmatrix}}_{\mathbf{d}} \tag{6.8}$$

The disturbance model is defined by the following equations:

$$e_{Sa}(t) = -\frac{3\pi}{2\tau}\Psi_{PM}(x)\cdot v(t)\cdot\sin(\beta)$$

$$e_{Sb}(t) = \frac{3\pi}{2\tau}\Psi_{PM}(x)\cdot v(t)\cdot\cos(\beta) \tag{6.9}$$

The term Ψ_{PM} doesn't depend on time and assuming that the speed variation over a control cycle is very small, the time derivative of the induced voltages can be written as:

$$\dot{e}_{Sa}(t) = \frac{\pi}{\tau}v\left(-\frac{3\pi}{2\tau}\Psi_{PM}(x)\cdot v\cdot\cos(\beta)\right) = -\frac{\pi}{\tau}v\cdot e_{Sb}(t)$$

$$\dot{e}_{Sb}(t) = \frac{\pi}{\tau}v\left(\frac{3\pi}{2\tau}\Psi_{PM}(x)\cdot v\cdot\sin(\beta)\right) = \frac{\pi}{\tau}v\cdot e_{Sa}(t) \tag{6.10}$$

$$\frac{d}{dt}\underbrace{\begin{bmatrix} e_{Sa} \\ e_{Sb} \end{bmatrix}}_{\mathbf{d}} = \underbrace{\begin{bmatrix} 0 & -\dfrac{\pi}{\tau}v \\ \dfrac{\pi}{\tau}v & 0 \end{bmatrix}}_{\mathbf{Ad}}\begin{bmatrix} e_{Sa} \\ e_{Sb} \end{bmatrix} \tag{6.11}$$

From (6.8) and (6.11) the model of the observer is built:

$$\frac{d}{dt}\begin{bmatrix} \hat{\mathbf{x}} \\ \hat{\mathbf{d}} \end{bmatrix} = \begin{bmatrix} \mathbf{A} & \mathbf{K} \\ 0 & \mathbf{Ad} \end{bmatrix}\begin{bmatrix} \hat{\mathbf{x}} \\ \hat{\mathbf{d}} \end{bmatrix} + \begin{bmatrix} \mathbf{B} \\ 0 \end{bmatrix}\mathbf{u_C} + \begin{bmatrix} \mathbf{H} \\ \mathbf{G} \end{bmatrix}\begin{bmatrix} \mathbf{I_2} & 0 \end{bmatrix}\begin{bmatrix} \mathbf{x} - \hat{\mathbf{x}} \\ \mathbf{d} - \hat{\mathbf{d}} \end{bmatrix} \tag{6.12}$$

where $\mathbf{I_2}$ is the unity matrix. $\mathbf{H}$ and $\mathbf{G}$ are the gain matrixes of the observer and $\mathbf{u_C}$ is the matrix of the compensated voltages.

$$\mathbf{I_2} = \begin{bmatrix} 1 & 0 \\ 0 & 1 \end{bmatrix} \quad ; \quad \mathbf{H} = \begin{bmatrix} h_{11} & 0 \\ 0 & h_{22} \end{bmatrix} \quad ; \quad \mathbf{G} = \begin{bmatrix} g_{11} & 0 \\ 0 & g_{22} \end{bmatrix} \quad ; \quad \mathbf{u_C} = \begin{bmatrix} u_{SaC} \\ u_{SbC} \end{bmatrix}$$

The matrix $\mathbf{Ad}$ in the equation (6.12) implies that the estimated speed $\hat{v}$ equals the real speed v, which depends on the mechanical observer. The coupling between the observers is eliminated by the assumption in the equation (6.13).

$$\frac{d}{dt}\begin{bmatrix} \hat{e}_{Sa} \\ \hat{e}_{Sb} \end{bmatrix} = \begin{bmatrix} 0 \\ 0 \end{bmatrix} \qquad (6.13)$$

The equations describing the observer become then:

$$\frac{d\hat{i}_{Sa}(t)}{dt} = -\frac{R_S}{L_S}\hat{i}_{Sa}(t) - \frac{1}{L_S}\hat{e}_{Sa}(t) + \frac{1}{L_S}u_{SaC}(t) + h_{11}\left(i_{Sa}(t) - \hat{i}_{Sa}(t)\right)$$

$$\frac{d\hat{i}_{Sb}(t)}{dt} = -\frac{R_S}{L_S}\hat{i}_{Sb}(t) - \frac{1}{L_S}\hat{e}_{Sb}(t) + \frac{1}{L_S}u_{SbC}(t) + h_{22}\left(i_{Sb}(t) - \hat{i}_{Sb}(t)\right)$$

$$\frac{d\hat{e}_{Sa}(t)}{dt} = g_{11}\left(i_{Sa}(t) - \hat{i}_{Sa}(t)\right) \qquad (6.14)$$

$$\frac{d\hat{e}_{Sb}(t)}{dt} = g_{22}\left(i_{Sb}(t) - \hat{i}_{Sb}(t)\right)$$

The correction term of the observer is based on the difference between the measured and the estimated current. In order to simplify the model, the observer's gains are selected as: $h_{11} = h_{22}$ and $g_{11} = g_{22}$. Now the values of these coefficients are determined by matching the coefficients of the characteristic polynomial of (6.12) with the negative roots of a 4th order polynomial. The roots are chosen as real, double roots and the gains of the observer are selected as in [72]:

$$h_{11} = h_{22} = -(p_1 + p_2)$$
$$g_{11} = g_{22} = -p_1 p_2 \qquad (6.15)$$

where p_1, p_2 are the roots of the mentioned polynomial.

The freedom in selecting the values of p_1, p_2 is limited by the value of the orientation error $\Delta\beta$ produced by the assumption in (6.13). The orientation error should be $\Delta\beta < 30°$, otherwise a significant decrease in the amplitude of the electrical force occurs. As deduced in [72], the limitation of the orientation error is set by:

$$\Delta\beta \leq \tan^{-1}\left(-|v|\frac{\pi}{\tau}\frac{h_{11}}{g_{11}}\right) \qquad (6.16)$$

Equation (6.16) gives the ratio between the gain factors h_{11} and g_{11}, according to an imposed limit of the orientation error (here set at 25°). The gain h_{11} defines the dynamic of the observer. Because the quality of the command voltages u_{SaC}, u_{SbC} is strongly affected by noise, the dynamic of the observer had to be diminished in order to increase the filtering effect of the observer.

After the estimation of the induced voltages, the estimated orientation angle was computed as:

$$\hat{\beta} = \text{atan}\left(\frac{\hat{e}_{Sa\Sigma}}{\hat{e}_{Sb\Sigma}}\right) \qquad (6.17)$$

The term $\hat{e}_{Sa\Sigma}$ is equal to $\hat{e}_{Sa}$ when the vehicle is completely inside a stator segment and with the sum of both induced voltages, i.e. $\hat{e}_{Sa,n} + \hat{e}_{Sa,n+1}$ during the vehicle's transition between the segments Sn and $Sn+1$. The same applies for $\hat{e}_{Sb\Sigma}$.

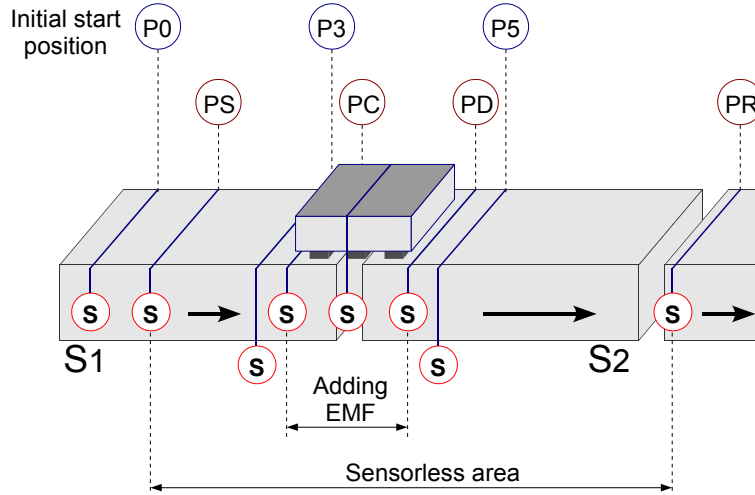The sensorless method was tested on two segments, as shown in Fig. 6.12.

Figure 6.12 Sensorless transition between two adjacent stator segments

The vehicle starts from the initial potion $P0$ and is accelerated until the position PS is reached, when the sensorless control is activated. At this position the speed of the vehicle is big enough to assure a reliable EMF-estimation. The sensorless motion of the vehicle ends at the position PR. Between the positions PC and PD, the EMF-values in both segments are added to build the values of $\hat{e}_{Sa\Sigma}, \hat{e}_{Sb\Sigma}$. The positions $P3$ and $P5$ are defined in the table 6.1. The flowchart of the transition process from Fig. 6.3 remains valid for the sensorless control too.

The Fig. 6.13 shows the estimated EMF-values and orientation angles for both stator segments. For the speed control the position sensor was used. In the interval defined by the positions PC and PD, the magnitude reduction of $\hat{e}_{Sa\Sigma}, \hat{e}_{Sb\Sigma}$ during the transition period can be seen. In the control cycle when the mastership is changed between the two DCUs, the initial value of the angle $\hat{\beta}_{2E}$ is set to the actual value of the angle $\hat{\beta}_{1E}$. The estimated angles $\hat{\beta}_{1E}, \hat{\beta}_{2E}$, and therefore the estimated position $\hat{x}_E$, have a high noise level, especially during the transition period.

6.2.3. The speed and position observer

The speed and position observer (mechanical observer) is designed starting from the mechanical model of the motor, which is defined as:

$$\frac{d}{dt}\begin{bmatrix} F_L \\ v \\ x \end{bmatrix} = \begin{bmatrix} 0 & 0 & 0 \\ -\dfrac{1}{M_v} & -\dfrac{b_C}{M_v} & 0 \\ 0 & 1 & 0 \end{bmatrix}\begin{bmatrix} F_L \\ v \\ x \end{bmatrix} + \begin{bmatrix} 0 \\ \dfrac{1}{M_v} \\ 0 \end{bmatrix} F_{th} \tag{6.18}$$

where b_C is the friction coefficient and F_L is the load force.

The block diagram of the observer is shown in Fig. 6.14. It is defined by the following equation:

$$\frac{d}{dt}\begin{bmatrix} \hat{F}_L \\ \hat{v} \\ \hat{x}_M \end{bmatrix} = \begin{bmatrix} 0 & 0 & 0 \\ -\dfrac{1}{M_v} & -\dfrac{b_C}{M_v} & 0 \\ 0 & 1 & 0 \end{bmatrix}\begin{bmatrix} \hat{F}_L \\ \hat{v} \\ \hat{x}_M \end{bmatrix} + \begin{bmatrix} 0 \\ \dfrac{1}{M_v} \\ 0 \end{bmatrix} F_{th} + \begin{bmatrix} k_1 \\ k_2 \\ k_3 \end{bmatrix}\begin{bmatrix} 0 & 0 & 1 \end{bmatrix}\begin{bmatrix} F_L - \hat{F}_L \\ v - \hat{v} \\ \hat{x}_E - \hat{x}_M \end{bmatrix} \tag{6.19}$$
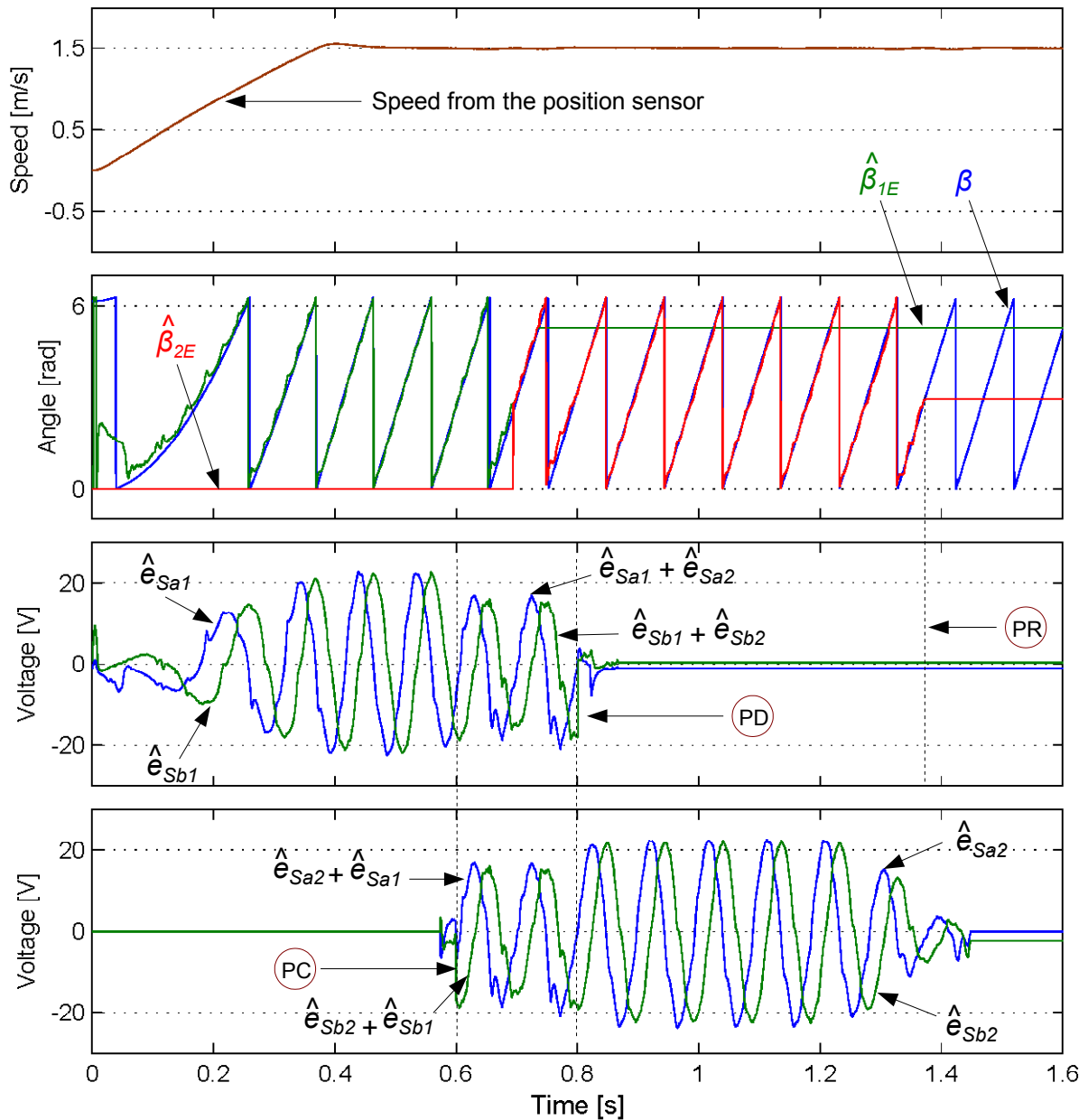
Figure 6.13 EMF-based estimation of the orientation angle (experimental results)

This type of observer is usually used for speed estimation, when the position measurement has a low resolution or a high noisy level. Here, the observer's input position is not coming from a sensor, but from the EMF observer and has the value $\hat{x}_E$. The deviation between $\hat{x}_E$ and the actual position is similar to a noisy position measurement, which has to be filtered by the observer. The correction term of the observer is based on the difference between the position $\hat{x}_E$ and the filtered position $\hat{x}_M$. The gain values of the observer are determined by means of the estimation

$$\frac{d}{dt}\begin{bmatrix} \tilde{F}_L \\ \tilde{v} \\ \tilde{x} \end{bmatrix} = \underbrace{\begin{bmatrix} 0 & 0 & -k_1 \\ -\dfrac{1}{M_v} & -\dfrac{b_C}{M_v} & -k_2 \\ 0 & 1 & -k_3 \end{bmatrix}}_{\mathbf{A_v}} \begin{bmatrix} \tilde{F}_L \\ \tilde{v} \\ \tilde{x} \end{bmatrix} \tag{6.20}$$

error model of (6.20), where $\tilde{F}_L = F_L - \hat{F}_L$, $\tilde{v} = v - \hat{v}$ and $\tilde{x} = \hat{x}_E - \hat{x}_M$.

The characteristic polynomial of the error model is:

$$\det(s \cdot \mathbf{I_3} - \mathbf{Av}) = s^3 + s^2 \left(\frac{b_C}{M_v} + k_3 \right) + s \left(\frac{b_C}{M_v} k_3 + k_2 \right) - \frac{k_1}{M_v} = 0 \qquad (6.21)$$

After matching the coefficients of the polynomial of (6.21) with a third order polynomial with the roots p_1, p_2, p_3, the values of the observer gain are:

$$k_1 = -p_1 \cdot p_2 \cdot p_3 \cdot M_v$$

$$k_2 = (p_1 \cdot p_2 + p_2 \cdot p_3 + p_1 \cdot p_3) - \frac{b_C}{M_v}(p_1 + p_2 + p_3) + \left(\frac{b_C}{M_v} \right)^2$$

$$k_3 = (p_1 + p_2 + p_3) - \frac{b_C}{M_v} \qquad (6.22)$$
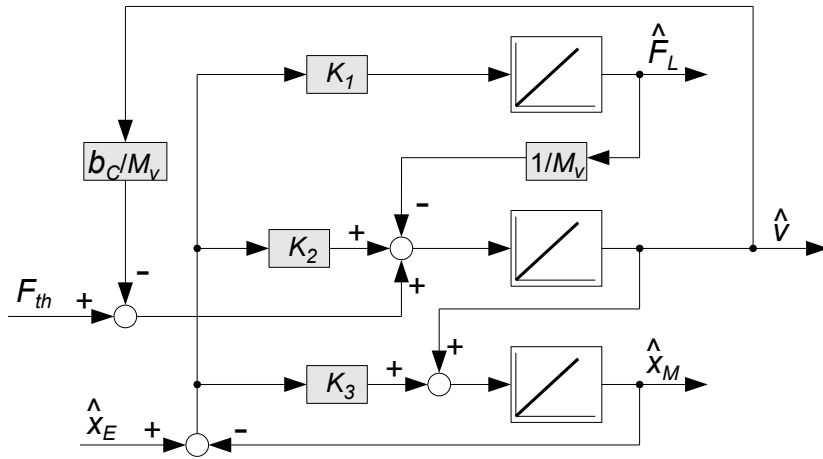
Figure 6.14 The block diagram of the position and speed observer

The mass of the vehicle is 6.5 Kg and the friction coefficient b_C has the value of 8 Kg/s. The values of p_1, p_2, p_3 are calculated so that they match the poles of a third order, low-pass Butterworth filter. Due to the high noise level of the calculated position $\hat{x}_E$, the cutoff frequency of the mechanical observer must be set very low. The filtering time constant of the Butterworth filter was set here at 15 ms. For this reason the sensitivity to the thrust force errors is high.

The experimental results shown in Fig. 6.15 show the values of the estimated speeds $\hat{v}_1, \hat{v}_2$, estimated orientation angles $\hat{\beta}_{1M}, \hat{\beta}_{2M}$ and the error $\Delta x = \hat{x}_M - x$ in the position estimation, for the sensorless control of the vehicle over two segments.

The orientation angles $\hat{\beta}_{1M}, \hat{\beta}_{2M}$ are defined as:

$$\hat{\beta}_{1M} = \frac{\pi}{\tau} \hat{x}_{1M}$$

$$\hat{\beta}_{2M} = \frac{\pi}{\tau} \hat{x}_{2M} \qquad (6.23)$$
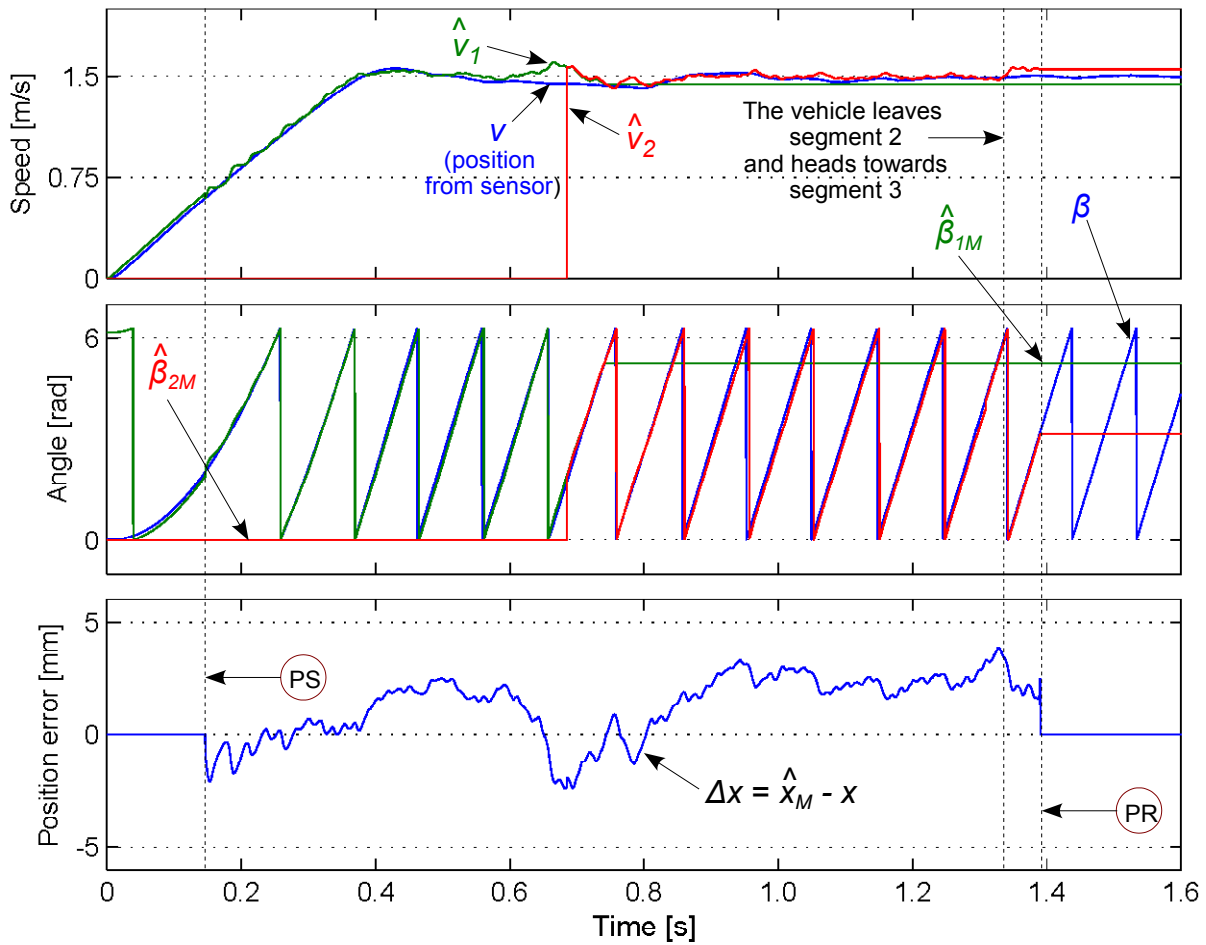
Figure 6.15 Speed sensorless control over two stator segments (constant speed)

When the vehicle is in the middle of the stator segments the following transitions occur:

$$
\begin{aligned}
\hat{\beta}_M &= \hat{\beta}_{2M} = \hat{\beta}_{1M} \\
\hat{x}_M &= \hat{x}_{2M} = \hat{x}_{1M} \\
\hat{v} &= \hat{v}_2 = \hat{v}_1
\end{aligned}
\tag{6.24}
$$

The error for the position estimation is smaller than 5 mm, which means that for a pole pitch $\tau = 36\ mm$, the error for the orientation angle $\Delta\beta = \hat{\beta}_M - \beta < 25°$. When the mastership is
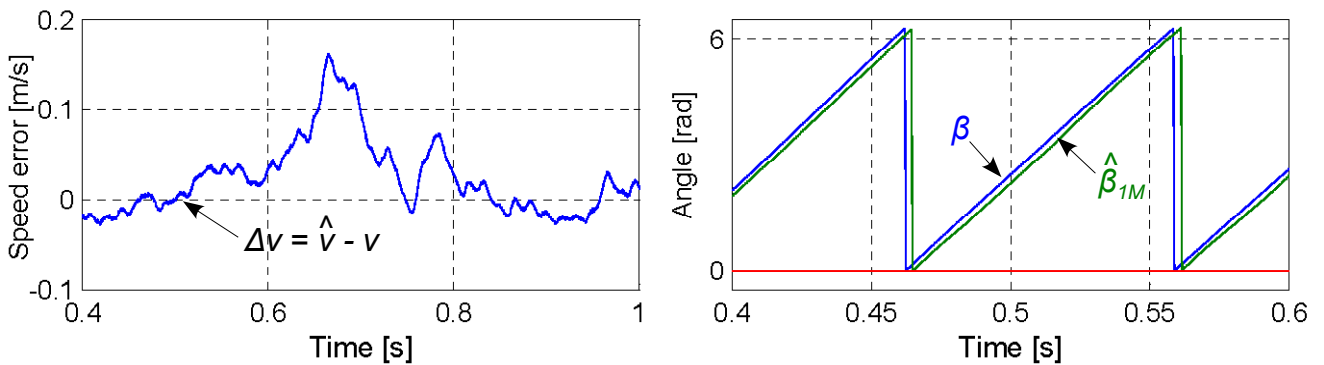
Figure 6.16 Orientation angle displacement and estimated speed error (zoom of Fig. 6.15)

changed between the two DCUs, the initial value of the speed $\hat{v}_2$ is set to the actual value of the speed $\hat{v}_1$. The Fig. 6.16 shows (for the same measurement from Fig. 6.15) that, as expected, the error for the estimated speed has the biggest value during the transition period. The commutation between the sensor-based and the sensorless control occurs at 0.6 m/s when the estimated EMF values are accurate enough for a good position and speed estimation.

In the case presented in Fig. 6.17, the vehicle is accelerated, shortly after it completely entered the second segment, from 1.5 m/s to 2 m/s. Also in this case the error for the position estimation remains smaller than 5 mm. Fig. 6.17 presents experimental results.
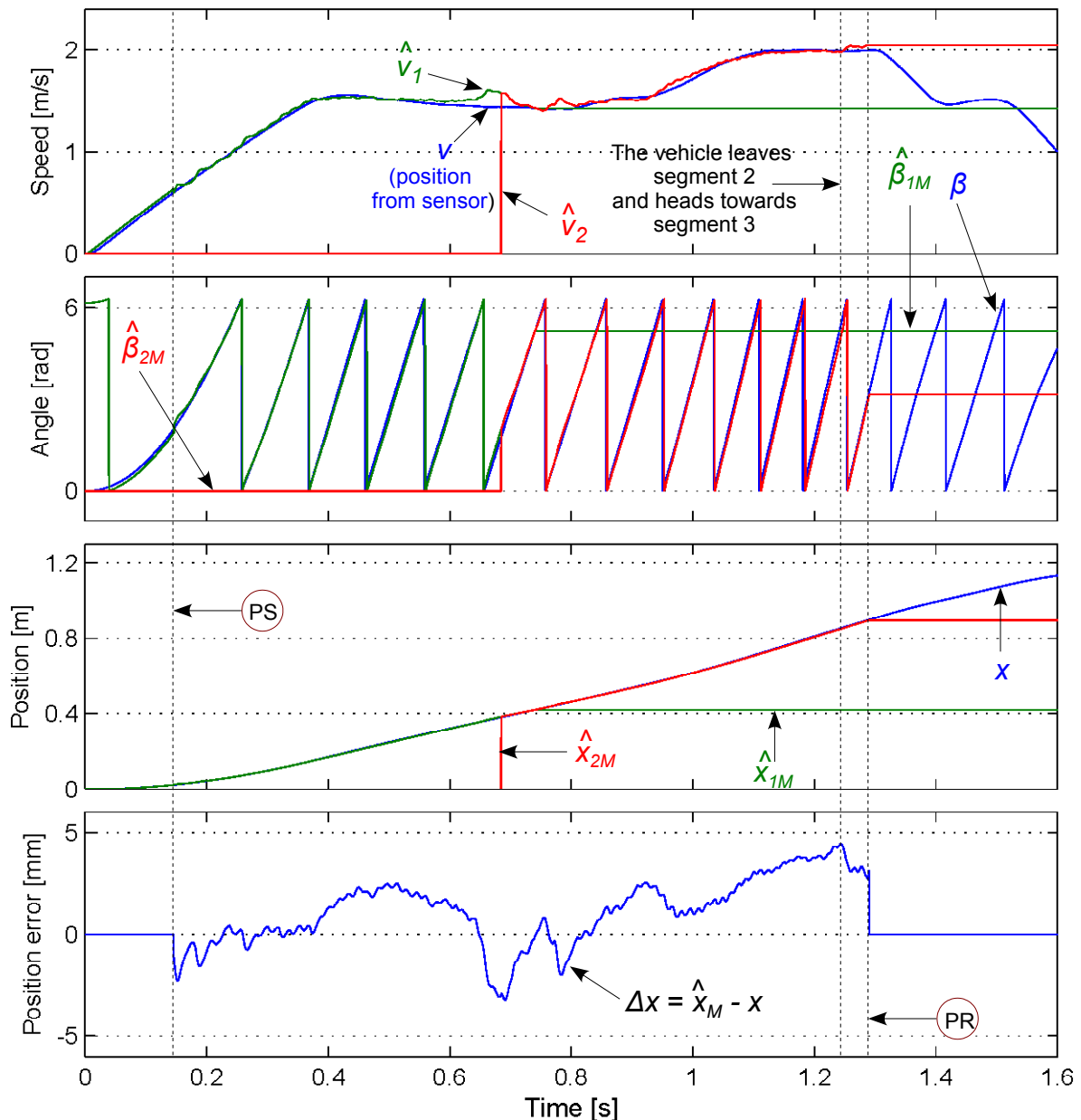
Figure 6.17 Speed sensorless control over two stator segments (acceleration)

7. Conclusions

The purpose of the work was to design a linear direct drive system for material handling and factory automation with totally distributed power and control stages. The system was designed to assure a high degree of modularity and scalability with minimal implementation costs. The characteristics and the performance of the designed system were tested on a small-scale experimental set-up. Among the multiple topologies of linear motors, the single-sided, long-stator PMLSM proved to be the most suitable solution.

For the power stage, the trend nowadays in electrical drives is to use compact power electronic modules with integrated gate-drivers and protection circuits. At the beginning of the work, the selected IPM was one of the few solutions available on the market in its power class. Beside the advantages of high-integration and low costs, the selected IPM has also some disadvantages. The biggest disadvantage is represented by the large dead-time, which influences the dynamic and performance of the sensorless control, as shown in chapter 6. The compact structure leads to higher capacitance values inside the module. It was demonstrated that the electronic of the servo-controllers, tied to the negative rail of the DC-link, functions properly under noisy conditions. A direct connection between the inverter and the controller was therefore possible. A safe current measurement, even at high modulation indexes, could be realised by using a shunt resistor in the low side of each inverter leg. Depending on the average value of the modulation index, continuous or discontinuous modulation methods can be used.

At the information processing stage, the hard real-time communication demands between the adjacent servo-controllers was solved by the proposed point-to-point connection. Here, the common-mode voltage problems of the RS485 devices were identified and analysed. In this case the value of this voltage was not of concern due to the low effective inductance of the bus bar system. The bus bar system can be of course further optimised, to reach smaller inductance values. Solutions have been also presented in the case that the common-mode voltage exceeds though the maximal specified values.

The task of motion coordination and monitoring was realised by means of an RTE-based fieldbus. EtherCAT was chosen here due to its advantages presented in chapter 4. In developing the communication structure of the system, the worst case was assumed, namely that all vehicles could be in a transition process. This led to the necessity of implementing the SPI-based

communication, besides the RTE-based one. A future work will be the optimisation of the motion coordination process with the help of special algorithms, so that the number of vehicles, which are in a transition state at a moment, is minimal. This would allow the utilisation of only one communication protocol, namely the RTE-based one. The overall costs would be therefore reduced and the transient voltages on the DC-link lines would be no more of concern.

In chapter 6, an EMF-based sensorless control method was presented. The results of this control method are satisfactory for the desired requirement, namely the sensorless transportation (with variable speed) of materials between the processing stations. Optical sensors give the best position measurement accuracy inside the processing stations. Their disadvantage is though their high price. Future work is therefore necessary to compare the cost-effective solutions: the capacitive and the magnetostrictive position sensors, and improve their accuracy.

Appendix

A.1 Speed control loop

App. 1 Diagram of the speed control loop

The transfer function of the open control loop is:

$$G_K(s) = \frac{V_{RV}}{k_f} \cdot \frac{T_{RV} \cdot s + 1}{T_{RV} \cdot s} \cdot \frac{1}{T_{EI} \cdot s + 1} \cdot \frac{1}{M_V \cdot s} \tag{A1}$$

where V_{RV}, T_{RV} are the gain and the time constant of the PI speed controller and T_F is the time constant of the speed filter.

The equivalent time constant of the current control loop is approximated by:

$$T_{EI} = 4 \cdot D_0^2 \cdot \frac{3}{2} \cdot T_0 \approx 3 \cdot T_0 \tag{A2}$$

The transfer function of the closed control loop is:

$$T_{EI} = 4 \cdot D_0^2 \cdot \frac{3}{2} \cdot T_0 \approx 3 \cdot T_0 \tag{A3}$$

The parameters of the controller are designed by using the method of symmetrical optimum:

$$V_{RV} = \frac{M_v}{2 \cdot k_f \left(T_{EI} + T_F \right)}$$
$$T_{RV} = 4 \left(T_{EI} + T_F \right) \tag{A4}$$

In order to avoid a big overshoot in the step response of the controller, a PT1 reference speed filter was used. The pole of this filter will compensate the zero of the closed control loop.

A.2   Position control loop

App. 2 Diagram of the position control loop

The transfer function of the open control loop is:

$$G_K(s) = \frac{V_P}{s(T_{EV} \cdot s + 1)}$$

(A5)

where V_P is the gain of the proportional controller and T_{EV} is the equivalent time constant of the speed control loop.

The transfer function of the closed control loop is:

$$G_0(s) = \frac{1}{\dfrac{T_{EV}}{V_P} s^2 + \dfrac{1}{V_P} s + 1}$$

(A6)

According to the amplitude optimum, the gain of the controller is:

$$V_P = \frac{1}{4 \cdot D_0^2 \cdot T_{EV}} \approx \frac{1}{2 \cdot T_{EV}}$$

(A7)

A.3   Analytical calculation of the parameters of a bi-plate DC-link bus bar system
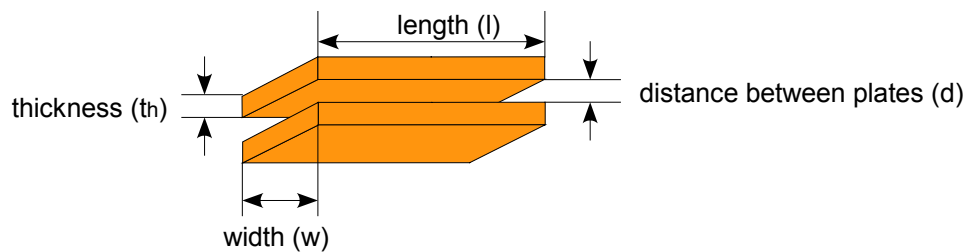
App. 3 Planar bi-plate DC-link bus

The effective inductance of the bus bar system at low frequencies is:

$$L_{eff,dc} = \frac{\mu_0 \mu_r}{8\pi} \cdot l + 2 \cdot \mu_0 \mu_r \cdot \frac{t_h \cdot l}{\pi(t_h + w)} \quad [\text{H}]$$

(A8)

where μ_r is the relative permeability of the isolating material.

The effective inductance of the bus bar system at frequencies above 1 MHz is defined by:

$$L_{eff,ac} = \frac{\mu_0 \mu_r}{w}(d + \delta) \ [H/m]$$

(A9)

where δ is the skin depth defined as:

$$\delta = \sqrt{\frac{\rho}{\pi f \mu_0}} \ [m]$$

(A10)

ρ is the conductivity of the conducting plates e.g. $\rho_{Copper} = 1.68 \cdot 10^{-8}$ [Ωm] and f is the frequency.

The resistance value of the two conductors at low frequencies is:

$$R_{dc} = \rho \frac{2 \cdot l}{w \cdot t_h}$$

(A11)

The resistance value of the two conductors at high frequencies is:

$$R_{ac} = \rho \frac{4 \cdot l}{w \cdot \delta}$$

(A12)

A.4 Calculation of the initial start position of the vehicle

In order to move the vehicle from standstill using the FOC, it is necessary for a PMLSM to know the relative position between the stator windings and the initial position of the PM (vehicle).
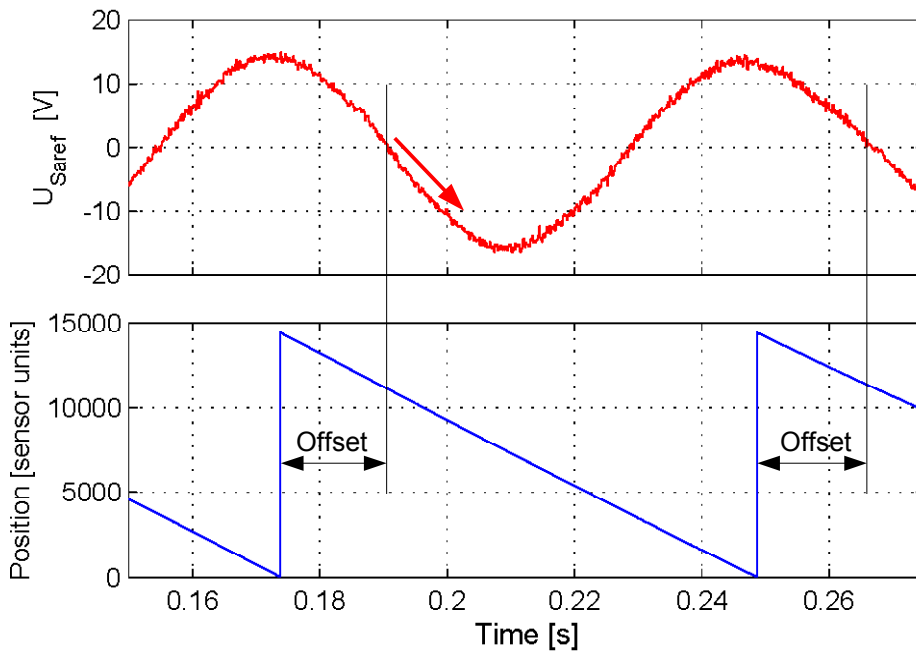
App. 4 Offset of the electrical angle of the vehicle at starting point (experimental results)

The offset between the reference starting position and the real position of Ψ_{PM} can be approximately determined with the help of the already tuned current controllers. For this, the reference values of both (dq) current controllers are set to zero and assuming that $\beta = 0$, the vehicle is moved with a relative constant speed. Because the currents are zero, the induced voltage in the machine will depend only on the vehicle's speed. The current controllers will compensate this induced voltage, so that the voltage response u_{Saref} will be almost equal to the induced voltage in the a-axis. The dead-time influence is very small due to the very low current values. The negative zero crossing points of the voltage u_{Saref} will point to the real position of Ψ_{PM}. If these points and the information from the position sensor are known simultaneously, the offset is determined as shown in Fig. App.4.

A.5   Characteristics of the IPM PS22056

Maximal ratings

Name	Symbol	Condition	Rating	Unit
Collector-emitter voltage	V_{CES}	-	1200	V
IGBT collector current	I_C	Junction temperature $T_J = 25°C$	±25	A
Junction temperature	T_J	-	-20 to +125	°C
Isolation voltage	V_{ISO}	Sinusoidal 60Hz, one minute	2500	V_{RMS}
Control input voltage	V_{IN}	Between U_P,V_P,W_P-V_{PC} ;U_N,V_N,W_N-V_{NC}	-0.5 to V_D+0.5	V

Static and switching characteristics

Name	Symbol	Condition	Min.	Typ.	Max.	Unit
Collector emitter saturation voltage	V_{CES}	$V_D = V_{DB} = 15V$ $V_{IN} = 5V, I_C = 25A, T_J = 25°C$	-	2.7	3.4	V
Diode forward voltage	V_F	$V_{IN} = 0, I_C = -25A$	-	2.5	3.0	V
Switching times	t_{ON}	VCC = 600V	0.8	1.5	2.2	μs
	t_{RR}	VD = 15V, VDB = 15V	-	0.3	-	
	$t_{C(ON)}$	$I_C = 25A$	-	0.6	0.9	
	t_{OFF}	$T_J = 125°C$	-	2.8	3.8	
	$t_{C(OFF)}$	Inductive load	-	0.6	0.9	
FO pulse width	t_{FO}	$C_{FO} = 22nF$	1.6	2.4	-	ms
HVIC circuit current	I_D	$V_D = V_{DB} = 15V$	-	-	1.3	mA

Recommended operation values

Name	Symbol	Condition	Min.	Typ.	Max.	Unit
Supply voltage	V_{CC}	Between P-NU, NV, NW	350	600	800	V
Control supply voltage	V_D	Between V_{P1}-V_{PC} and V_{N1}-V_{NC}	13.5	15	16.5	V
Control supply voltage	V_{DB}	Between $V_{U,V,WFB}$-$V_{U,V,WFS}$	13.5	15	16.5	V
Dead-time	t_{DEAD}	For each input control signal	3.3	-	-	μs
PWM frequency	f_S	Junction temperature $T_J < 125°C$	-	-	15	KHz
Output current	I_{RMS}	$V_{CC} = 600V, f_S = 15KHz, V_D = 15V$	-	-	9.2	A
Minimum PWM pulse width	PW_{ON}	-	1.5	-	-	μs
	PW_{OFF}	Collector current $I_C < 25A$	2.1	-	-	μs

A.5 Photos of the experimental set-up
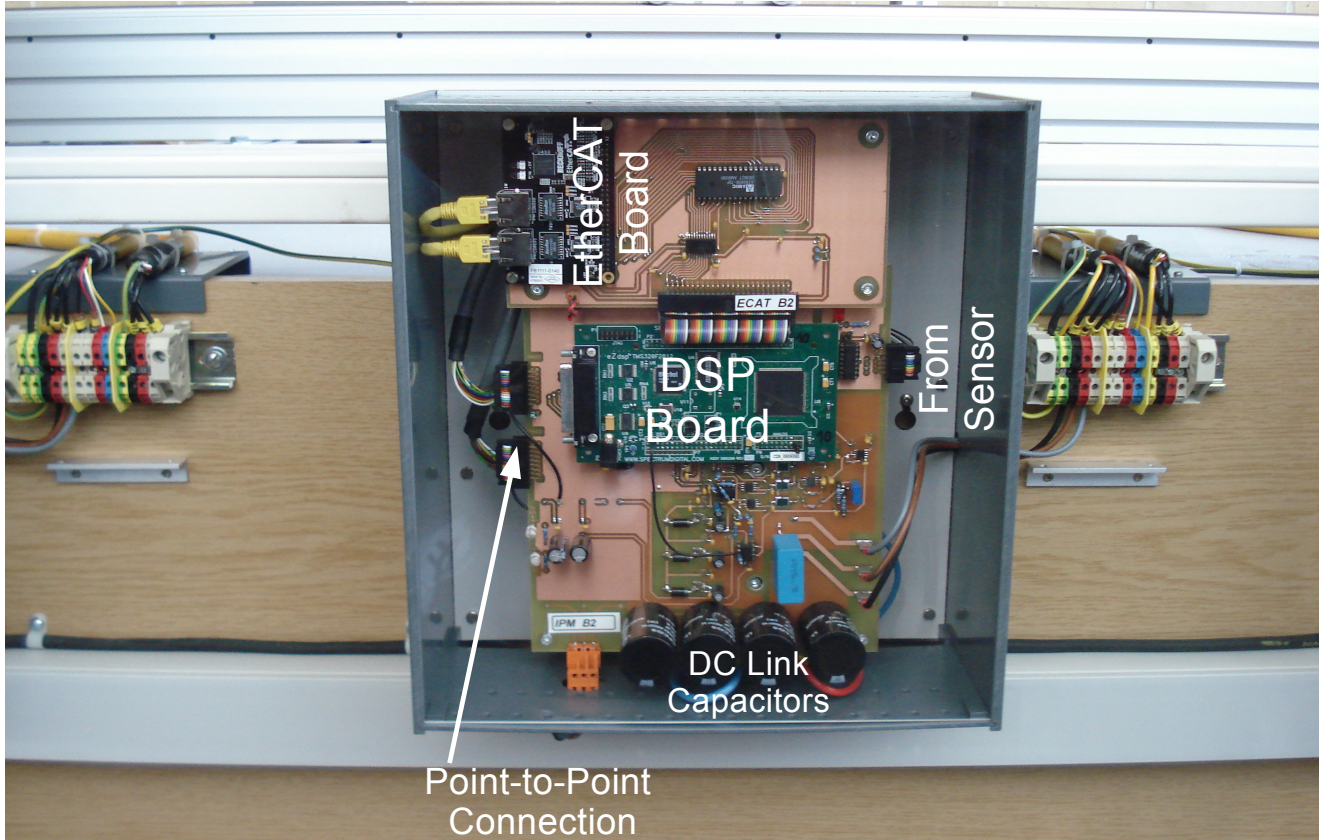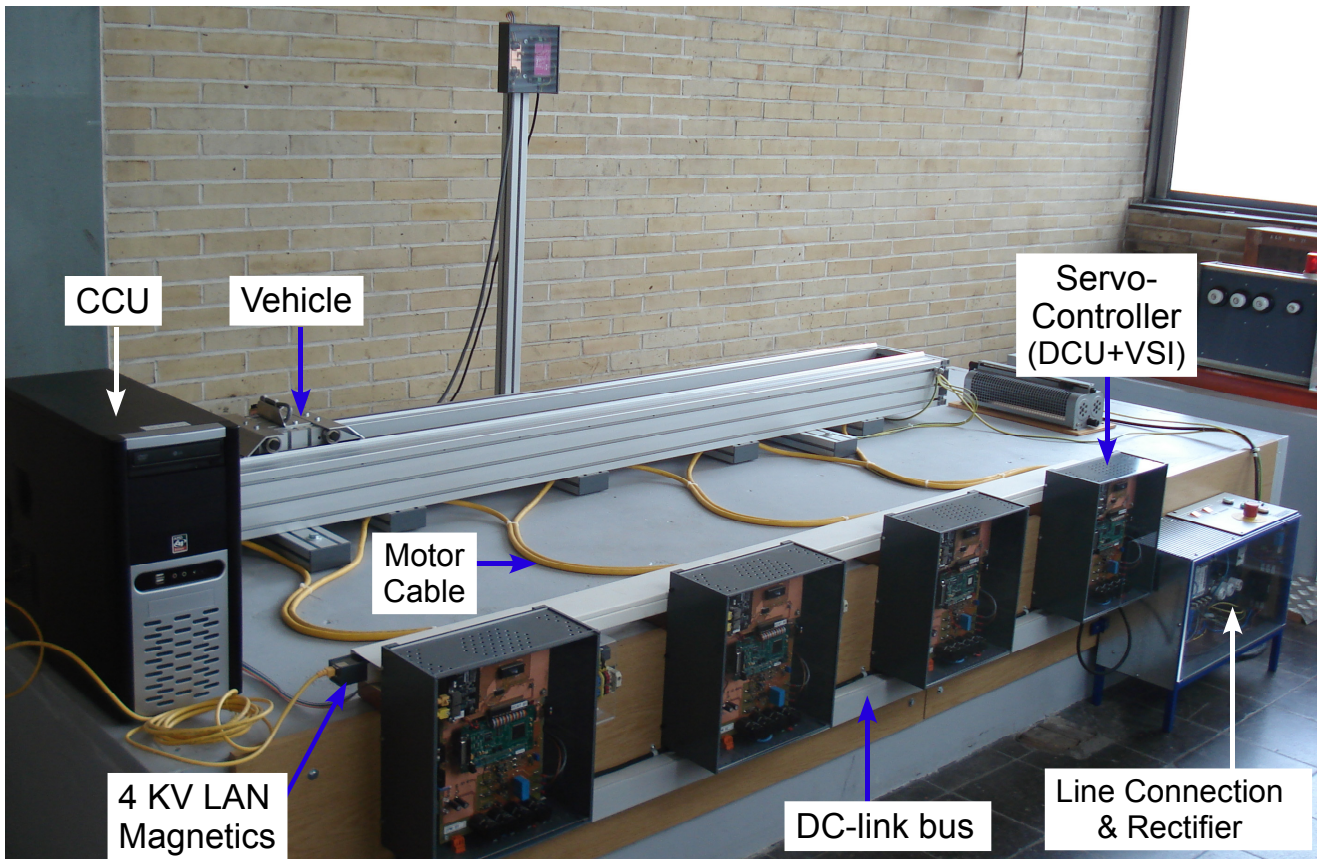
Bibliography

[1]   Laithwaite E. R., *"Linear Electric Motors"*, M&B Technical Library, London 1971; ISBN 0263515869

[2]   Boldea I., Nasar A., *"Linear Electric Actuators and Generators"*, Cambridge University Press, New York 1997; ISBN 0521480175

[3]   Gieras F., Piech J., *"Linear Synchronous Motors-Transportation and Automation Systems"*, CRC Press, Florida - Boca Raton 2000; ISBN 0849318597

[4]   Gurol H., *"General Atomics Linear Motor Applications: Moving Towards Deployment"*, Proceedings of the IEEE, Vol. 97, No 11, November 2009, pp. 1864-1871

[5]   Hellinger R., Mnich P., *"Linear Motor-Powered Transportation: History, Present Status and Future Outlook"*, Proceedings of the IEEE, Vol. 97, No 11, November 2009, pp. 1892-1900

[6]   Park D. Y., Shin B. C., Han H., *"Korea's Urban Maglev Program"*, Proceedings of the IEEE, Vol. 97, No 11, November 2009, pp. 1886-1891

[7]   Gustafsson J., *"Vectus-Intelligent Transport"*, Proceedings of the IEEE, Vol. 97, No 11, November 2009, pp. 1856-1863

[8]   Cassat A., Kawkabani B., Perriard Y., *"Power Supply of Long Stator Linear Motors-Application to Multi Mobile System"*, IEEE annual meeting of Industry Application Society, IAS 2008

[9]   Zhu Y., Lee S., Cho Y., *"Topology Structure Selection of Permanent Magnet Linear Synchronous Motor for Ropeless Elevator System"*, IEEE International Symposium on Industrial Electronics, ISIE 2010

[10]   Perreault, B., *"Optimizing Operation of Segmented Stator Linear Synchronous Motors"*, Proceedings of the IEEE, Vol. 97, No 11, November 2009, pp. 1777-1785

[11]   Henning U., Hoke D., Nothhaft J., *"Development and Operation Results of TRANSRAPID Propulsion System"*, International Conference on Magnetically Levitated Systems and Linear Drives, Maglev 2004

[12]   Mutschler P., Silaghiu S., *"Linear Drives for Material Handling and Processing: A Comparison of System Architectures"*, 34th annual conference of IEEE, IECON 2008

[13]   Corsi N., Coleman R., Piaget D., *"Status and New Development of Linear Drives and Subsystems"*, 6th International Symposium on Linear Drives for Industrial Applications, LDIA 2007

[14] http://www.parker.com/portal/site/PARKER|, *"Parker Linear Motor Solutions – Catalog 8092/USA"*, SectionA.pdf (February 2012)

[15] Fernandes Neto T. R., Mutschler P., *"Short Primary Linear Synchronous Motor Drive with an Ultracapacitor Regenerative Braking System for Material Handling and Processing"*, 8th International Symposium on Linear Drives for Industrial Applications, LDIA 2011

[16] Mihalachi M., Leidhold R., Mutschler P., *"Linear Drive System for Combined Transportation and Processing of Materials"*, 35th annual conference of IEEE, IECON 2009

[17] Purcarea C., Kedarisetti J., et al., *"A Motor-Friendly and Efficient Resonant DC-Link Converter"*, 13th European Conference on Power Electronics and Applications, EPE 2009

[18] Ranky P. G., *"MagneMotion's Linear Synchronous Motor (LSM) Driven Assembly Automation and Material Handling System Designs"*, Assembly Automation Journal, Vol. 27, No. 2, 2007, pp. 97-102

[19] http://www.magnemotion.com/industrial-automation/QS_layout.cfm, (February 2012)

[20] Zesheng D., Boldea I., et al. *"Fields in Permanent Magnet Linear Synchronous Machines"*, IEEE Transactions on Magnetics, Vol. 22, No 2, March 1986, pp. 107-112

[21] Leonhard W., *"Control of Electrical Drives"*, 3rd Ed., Springer-Verlag, 2001; ISBN 3-540-41820-2

[22] Denkena B., Tönshoff H. K., et al., *"Analysis and Control/Monitoring of the Direct Linear Drive in End Milling"*, International Journal of Production Research, Vol. 42, No. 24, December 2004, pp. 5149-5166

[23] Benavides R., Mutschler P., *"Compensation of Disturbances in Segmented Long Stator Linear Drives using Finite Element Models"*, IEEE International Symposium on Industrial Electronics, ISIE 2006

[24] Ogasawara S., Akagi H., et al., *"A Novel PWM Scheme of Voltage Source Inverters based on Space Vector Theory"*, Archiv für Elektrotechnik, Springer-Verlag, Vol. 74, 1990,

[25] Holtz J., Beyer B., *"Optimal Pulsewidth Modulation for AC Servos and Low-Cost Industrial Drive"*, IEEE Transactions on Industry Applications, Vol. 30, No. 4, August 1994, pp. 1039-1047

[26] van der Broeck H., Skudelny H. C., *"Analysis and Realization of a Pulsewidth Modulator based on Voltage Space Vectors"*, IEEE Transactions on Industry Applications, Vol. 24, No. 1, February 1988, pp. 142-150

[27] Reinold H., *"Optimierung dreiphasiger Pulsdauermodulationsverfahren"*, doctoral dissertation, Verlag der Augustinus Buchhandlung, Aachen1996, ISBN 3-86073-235-8

[28] Schröder J., *"Bezugsspannung zur Umrichtersteuerung"*, ETZ-B, Vol. 27, No. 7, 1975, pp. 151-152

[29] Leidhold R., *"Position Sensorless Control of PM Synchronous Motors based on Zero-Sequence Carrier Injection"*, IEEE Transactions on Industrial Electronics, Vol. 58, No. 12, 2008, pp. 5371-5379

[30]   Holtz J., *"Acquisition of Position Error and Magnet Polarity for Sensorless Control of PM Synchronous Machines"*, IEEE Transactions on Industry Applications, Vol. 44, No. 4, August 2008, pp. 1172-1180

[31]   Boldea I., Paicu M. C., et al., *"Active Flux Concept for Motion-Sensorless Unified AC Drives"*, IEEE Transactions on Power Electronics, Vol. 23, No. 5, September 2008, pp. 2612-2618

[32]   Linke M., Kennel R., et al., *"Sensorless Speed and Position Control of Synchronous Machines using Alternating Carrier Injection"*, IEEE International Conference on Electric Machines and Drives, IEMDC 2003

[33]   Zurawski R., *"The Industrial Communication Technology Handbook"*, CRC Press 2005; ISBN 978-0-8493-3077-3

[34]   Decotignie J., *"The Many Faces of Industrial Ethernet [Past and Present]"*, IEEE Industrial Electronics Magazine, Vol. 3, No. 1, March 2009, pp. 8-19

[35]   Rostan M., Stubbs J. E., et al., *"EtherCAT enabled Advanced Control Architecture"*, IEEE/SEMI Advanced Semiconductor Manufacturing Conference, ASMC 2010

[36]   Texas Instruments, *"TMS320x281x DSP Multichannel Buffered Serial Port Reference Guide"*, Literature Number SPRU061C, Revised November 2007

[37]   Silaghiu S., Mutschler P., *"Communication Topology in a Modular Servo-Drive System based on Long Stator Permanent Magnet Synchronous Linear Motor"*, 5th IET International Conference on Power Electronics, Machines and Drives, PEMD 2010

[38]   Texas Instruments, *"RS-422 and RS-485 Standards Overview and System Configurations"*, Literature Number SLLA070D, Revised May 2010

[39]   Bakran M. M., Helsper M., et al., *"Multicommutation of IGBTs in Large Inverters"*, 11th European Conference on Power Electronics and Applications, EPE 2005

[40]   Bock B., *"Switching IGBTs in Parallel Connection or with Enlarged Commutation Inductance"*, Doctoral dissertation, Bochum 2005, URL http://www-brs.ub.ruhr-uni-bochum.de/netahtml/HSS/Diss/BockBurkhard/diss.pdf

[41]   Skibinski G. L., Divan D. M., *"Design Methodology and Modelling of Low Inductance Planar Bus Structures"*, 5th European Conference on Power Electronics and Applications, EPE 1993, pp. 98-105

[42]   Zare F., Ledwich F. G., *"Reduced Layer Planar Busbar for Voltage Source Inverters"*, IEEE Transactions on Power Electronics, Vol. 17, No. 4, July 2002, pp. 508-516

[43]   Caponet M. C., Profumo F., et al., *"Low Stray Inductance Bus Bar Design and Construction for Good EMC Performance in Power Electronic Circuits"*, IEEE Transactions on Power Electronics, Vol. 17, No. 2, March 2002, pp. 225-231

[44] Decotignie J. D., *"A perspective on Ethernet-TCP/IP as a Fieldbus"*, IFAC 4th International Conference on Fieldbus Systems and their Applications, FeT 2001

[45] Thomesse J. P., *"Fieldbus Technology in Industrial Automation"*, Proceedings of the IEEE, Vol. 93, No 6, June 2005, pp. 1073-1101

[46] Felser M., *"Real-Time Ethernet-Industry Prospective"*, Proceedings of the IEEE, Vol. 93, No 6, June 2005, pp. 1118-1129

[47] Decotignie J. D., *"Ethernet-Based Real-Time and Industrial Communications"*, Proceedings of the IEEE, Vol. 93, No 6, June 2005, pp. 1102-1117

[48] Zurawski R., *"Embedded System Handbook-Networked Embedded Systems"*, CRC Press 2009; ISBN 978-1-4398-0761-3, Part IV, Chapter 21

[49] EtherCAT Technology Group (ETG), *"EtherCAT Communication Specification"*, Member Download Area, Version 1.0 2004

[50] Beckhoff Automation, *"The Windows Control and Automation Technology"* URL (http://www.beckhoff.com/default.asp?twincat/default.htm), Link retrieved in 2011

[51] Texas Instruments, *"Running an Application from Internal Flash Memory on the TMS320F28xxx DSP"*, Literature Number SPRA958J, Revised June 2011

[52] Texas Instruments, *"TMS320C28x Assembly Language Tools-User Guide"*, Literature Number SPRU513D, Revised May 2011

[53] Majumdar G., Iwasaki M., et al., *"Compact IPMs in Transfer Mold Packages for Low-Power Motor Drives"*, Proceedings of the International Symposium on Power Semiconductor Devices and ICs, ISPSD 2004

[54] Motto E., Donlon J., et al., *"A 1200V Transfer Molded DIP-IPM"*, POWEREX Technical Library URL (http://www.pwrx.com/Library.aspx?s=1^0|2^65|3^0|), article published in 2004

[55] Kolar W. J., Ertl H., et al., *"Influence of the Modulation Method on the Conduction and Switching Losses of a PWM Converter System"*, IEEE Transactions on Industry Applications, Vol. 27, No. 6, December 1991, pp. 1063-1075

[56] Kolar W. J., Round S. D., *"Analytical Calculation of the RMS Current Stress on the DC-link Capacitor of Voltage-PWM Converter Systems"*, IEE Proceedings of Electric Power Applications, Vol. 153, No. 4, July 2006, pp. 535-543

[57] Texas Instruments, *"TMS320F2810, TMS320F2811, TMS320F2812, TMS320C2810, TMS32C2811, TMS320C2812"*, Literature Number SPRS174S, Revised March 2011

[58] Texas Instruments, *"C28x IQmath Library, A Virtual Floating Point Engine"*, Literature Number SPRC990, Revised June 2010

[59]   Beckhoff   Automation,   *"ET1100   Hardware   Data   Sheet"*,   URL (http://www.beckhoff.de/german/download), Version 1.8, Revised 2010

[60]   Rüedi H., Köhli P., *"Driver Solutions for High-voltage IGBTs"*, PCIM Europe, Power Electronics Magazine, April 2002

[61]   Mihalachi M., Mutschler P., *"Position Acquisition for Long Primary Linear Drives with Passive Vehicles"*, IEEE annual meeting of the Industrial Applications Society, IAS 2008

[62]   Khong P. C., Leidhold R., et al., *"Magnetic Guiding and Capacitive Sensing for a Passive Vehicle of a Long-Primary Linear Motor"*, 14th International Conference on Power Electronics and Motion Control, EPE/PEMC 2010

[63]   Rettenmaier T., *"Positionserfassung und Kommunikation zwischen zwei DSPs in modularen Servoantriebssystemen"*, Diplom Thesis Nr. 1349, Darmstadt University of Technology, Institute of Power Electronics and Control of Drives, 2009

[64]   Tomita M., Senjyu T., et al., *"New Sensorless Control for Brushless DC Motors using Disturbance Observers and Adaptive Velocity Estimations"*, IEEE Transactions on Industrial Electronics, Vol. 45, No. 2, April 1998, pp. 274-282

[65]   Holtz J., *"Pulsewidth Modulation for Electronic Power Conversion"*, Proceedings of the IEEE, Vol. 82, No 8, August 1994, pp. 1194-1214

[66]   Seung-Gi J., Min-Ho P., *"The Analysis and Compensation of Dead-Time Effects in PWM inverters"*, IEEE Transactions on Industrial Electronics, Vol. 38, No. 2, April 1991, pp. 108-114

[67]   Munoz A. R., Lipo T. A., *"On-line Dead-Time Compensation Technique for Open-Loop PWM-VSI Drives"*, IEEE Transactions on Power Electronics, Vol. 14, No. 4, July 1999, pp. 683-689

[68]   Wang G. L., Xu D. G., *"A Novel Strategy of Dead-Time Compensation for PWM Voltage-Source Inverter"*, 23rd IEEE annual Conference and Exposition on Applied Power Electronics, APEC 2008

[69]   Urasaki N. T., Senjyu T., *"Dead-Time Compensation Strategy for Permanent Magnet Synchronous Motor Drive tacking Zero-Current Clamp and Parasitic Capacitance Effects into Account"*, IEE Proceedings of Electric Power Applications, Vol. 152, No. 4, July 2005, pp. 845-853

[70]   Hyun-Soo K., Hyung-Tae M., et al., *"On-line Dead-Time Compensation Method using Disturbance Observer"*, IEEE Transactions on Power Electronics, Vol. 18, No. 6, November 2003, pp. 1336-1345

[71]   Leggate D., Kerkman R. J., *"Pulse-based Dead-Time Compensator for PWM Voltage Inverters"*, IEEE Transactions on Industrial Electronics, Vol. 42, No. 2, April 1997, pp. 191-197

[72]   Leidhold R., Mutschler P., *"Speed Sensorless Control of a Long-Stator Linear Synchronous Motor Arranged in Multiple Segments"*, IEEE Transactions on Industrial Electronics, Vol. 54, No. 6, December 2007, pp. 3246-3254

Curriculum vitae

Name	Sorin Mihail Silaghiu
Birth date/place	31.08.1983/Romania
Nationality	Romanian
Educational achievements	
1997-2001	High School *Liceul Nichita Stanescu*, Ploiesti, Romania
2001-2006	Study of Electrical Engineering and Computer Science at *Transilvania* University, Brasov, Romania. Specialization: Automation Systems and Industrial Informatics
Professional experience	
2006	Student trainee at Siemens (*Power Generation*), Erlangen, Germany
2007-2011	Assistant at the department of *Power Electronics and Control of Electrical Drives*, Darmstadt University of Technology, Germany
since January 2012	Development engineer *at GIGATRONIK* company in Stuttgart, Germany